UNIVERSITY OF CALIFORNIA, SAN DIEGO

Study of Fields Structure at Strong Shock Front in Low-density System

A dissertation submitted in partial satisfaction of the
requirements for the degree
Doctor of Philosophy

in

Engineering Sciences (Mechanical Engineering)

by

Rui Hua

Committee in charge:

Farhat N. Beg, Chair
Sergei Krasheninnikov
Yuan Ping
Kevin B. Quest
Clifford M. Surko
George R. Tynan

2019

The dissertation of Rui Hua is approved, and it is acceptable in quality and form for publication on microfilm and electronically:

_____

_____

_____

_____

_____

_____

Chair

University of California, San Diego

2019

DEDICATION

To my parents Sumei and Guojun for their love and support ever since I was born.

To my husband Xiaohua for bringing cheer and joy to my life.

TABLE OF CONTENTS

LIST OF FIGURES

LIST OF TABLES

ACKNOWLEDGEMENTS

First and foremost, I want to thank my advisor Professor Farhat Beg for his guidance in the past several years. He accepted me to the group and introduced me to inertial confinement fusion. His support throughout my six years' Ph.D. life has been invaluable to my academic, professional and personal growth. I would also like to thank Yuan Ping, without her guidance and support, none of the work present in this thesis could be accomplished. I benefit so much from her enthusiasm and passion for research. Her endless knowledge in this field has helped me to become a better researcher.

Great thanks to Mark Sherlock, Chris McGuffey, Mathieu Bailly-Grandvaux and Scott Wilks for their encouragement and discussion from the aspects of theory, experiment, and simulation. They have provided instructions from their extensive knowledge and gave great support in paper writing.

I would like to thank all my colleagues in the High Energy Density Physics Group for their help and for being inspiring over the years. Thank Shu Zhang, Jonathan Peebles, Joohwan Kim, Mathieu Bailly-Grandvaux, Gilbert Collins IV, Christine Krauland, Maylis Dozieres, Krish Bhutwala, Joe Strehlow, and Jun Li. I would also like to thank my friends Shu Zhang, Zhao Chen, Zhuqing Yuan, Wei Wang, Kang Wang, Chu Yu, Zheng Xing, Yongfei Wang, Shiying Nie, and Sheng Jiang. My life became much more interesting with you guys. I want to thank my parents for their support and love ever since I was born. Finally, I want to sincerely thank my best friend, husband and true love, Xiaohua Xu. Thank you for bringing joy and wonderful memories to me. Meeting you in the beautiful city San Diego is the best thing ever happened in my life.

This work was performed under DOE contract DE-AC52-07NA27 344 with support from OFES Early Career program and LLNL LDRD program. CM is supported by the FES High Energy Density Laboratory Plasmas program (DE-SC0014600). The work has been partially supported by the University of California Office of the President

Lab Fee grant number LFR-17-449059.

Chapter 4, in full, is a reprint of the material as it appears in Applied Physics Letter: R. Hua, H. Sio, S. C. Wilks, F. N. Beg, C. McGuffey, M. Bailly-Grandvaux, G. W. Collins, and Y. Ping "Study of self-generated fields in strongly-shocked, low-density systems using broadband proton radiography" *Applied Physics Letter*, 2017. The dissertation author is the primary investigator and author of this paper.

Chapter 5, in full, is currently being prepared for publication as R. Hua, J. Kim, M. Sherlock, M. Bailly-Grandvaux, F.N. Beg, C. McGuffey, S. Wilks, H. Wen, A. Joglekar, W. Mori, Y. Ping "Self-generated magnetic and electric fields at a Mach-6 shock front in a low density1helium gas by dual-angle proton radiography", The dissertation author was the primary investigator and author of the paper.

Chapter 6, in full, is currently being prepared for publication as R. Hua J. May, M. Sherlock, M. Bailly-Grandvaux, M. Dozieres, F.N. Beg, C. McGuffey, W. Mori, and Y. Ping "Precursor structures of strong plasma shocks in helium and neon gases". The dissertation author was the primary investigator and author of the paper.

VITA

2009-2013	Bachelor of Science in Physics, University of Science and Technology of China, Hefei, China
2013-2019	Graduate Student Researcher, Mechanical and Aerospace Department, University of California, San Diego, U.S.A.
2013-2019	Doctor of Philosophy in Engineering Sciences (Mechanical Engineering), Mechanical and Aerospace Department, University of California, San Diego, U.S.A.

PUBLICATIONS

R. Hua, J. Kim, M. Sherlock, M. Bailly-Grandvaux, F.N. Beg, C. McGuffey, S. Wilks, H. Wen, A. Joglekar, W. Mori, Y. Ping "Self-generated magnetic and electric fields at a Mach-6 shock front in a low-density helium gas by dual-angle proton radiography", *in review for PRL*

R. Hua, H. Sio, S. C. Wilks, F. N. Beg, C. McGuffey, M. Bailly-Grandvaux, G. W. Collins, and Y. Ping "Study of self-generated fields in strongly-shocked, low-density systems using broadband proton radiography" *Applied Physics Letter*, *111(3), 034102* 2017

R. Hua J. May, M. Sherlock, M. Bailly-Grandvaux, M. Dozieres, F.N. Beg, C. McGuffey, W. Mori, and Y. Ping "Precursor structures of strong plasma shocks in helium and neon gases" *in prep*

Yuan Ping, Heather D. Whitley, Andrew McKelvey, Gregory E. Kemp, Phillip A. Sterne, Ronnie Shepherd, M. Marinak, **R. Hua**, Farhat N. Beg, and Jon H. Eggert " Heat-Release Equation-of-State and Thermal Conductivity of Warm Dense Carbon by Proton Differential Heating " *in review*

S. N. Chen, S. Atzeni, T Gangolf, M. Gauthier, D. P. Higginson, **R. Hua**, J. Kim, F. Mangia, C. McGuffey, J.-R. Marqus, R. Riquier, H. Ppin, R. Shepherd, O. Willi, F. N. Beg, C. Deutsch, and J. Fuchs " Experimental evidence for the enhanced and reduced stopping regimes for protons propagating through hot plasmas" *Scientific Reports*, *8(1), 14586* 2018

A. McKelvey, G. E. Kemp, P. A. Sterne, A. Fernandez-Panella, R. Shepherd, M. Marinak, A. Link, G. W. Collins, H. Sio, J. King, R. R. Freeman, **R. Hua**, C. McGuffey, J. Kim, F. N. Beg, and Y. Ping "Thermal conductivity measurements of proton-heated warm dense aluminum", *Scientific Report*, *7(1), 7015* 2017

H. Sio, **R. Hua**, Y. Ping, C. McGuffey, F. Beg, R. Heeter, C. K. Li, R. D. Petrasso, and G. W. Collins "A broadband proton backlighting platform to probe shock propagation in low-density systems", *Scientific Report 88(1), 013503* 2017

C. McGuffey, A. Raymond, T. Batson, **R. Hua**, G. M. Petrov, J. Kim, C. M. Krauland, A. Maksimchuk, A. G. R. Thomas, V. Yanovsky, K. Krushelnick and F. N. Beg "Acceleration of high charge-state target ions in high-intensity laser interactions with sub-micron target", *New Journal of Physics*, *18(11), 113032* 2016

ABSTRACT OF THE DISSERTATION

Study of Fields Structure at Strong Shock Front in Low-density System

by

Rui Hua

Doctor of Philosophy in Engineering Sciences (Mechanical Engineering)

University of California, San Diego, 2019

Professor Farhat N. Beg, Chair

Shocks are essential components in astrophysical systems and inertial confinement fusion (ICF). In recent decades, with the development of the proton probing technology, the fields associated with shock fronts have attracted great attention. However, the tiny scale of ICF relevant shocks and the finite resolving power of proton probing highlights the difficulty of measuring and differentiating between electric and magnetic fields. Besides, the hydrodynamic treatment, which is frequently used to predict the evolution of plasmas in inertial confinement fusion (ICF), may not be sufficient in simulating the shock convergence phase of the implosion, as the plasma can become kinetic in the high temperature, low-density conditions. Therefore, the quantitative experimental

measurement of the strong shock structure and the associated fields in the low-density plasma system is crucial for further understanding the shock physics and benchmarking the theoretical and numerical models.

This thesis proposes the experiments to study shock propagation in a cylindrical gas-tube along the central axis. This series of experiments were conducted on the OMEGA EP Facility. strong shocks were generated using long pulse beams from their laser system. Two primary diagnostics, proton radiography and a soft-X-ray spectrometer, were fielded to probe the field structure and plasma conditions at the shock fronts. Another short-pulse laser was used to generate protons for the proton radiography.

Given the difference in responses of charged particles to magnetic and electric fields, protons were designed to project the shock front region from multiple angles to distinguish the magnetic field from the electric field. For a Mach 6 shock propagating in pure helium gas, the oblique incident protons revealed the domination of the magnetic field on the order of couple tesla, while the normal incident protons disclosed the electric field on the order of couple hundreds of volts. Simulations indicate the Biermann battery effect and the electron pressure gradient at the shock front respectively accounts for the generation of the magnetic field and electric field.

In addition to the field structure, spatial profiles of density and temperature of strong shocks including the entire precursor regions are also measured by the soft x-ray spectrometer respectively in the helium and neon gases. With comparable peak electron temperatures at the shock fronts, a precursor layer, where electron temperature is far more than ion temperature, was found to be highly dependent on the atomic number Z as it extended much longer in the helium gas than in the neon gas.

Chapter 1

Introduction

1.1 Concept of Fusion

Fusion energy serves as a potentially ideal energy source for humankind with unlimited fuel reserves on earth. Contrary to fossil fuels that are widely used in the world, the production from fusion reaction is free from greenhouse gases and pollution, which are the primary sources causing global warming.

In a fusion reaction, the conservation of mass is no longer obeyed because part of the mass is converted to energy governed by the mass-energy equation $E = mc^2$. Here, we introduce the binding energy to help understand the energy released or absorbed in a fusion reaction. The binding energy is the minimum energy required to decompose a nucleus into nucleons, namely protons and neutrons. The expression for the binding energy is written as $E_B = (Nm_p + Zm_n - m_A)c^2$, where N is the number of protons in the nucleus, m_p is the proton mass, Z is the number of neutrons, m_n is the neutron mass and m_A is the mass of the original nucleus.

A curve of the average binding energy per nucleon (E_B/A, where A is the number

of nucleons) against the number of nucleons in the nucleus is shown in Fig.1.1[1]. The binding energy increases from hydrogen to ^{56}Fe and then decreases again. As one of the maximum binding energy, ^{56}Fe is the most stable element. When atoms that are lighter than iron fuse, the energy required to disassemble reactant atoms is smaller than that released from reassembling the protons and neutrons into the production atoms. Therefore, extra energy can be collected from such fusion reactions. Similarly, in the fission reaction, where elements that are heavier than iron decompose into lighter species, there will be extra energy released.

However, it is of great difficulty for a fusion reaction to take place due to the repulsive Coulomb force between positively charged protons. Extreme conditions are required to overcome such repulsive forces and bring protons as close as $10^{-15}m$, within which the attractive strong nuclear force takes place. The Coulomb force is inversely proportional to the square of the distance between two charged particles as:

$$F^{Coulomb} = \frac{e^2}{4\pi\varepsilon r^2}, \tag{1.1}$$

and the attractive strong nuclear force is inversely proportional to the quartic of the distance as:

$$F^{nuclear} = -\frac{k_N}{r^4}, \tag{1.2}$$

therefore, after being brought into the distance where the nuclear force plays a role, the protons and neutrons are forced together by the strong nuclear forces.

Despite the difficulty in making fusion reactions occur, fusion is superior to fission reactions in many aspects, such as the availability of the fuel sources, pollution from the fuel and production, and the efficiency of producing energy. The materials used for fusion reactions are mostly isotopes of hydrogen, namely deuterium and tritium,

and the products from them are commonly helium nuclei and neutrons. Two benefits regarding those fusion reactions are the unlimited reserve for the reaction fuel on earth and the safety of both the reaction and production materials involved. In contrast, the most commonly used material for fission reaction nowadays, $^{236}Uranium$, has very limited reserves on earth. Besides, both it and its products, $^{92}Krypton$ and $^{41}Barium$, are radioactive, therefore harmful for human beings' health. Besides, the efficiency of energy production of fusion is more than that of fission by a factor of 6 and is about 10^7 times more than that from an equal mass of fossil fuels.

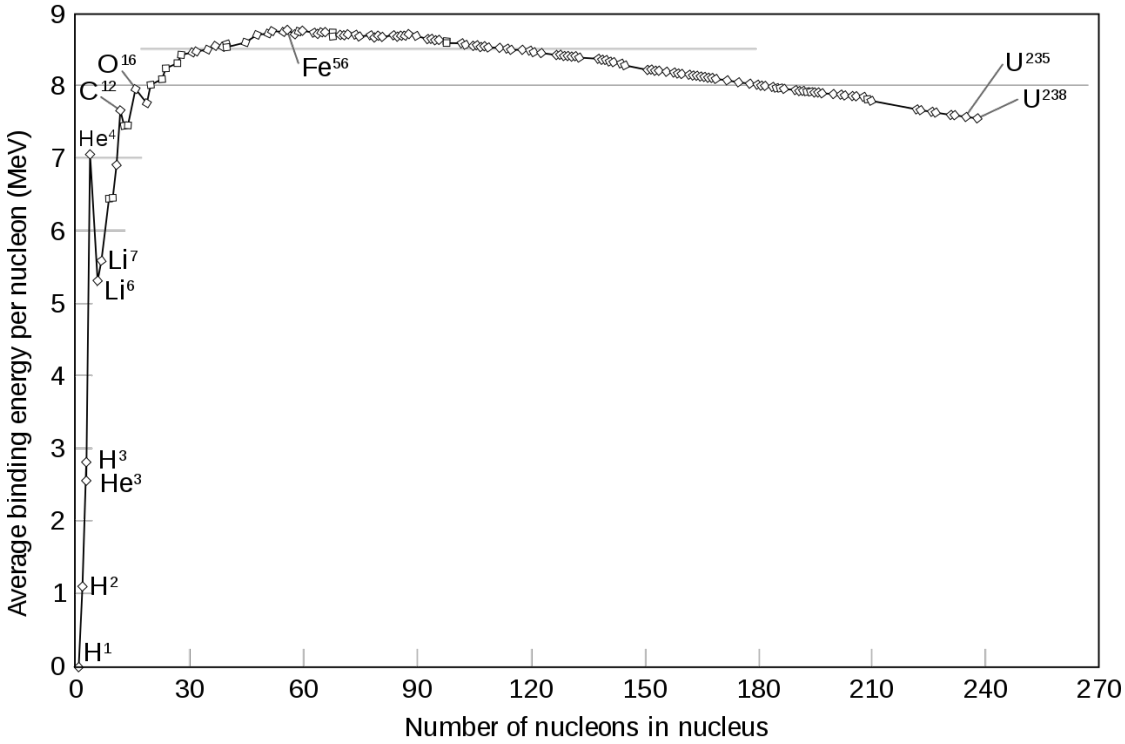

Figure 1.1: Average binding energy per nucleon along the number of nucleons in nucleus

Because fusion is so promising in providing clean and reusable energy for human activities, it attracts great attention and has been studied widely. The occurrence of a fusion reaction requires extreme conditions, where the temperature has to be on the order of 10^{10} degrees and the density has to be more than 20 times that of lead. One approach

to reach the condition is inertial confinement fusion (ICF), for which an overview is provided in the following section.

1.2 Basics of Inertial Confinement Fusion

Although extra energy can be collected as long as the fusion reaction occurs, the conditions required for the occurrence of the reaction are different depending on the elements used.

Among all the candidate reactions, deuterium and tritium are mostly used for fusion reactions due to their bigger fusion cross-section (as shown in Fig.1.2), which leads to a higher reaction rate. The reaction expression is as follows:

$$D + T \rightarrow \alpha(3.5MeV) + n(14.1MeV) \tag{1.3}$$

in each reaction, one deuterium and one tritium are reassembled into an alpha particle and a neutron.

For the achievement of the desired yield of energy, the heated deuterium, and tritium fuel are designed to be heated to a temperature in the order of keV and then be confined as long as possible. Two approaches used for the confinement are magnetic confinement fusion (MCF) and ICF. MCF uses a magnetic field to confine the deuterium/tritium (DT) plasma in a toroidal reactor of a 10 m scale. On the other hand, ICF uses the inertia of the target itself to provide confinement and can be performed on a much smaller scale (targets are in the order of millimeters).

Three different schemes have been developed to achieve ignition by the ICF approach: central hot spot ignition, fast ignition, and shock ignition. In this section, we only focus on the discussion of the central hot spot ignition which is most relevant to the

topic of this thesis.

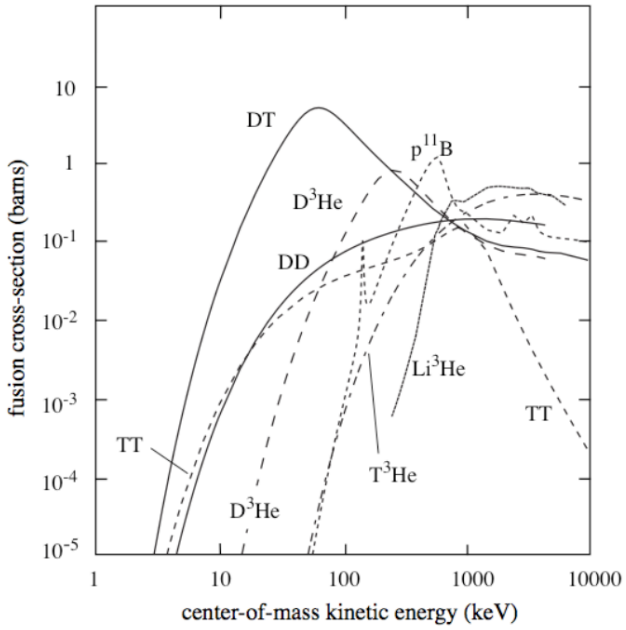

Figure 1.2: The fusion cross sections versus center-of-mass energy for various fusion reactions. The DT reaction has the largest cross-section among the reactions displayed. Figure from [2]

In a typical central spot ignition process, a spherical target made of plastic and filled with DT gas is illuminated by intense drivers uniformly from all directions. The drivers can either be multiple laser beams, for instance, 192 beams at the National Ignition Facility, indirect drive ICF shown as Fig.1.3, or x-rays generated by the interaction between those laser beams with hohlraum walls in indirect drive ICF shown as Fig.**??**.

Being illuminated and heated by the drivers, a surrounding plasma envelope can be formed by the blow-off from the target surface, which leads to the implosion of the remaining target due to the rocket effect. In the process of direct drive ignition, multiple laser beams illuminate the target shell, forming a surrounding plasma envelope. The remaining target compresses inward due to the blow-off rocket model. During the stagnation phase, the hot spot temperature reaches more than keV and the areal density

reaches more than $0.3 g/cm^2$ [3]. The thermal nuclear burn spreads in the compressed fuel by the transport of the energetic fusion reaction product alpha particles with an energy of $3.5 MeV$ as described in equation.1.3, which are expected to deposit their energy near the hot spot and cause a thermal nuclear burn wave propagating through the cold and dense fuel layer in the target shell for the further fusion reaction. It is expected that the alpha particles produced by the DT fusion deposit their energy near the hot spot and cause a thermal nuclear burn wave propagating through the cold and dense fuel layer in the target shell for the further fusion reaction. The hot spot must be confined for $\sim 100 ps$ before the expansion of the compressed target.

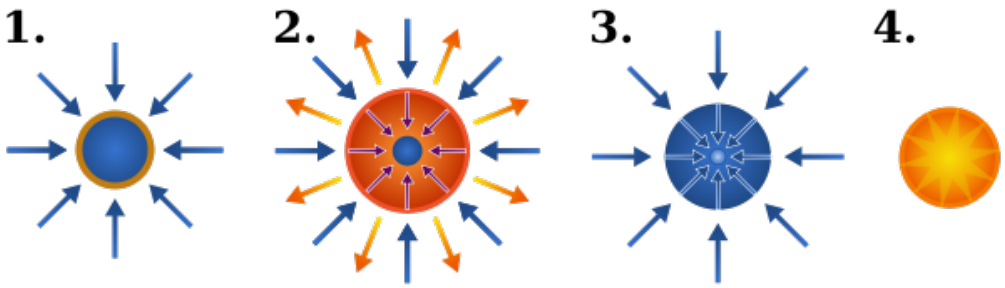

Figure 1.3: Schematic of the stages of inertial confinement fusion using lasers. The blue arrows represent radiation; orange is blowoff; purple is inwardly transported thermal energy. Images from [4]

1.3 Motivation

The current thesis will focus on the study on the structure of a shock propagating in plasma, especially the self-generated field structure associated with the shock front.

Shocks [5] are essential components in astrophysical systems [6, 7] and inertial confinement fusion (ICF) [2], especially the shock ignition configuration [8], prompting recent studies of their roles by the high energy density physics community. Despite their common occurrence, the precise shock profile - especially the associated field structures - lacks a detailed investigation. In recent years, as inconsistencies between experiments

and radiation-hydrodynamic simulations have appeared [9, 10], an appreciation of the importance of kinetic effects in shock physics [11, 12] has emerged, building on earlier Vlasov-Fokker-Planck simulations [13, 14] and particle-in-cell calculations [15]. Since then, the complexity of shocks has been revealed with the discovery of new effects such as electric current [16], charge separation [17] and electro-diffusion [18] at the shock front.

Radiation hydrodynamic codes are frequently used to predict the evolution of plasmas in inertial confinement fusion (ICF) by modeling a single average-ion species fluid and an electron fluid. However, The hydrodynamic treatment may not be sufficient in simulating the shock convergence phase of the implosion, as the ion-ion mean free path in the fuel can be comparable to the target radius because of the high temperature, low-density plasma conditions. In the case where the Knudsen number (the ratio of ion mean free path to minimum shell radius) is near unity, the kinetic theory is more appropriate than hydrodynamics to explain the underlying physics[11, 19]. To investigate the deviations from the ICF process to the hydrodynamic framework, and the impact on implosion experiments from those deviations, the development of kinetic models and new experiments to validate these models are warranted.

Recent experimental studies indicate that single-ion hydrodynamic treatment is inadequately in simulating the ICF implosions as the plasma condition becomes more kinetic and ion separation starts to take place. Deviations between experimental results and the hydrodynamic predictions exist extensively in shock drive implosion experiments. Experimental observations include unexpected yield degradation as implosion becomes more kinetic[11], thermal decoupling between ion species[10], anomalous yield scaling for different plasma mixtures[20, 9], ion diffusion[21], and ion species stratification[22].

This thesis proposes the experiments to study shock propagation in a cylindrical gas-tube along the central axis. The simplified 1-D geometry has provided valuable

insights into the underlying physics of the shock development from the observation of plasma condition, and the self-generated electric and magnetic field. As electric and magnetic fields evolve self-consistently from the plasma density, temperature, and applied pressure profiles, measurement of these fields can provide additional information about shock structures in kinetic and multiple-ion-species plasma. The impact of these electric and magnetic fields on shock dynamics and implosion performance is potentially significant but not fully understood.

In recent decades, the electric fields associated with shock fronts have attracted great attention and are widely studied with proton radiography [23, 24, 25, 26, 27]. Extensive modeling work by hybrid codes with reduced ion kinetic models[28] or kinetic codes such as LSP[29] and FPION[30], which compute the associated electric fields self-consistently at shock fronts, have provided valuable insights into the role strong shock propagation plays in species separation[15, 31] and thermal decoupling between ion species[32]. Studies using analytical theories were also widely performed for the structure of plasma shock front[13, 33, 34].

However, the tiny scale of shocks and the finite resolving power of proton probing highlights the difficulty of not only differentiating between electric and magnetic fields but also of providing a quantitative description of the field structure. As a result, the critical role played by the magnetic field has been underappreciated, and only the electric field has been included in the experimental analysis, which has resulted in an aberration of up to a couple of orders of magnitude between experiments and simulation [23]. Besides, the numerical difficulties associated with magnetohydrodynamic simulation (MHD) of shocks impose limitations on our ability to account for their effect on shock evolution [35]. Consequently, the magnetic fields associated with shocks remain unexplored both experimentally and theoretically.

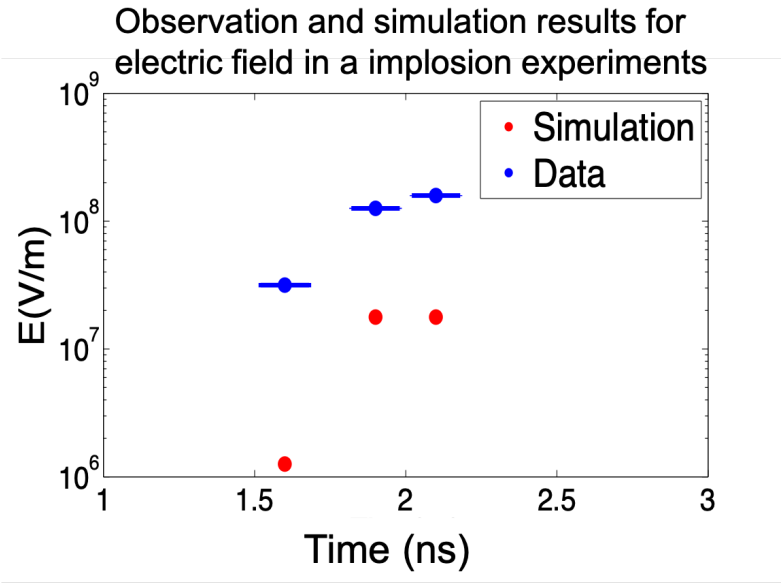

Figure 1.4: deviation between experimental observation and simulation results of electric fields in a shock driven implosion experiments in 2008. Image courtesy of C.K.Li.

These theoretical, computational studies and the gap between experimental observation and simulation results motivate the development of an innovative experimental platform for a systematic study of strong shock propagation that allows for quantitative constraint for both electric and magnetic fields as well as the comparison with simulation results. This platform has been developed on OMEGA-EP, using long-pulse lasers to drive a strong shock into a gas-cell target, while using a short-pulse laser to drive a proton backlighter to side-on radiograph the shock propagation. The gas-cell design used for this setup emphasizes minimal target mass along the radiography axis to minimize scattering effects. Similar geometries have been previously used to study shock-compressed aerogel foam[36], collision-less shocks[37] and implosions[38].

1.4 Outline of the Dissertation

Chapter 2 provides a theoretical background for the basics of plasma and laser-plasma interaction in the first section. The underlying physics of shock waves' propagation in plasma is discussed in the second section of the chapter.

Chapter 3 provides an overview of the laser facility, Omega EP Laser facility, where the experiments were performed. The motivation and experimental design are also discussed, followed by the introduction to the two primary diagnostics in this series of experiments, Proton Radiography and a soft x-ray spectrometer, VSG.

Chapter 4 mainly discusses the results from experiments on the study of field generation at the shock front in low-density gas configured in quasi-planar geometry using broad-energy proton probing. Experiments were conducted using three long-pulse laser beams with a total energy of 6.4 kJ in 2 ns for shock generation and an 850 J, 10 ps short-pulse laser to produce broadband protons for radiography. Observations of the deflection pattern of probe protons show the existence of self-generated electric fields at the shock front with the electric potential in the order of 300 V. Analytical and particle tracking methods support this conclusion.

Chapter 5 presents the observation of a magnetic field at the front of a Mach ~ 6 shock propagating in a low-density helium gas system. Proton radiography from different projection angles not only confirms the magnetic field's existence but also provides a quantitative measurement of the field strength in the range ~ 5 to 7 Tesla. X-ray spectrometry allowed inference of the density and temperature at the shock front, constraining the plasma conditions under which the magnetic and electric fields are generated. Simulations with the particle-in-cell code LSP attribute the self-generation of the magnetic field to the Biermann-battery effect.

Chapter 6 provides the measurement for spatial profiles of density and temperature

of a strong shock including the entire precursor region in a mixed gas of 90 % helium, 10 % neon and a pure neon gas using a 1-D resolved x-ray spectrometer. With comparable peak electron temperatures at the shock fronts, a precursor layer, where the electron temperature is far more than that of the ions, extends for $\sim$ 500μm in the mixed gas and less than 30 μm in the pure neon case. Because electrons are strongly collisional with two orders less mean-free path than the characteristic length of the shock, radiation–hydrodynamic simulation is performed to investigate the heat flow effect, which fails to reproduce the observed precursor pattern. PIC simulation is also performed because ion movement falls in the kinetic region. The results indicate that a group of fast-streaming ions ahead of the shock exists in the helium but not in the neon gas, contributing to lengthening the precursor layer in the helium shock. The relation between the particle collisionality and formation of those fast ions is discussed.

Chapter 7 concludes and presents future work.

1.5 Role of the Author

The radiography and spectroscopy data presented in this thesis, mostly in Chapter4, 5 and 6, came from a series of experiments performed on OMEGA EP from 2014 to 2018, which the author attended and became the principal investigator, starting to lead the experiments from 2016.

The data presented in Chapter 4 was from shots in 2014 and 2015, the time that the 50μm CH ablator was still in use. The author performed data analysis on the radiography images including quantitatively extracting the electric field from raw data, writing a particle tracking code using the C language and producing simulated radiography images for comparison and numerical calculation, performing the 2-D hydrodynamic simulation using FLASH [39] to model the shock propagation.

The data presented in Chapter 5 are from shots performed in 2016 and 2017, for which the author was the principal investigator. The author proposed the idea of using dual-angle proton radiography to recognize the field types and carried out the data analysis on the proton radiography, leading to the conclusion of the magnetic field domination at the low-density plasma shock front studied in Chapter 5.

The author observed the evidence of shock preheat from the soft x-ray data presented in Chapter 6 and carried out the data analysis, including performing the radiative atomic simulation using PRISM[40] for the shock-front condition constraints and constructing the spatial profiles of density and temperature for a plasma shock from the raw soft x-ray data, performing the 1-D radiative–hydrodynamic code for further investigation of the formation of the observed preheat region.

Chapter 2

Theoretical Background

2.1 Physics of plasma basics and laser-plasma interaction

Plasma is one of the four fundamental statuses of matter in addition to solid, liquid, and gas. It is characterized by the ionized gas that is composed of positively charged ions and negatively charged electrons. Irving Langmuir, an American chemist, and physicist is the first one to define it in the 1920s [41]. In this section, we introduce some of the essential characters of plasma and briefly discuss its interaction with intense lasers.

2.1.1 Debye Shielding

An essential characteristic of plasma is its ability to shield out the external electric field by the rapid response of electrons. Here we present an example to show the electric potential from a charged particle q, which is placed into a static plasma. Assuming the

initial background electron density is uniform, n_e. In the calculation, ions are treated as fixed background due to their exceedingly large mass compared to electrons. The electrical potential ($E = -\nabla\Phi$) is determined by the Poisson's equation:

$$\nabla^2\Phi = -4\pi q\delta(r) + 4\pi e(n_e - n_0), \tag{2.1}$$

where $\delta(r)$ is the delta function, which equals to 1 at $x = 0$ and 0 anywhere else. The charge is placed at origins for the simplicity of the calculation. Under the static assumption, the momentum equation for electron fluid can be expressed as:

$$n_e eE = -T_e \nabla n_e, \tag{2.2}$$

where an isothermal equation $p_e = T_e n_e$ has been applied. By substituting equation $E = \nabla\phi$ to Equation. 2.2, the electron density can be expressed as:

$$n_e = n_0 exp(\frac{e\phi}{T_e}) \tag{2.3}$$

Noting that $e\phi/T_e << 1$, we applied Taylor expansion formula the above equation to get:

$$\nabla^2\phi - \frac{\phi}{\lambda_{De}^2} = -4\pi q\delta(r), \tag{2.4}$$

where,

$$\lambda_{De} = \sqrt{T_e/4\pi n_0 e^2}, \tag{2.5}$$

defines the electron Debye length. By solving Equation.2.4, there is:

$$\phi = \frac{q}{r} exp(\frac{-r}{\lambda_{De}}). \tag{2.6}$$

The result indicates that the electric potential induced by the charged particle exponentially decay and becomes significantly small out of the Debye length. The equation discloses a critical feature of plasma, as mentioned at the beginning of this section. Any external electric field can be shielded out by the quick response of the electrons, maintaining the quasi-neutrality character of a plasma on the scale more extensive than a Debye length. Although ions were treated as fixed background in the derivation, they in general also contribute to the shielding on a larger time scale.

2.1.2 Plasma frequency

Electrons in plasma tend to oscillate at a particular frequency due to their light mass. In a quasi-neutral static plasma, all particles move randomly from the micro-level. If an electron deviates from the uniform ion background, the space separation between positive and negative charges will give rise to an electric field. The electric force imposed on the electron tries to drag it back, thus restoring the neutrality of the plasma. Because of such electric force, the electron moves back to its original position. Then it will overshoot due to inertia. As a result, the electrons oscillate at a particular frequency called plasma frequency, which is generally written as ω_p. This section provides in detail the derivation of plasma frequency. A couple of assumptions to simplify the calculation are: (1) the ions are fixed in space in a uniform distribution. (2) the motion of the electrons occurs in one dimension. (3) the scale of plasma is significantly larger than the electron movement. (4) no external magnetic field applied.

Firstly, we apply linearization to the mass and momentum conservation equations of electron fluid as well as Gauss law:

$$\frac{\partial n_e}{\partial t} + \nabla \cdot (n_e v_e) = 0 \tag{2.7}$$

$$mn_e\left[\frac{\partial v_e}{\partial t}+(v_e\cdot\nabla)v_e\right]=-en_eE \tag{2.8}$$

$$\nabla\cdot E=4\pi e(n_i-n_e) \tag{2.9}$$

Assuming oscillation is small compared to the collective motion of the electrons. Therefore parameters n_e, v_e and E can be considered as compositions of two parts: and equilibrium part denoted by subscription '0' and a perturbation part denoted by subscription '1':

$$n_e=n_0+n_1, v_e=v_0+v_1, E=E_0+E_1 \tag{2.10}$$

Substituting Equation.2.10 to the mass, momentum equations and Gauss law formula gives:

$$\frac{\partial n_1}{\partial t}+n_0\cdot\nabla v_1+\cancelto{0}{v_1\cdot\nabla n_0}=0 \tag{2.11}$$

$$m\left[\frac{\partial v_1}{\partial t}+\cancelto{0}{(v_1\cdot\nabla)v_1}\right]=-eE \tag{2.12}$$

$$\nabla\cdot E_1=-en_1 \tag{2.13}$$

The perturbation terms behave sinusoidally:

$$v_1=v_1e^{i(kx-\omega t)}\hat{x}, n_1=n_1e^{i(kx-\omega t)}, E_1=E_1e^{i(kx-\omega t)}\hat{x} \tag{2.14}$$

By substituting Equation.2.14 to Equation.2.7 to 2.9 and eliminating n_1 and E_1, we have:

$$\omega_{pe} = \sqrt{\frac{4\pi n_0 e^2}{m_e}} \tag{2.15}$$

This frequency, as indicated by Equation.2.15, depends only on the plasma density and typically very high due to the smallness of electron mass.

With the preknowledge of Debye length and the plasma frequency, we can give a scientific definition for plasma now. Two essential features are 'quasi-neutral' and 'collective behavior'. 'Quasi-neutral' is related to the ability of plasma to shield out the field induced by the external charged particles or electric potentials. Electrons response quickly to maintain the plasma free of enormous electric potential on the scale of Debye length. Typically, it takes only a small charge imbalance to give rise to potentials on the order of $\frac{kT}{e}$. Therefore, 'quasi-neutral' states that on the length scale that is larger than Dyebe length, the following relation stands: $n_i \approx Zn_e$

Collective behavior means motions of plasma depend not only on local conditions but also on the state of the plasma in remote regions. In neutral gases, in which particle movements are mostly affected by collisions when gravity is neglected due to its smallness. Consequently, the motion of neutral gases obey the hydrodynamic formulas. In contrast in plasma, the local concentration of positive and negative charges can occur, which give rise to electric field as well as magnetic field by electric current. The charged particles in the plasma from a remote region could be affected by the electric and magnetic field as the Coulomb force is a long-distance interaction. Therefore, plasma on a large length scale can respond collectively to the applied electric and magnetic forces. For the collective behavior to be valid, two requirements posted are: firstly, the length scale of the studied plasma is much larger than the Dyebe length; secondly, much more than 1 particle are required within a Dyebe sphere (a sphere of the radius equal to the Dyebe length). Those could be written as: (1).$\lambda_D << L$, where λ_D is the Dyebe

length and L is the length scale of the plasma. (2).$N_D >> 1$, where N_D is the number of electrons within a Dyebe sphere as $N_D = n_e \frac{4}{3}\pi\lambda_D^3$.

Besides, the frequency of collisions with neutral particles has to be smaller than the plasma frequency to ensure that the electromagnetic rather than hydrodynamic force governs the motion of the particles. The formal equation is written as: $\omega_{pe}\tau > 1$, where τ is the mean time between collisions with neutral atoms

2.1.3 Laser plasma interaction

We discuss the fundamental physics of laser-plasma interaction in this section. Though it is not the focus of the current thesis, it plays a crucial role in the study of inertial confinement fusion. Laser-produced plasmas have many applications. In the longer pulse regime, there are studies of thermodynamic and optical properties of matter at very high density and pressure[42, 43], inertial confinement fusion (ICF) [44, 45], the simulation of astrophysical processes in the laboratory[46, 47], coherent and incoherent X-ray sources[48]. Plasmas produced by ultrashort and ultraintense laser pulses can be used as intense sources of particles and photons (relativistic electrons, MeV ions, positrons, X-rays and gamma-rays, neutrons, etc.) and for particle acceleration[49, 50, 51].

We start with introducing the dispersion relation for electromagnetic waves in a plasma with a uniform density.

$$\omega^2 = \omega_{pe}^2 + k^2c^2 \tag{2.16}$$

where ω is the frequency of the electromagnetic wave, ω_{pe} is the electron plasma frequency defined in Equation. 2.15. k is the wave number, and c is the light speed.

It is worth noting that ω_{pe} defines the minimum frequency of a light wave

propagating in a plasma. When ω is smaller than the electron plasma frequency, k becomes imaginary. Because the characteristic response time of plasma is inversely proportional to the electron frequency, $\frac{1}{\omega_{pe}}$, the electrons in plasma can shield out the electromagnetic field of a light wave when $\omega < \omega_{pe}$.

In other words, since ω_{pe} depends only on the plasma density, the relation $\omega = \omega_{pe}$ provides the maximum plasma density in which a light wave can penetrate. This density is called critical density:

$$n_{crit} = \frac{m_e \omega^2}{4\pi e^2} \tag{2.17}$$

which can be expressed in terms of the free-space wavelength of the light wave in the units of microns, λ_μ:

$$n_{crit} = \frac{1.1 \times 10^{21}}{\lambda_\mu^2} cm^{-3} \tag{2.18}$$

Because the laser light can not penetrate further into the overdense plasma, where $n_e > n_{cirt}$, the absorption and reflection happen mostly in the underdense plasma, where $n_e < n_crit$. The majority of energy carried by the light wave is absorbed near the critical density. Therefore, the electrons in the plasma near the critical density are heated up by the interaction with the incoming light wave. Afterward, some of the energy is transported into the overdense plasma region by electron thermal region. Some of it is transported to ions through electron-ion equilibration.

2.2 Basics of Shock Waves

The shock phenomenon is a fundamental concept in high-energy-density physics (HEDP) and is common in astrophysical systems. This phenomenon has been studied

with significant effort for deep insights into astrophysical and ICF plasmas. Discrepancies between experimental results and hydrodynamic predictions have been revealed by many implosion experiments [21, 9], which point toward the underlying kinetic effects in ICF physics. Besides, it has been suggested that the role of charge separation potentials is important in supernova remnant shocks[52]. Thus, investigation of a shock wave propagating in plasma is warranted.

In this section, we provide an overview of a shock wave by deriving its structure from the traditional hydrodynamic equations. A shock wave forms when the velocity of the propagating material is faster than the speed of sound in the material. The fast-traveling sample will rapidly compress material and cause discontinuities in the sample in terms of density, temperature, and pressure.

To calculate the quantitative math for the structure of a shock, we adopt the conservation equations of mass, momentum, and energy, which can be formally written as:

$$\frac{\partial \rho}{\partial t} = -\frac{\partial \rho u}{\partial x}, \tag{2.19}$$

$$\frac{\partial \rho u}{\partial t} = -\frac{\partial \left(p + \rho u^2\right)}{\partial x}, \tag{2.20}$$

$$\frac{\partial (\rho \varepsilon + \rho u^2/2)}{\partial t} = -\frac{\partial \left[\rho u(\varepsilon + u^2/2 + p/\rho)\right]}{\partial x}, \tag{2.21}$$

in which ρ is the density, u is the velocity of the shock, p is pressure and ε is then energy density of the sample.

The condition relationship on the two sides of the shock surface can be derived

from the above equations as:

$$\rho_1 u_1 = \rho_0 u_0, \tag{2.22}$$

$$p_1 + \rho_1 u_1^2 = p_0 + \rho_0 u_0^2, \tag{2.23}$$

$$\varepsilon_1 + \frac{p_1}{\rho_1} + \frac{u_1^2}{2} = \varepsilon_0 + \frac{p_0}{\rho_0} + \frac{u_0^2}{2}, \tag{2.24}$$

where subscript 0 denotes the parameters for the unshocked material (upstream of the shock) and 1 denotes the parameters for the shocked material (downstream of the shock).

From the relationship defined by the above equation, one can derive the Hugoniot curve of the shock, describing the relation between pressure and density on both sides of the shock front. Derivation of the Hugoniot relation requires the preknowledge of other variables besides pressure and density, which raises difficulties in some real applications.

To simplify the problem, we discuss the shock structure defined by the above conservation equations in a perfect gas with constant specific heat.

2.2.1 Shock waves in ideal gases

A perfect gas is characterized by known hydrodynamic relations and entropy expression:

$$\begin{aligned} \varepsilon &= c_v T = \frac{1}{\gamma - 1} pV, \\ h &= c_p T = \frac{\gamma}{\gamma - 1} pV, \end{aligned} \tag{2.25}$$

in which h is the specific enthalpy of the ideal gas, c_p is the isobaric specific heat and c_v is the isochoric specific heat, γ is the ratio of the specific heats, which equals c_p/c_v.

Substituting the above relations into equation2.22 to 2.24 enables the derivation for an explicit formula of the Hugoniot relation in an ideal gas:

$$\frac{p_1}{p_0} = \frac{(\gamma+1)V_0 - (\gamma-1)V_1}{(\gamma+1)V_1 - (\gamma-1)V_0}, \tag{2.26}$$

as well as density and temperature relations behind and beyond the shock front:

$$\frac{T_1}{T_0} = \frac{p_1 V_1}{p_0 V_0}, \frac{\rho_1}{\rho_0} = \frac{\gamma+1}{\gamma-1}, \tag{2.27}$$

From these, the shock compression for a monatomic gas with $\gamma = 5/3$ can be calculated to be 4.

In gases, the temperature can be raised to as high as $\sim 100eV$ when the shock velocity reaches $\sim 100km/s$, which causes ionization of the gas and forms a plasma environment. In the plasma, electrons and ions behave differently due to the difference in their masses, which possibly complicates the structure of a shock front and gives rise to the electric and magnetic fields.

In addition to the confinement fusion system, plasma shock waves broadly exist in astrophysical environments.

2.3 Shock Wave propagation in Plasma

This section provides the fundamental theory of the current thesis, the shock wave propagation in plasma and the self-generation of the associated electric and magnetic fields. For a shock propagating in plasma, some features that are absent from the shock in neutral gases arises from the unique characters of plasma. Due to the enormous difference

between an electron and ion mass, they are treated as two different fluids rather than one and have their behavior independently to some extent. Besides, due to the unique structure at a shock front, the electric field by charge separation as well as the magnetic field due to the Biermann Battery effect can be generated. In the condition where shocks travel at high velocities, the ions gain significant kinetic energies. The ion means free path can increase significantly accordingly and become comparable to the characteristic scale of the shock eventually. In such a case, hydrodynamic treatment is inadequate anymore, and kinetic theory must be taken into account.

Traditional hydrodynamic theory of a plasma shock consists of three layers: the ion and electron equilibrium layer close to the downstream (hot side), the compression ion shock layer in which density drops dramatically and the precursor layer which is featured by heated electrons and cold ions [53, 12]. The length of both the equilibrium and precursor layes are $\sim \sqrt{m_i/m_e}\,\lambda_{ii}$ (where m_i and m_e are the ion and electron masses, respectively, and λ_{ii} is the ion-ion downstream mean free path), whereas compression region is a few ion-ion mean free paths in length.

2.3.1 Shock without electron heat conduction

For simplicity, we first study the case where electron heat conduction does not differ from ion heat conduction. The studied shocks are assumed to be strong ones, in which particles have been pre-ionized before shock arrival; therefore ionization process is not considered in the calculation.

When a piston compresses the plasma with extremely high speed, ions in the plasma gain kinetic energy on the order of $\sim m_i U_{shock}^2/k$, where m_i is the mass of the ion, U_{shock} is the shock velocity and k being the Boltzmann constant. The length scale of the density jump, which makes up the embedded ion shock region is determined by

the ion-ion collision time τ_i, being on the order of couple ion-ion mean free path λ_{ii}. When encountering cold ions, the hot ions with larger kinetic energies transfer moderate amounts of energy in each collision and reach equilibrium with the cold ions within a couple of times of collisions. However, during the equilibration process among ions, they transfer only a small amount of energy to electrons, due to the exchange time between ions and electrons τ_{ie} is on the order of $(\frac{m_i}{m_e})^{1/2}\tau_{ii}$, which is at least 43 (for protons) times slower than the ion-ion collision time. Therefore equilibrium between ions and electrons takes a much longer time than that between ions. Within the embedded shock region, a nonequilibrium condition between ions and electrons is maintained. Because of the shock compression, electrons at the shock front get the same amount of velocity as ions, which is roughly equal to the shock velocity. An increase in electron thermal energy is $m_e U_{shock}^2/k$, which is much smaller than ion thermal energy due to its lightness. Therefore, electrons at the embedded ion shock layer exhibit a lower temperature in comparison with ions.

Behind the shock, electron and ions will eventually come to equilibration within a length scale on the order of $(\frac{m_i}{m_e})^{1/2}\lambda_{ii}$ depending on the thermal energy exchange time τ_{ie}. The structure of a shock propagating in plasma is shown as Fig.2.1 without consideration of the electron heat conduction, on which Δx represents the scale length $(\frac{m_i}{m_e})^{1/2}\tau_{ii}$ over which ions equilibrate with electrons in terms of temperature.

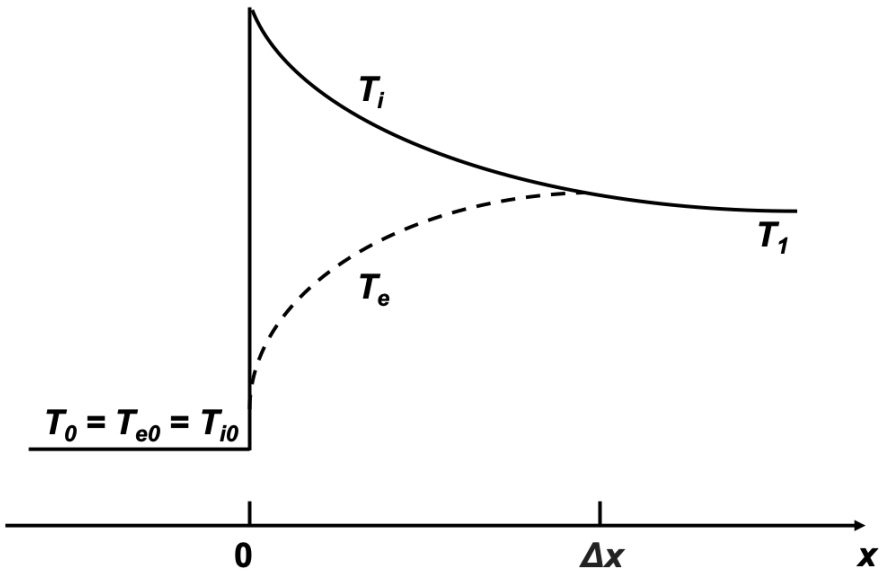

Figure 2.1: Ion and electron(dashed line) temperature profiles in a shock front in a plasma without taking into account electron heat conduction.

In spite of the nonequilibrium over electrons and ions, the plasma remains quasi-neutral on the scale of comparable or larger than Debye length due to the electric interaction between ions and electrons together. When electrons try to escape from ions, even a small displacement gives rise to a large electric field, thus preventing further separation.

2.3.2 Shock with electron heat conduction

Now we take into consideration the impact of electron heat conduction on the shock front structure. We start by calculating the thermal diffusivity for both ions and electrons as well as the scale length over which their impacts are significant.

The transport coefficient, for the atom thermal diffusivity, is on the order of $\chi \sim \lambda_{ii} v_i/3$, where χ is the thermal diffusivity, λ_{ii} is the ion-ion mean free path and v_i is the ion thermal velocity. Therefore the characteristic diffusion length is on the order of $\lambda \sim \chi/U_{shock} \sim \lambda_{ii} v_i/U_{shock}$. As discussed above, the ion thermal velocity is on the order

of shock velocity. Thus the characteristic diffusion length for ions being on the same order of the ion-ion mean free path λ_{ii}.

The coefficient of electron thermal diffusivity χ_e is on the order of

$$\chi_e = \frac{l_e v_e}{3},$$

where l_e is the electron mean free path and v_e is the electron thermal velocity. The mean free path is independent of particle mass and depends only on their temperature and charge state, which can be expressed as $\lambda \sim T^{3/2}/Z^2$. When the ion and electron temperature reach equilibration, the electron mean free path is on the same order of (for ions that charge states are equal to one) or large than (for ions that charge states are larger than one) ion mean free path.

At temperature equilibrium, the electron thermal velocity is larger than ion thermal velocity by a factor of $(m_i/m_e)^{1/2}$. Therefore, the characteristic scale over which the electron heat conduction can take place is on the order of

$$\lambda_e \sim Z^2 \frac{\chi_e}{U_{shock}} \sim (Z^2 \frac{m_i}{m_e})^{1/2} \lambda_{ii}$$

This length scale is larger by a factor of Z^2 than the thickness of the equilibrium layer over which the electron temperature becomes comparable with ion temperature behind the shock, which is:

$$\Delta x \sim U_{shock} \tau_{ie} \sim U_{shock} (\frac{m_i}{m_e})^{1/2} \tau_i \sim (\frac{m_i}{m_e})^{1/2}$$

Therefore, within the equilibrium layer between electrons and ions behind the shock front, the electron heat conduction is the same important as the energy exchange between ions and electrons.

One thing worth noting is that this fact is fundamental because it gives rise to the existence of a preheating layer ahead of the shock front. With the thermal velocity

comparable with the shock velocity, the hot ions cannot move too far ahead of the compression shock layer. However, being extremely light, the thermal velocity of electrons is much larger than the shock velocity by a factor of $(\frac{m_i}{m_e})^2$, which is at least 36 times. They can travel ahead of the compression shock layer (which is on the order of couple ion mean free path) and heat the background electrons as well as ions that before the arrival of the compression shock. A preheating layer is thus formed up. In this layer, the electron temperature is higher than ion temperature, since the efficiency of energy exchange between electrons is much higher than that between ions and electrons. Therefore, a sharp gradient in ion temperature at the front of the compression shock layer takes place while the electron temperature keeps a more smooth slope due to the significant heat conduction that prevents discontinuous changes.

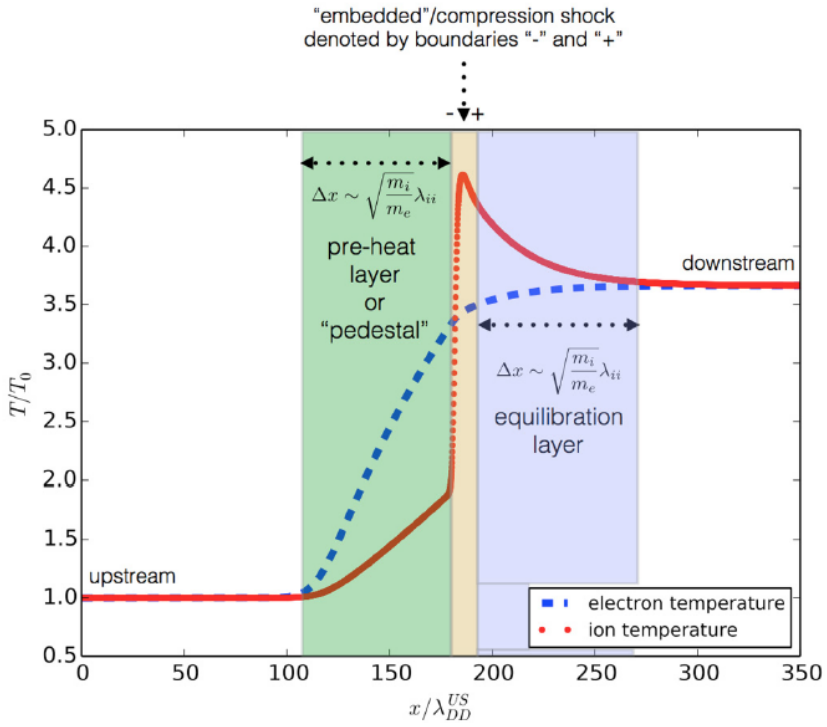

Figure 2.2: Ion and electron(dashed line) temperature profiles at a shock front in a plasma with the electron heat conduction taken into account. Image courtesy of Keenan [54]

Fig.2.2 displays a general shock structure in plasma when electron heat conduction is taken into consideration.

Let's estimate the scale length of the preheating layer now. For simplicity, we assume that the gas ahead of is not compressed and the energy transport from the heated electrons to the ions ahead of the shock is negligible. The electron heat conduction flux is:

$$S = -\kappa_e \frac{dT_e}{dx} = -\chi_e c_{ev} \frac{dT_e}{dx}, \tag{2.28}$$

where $\kappa_e = \chi_e c_{ev}$ is coefficient of the thermal conductivity and c_{ev} is the isobaric specific heat. The effective coefficient of electron thermal conductivity is:

$$\kappa_e = \xi \frac{(kT_e)^{(5/2)}k}{m_e^{1/2} Ze^4 ln\Lambda} \tag{2.29}$$

where $ln\Lambda$ is the Coulomb logarithm, and ξ is a number which depends only weakly on Z;

Given this a quasi-static process, the heat conduction flux in the preheating layer is equal to the hydrodynamic flux of electron energy:

$$S = -U_{shock} c_e T_e = -\chi_e c_e \frac{dT_e}{dx} \tag{2.30}$$

Noting that $\chi_e \sim v_{ethemal} l_e \sim T_e^2$, which can be written as $\chi_e = aT_e^2$, where a is a constant. by integrating 2.30, we have:

$$d_{preheat} = \frac{2}{5} \frac{a}{U_{shock}} T_e^2 = \frac{1}{2} \frac{\chi_e(T_e)}{U_{shock}} \tag{2.31}$$

T_e here is the electron temperature at the compression shock layer, which is on the same order as that in the equilibrium layer behind the shock when electron heat conduction

is taken into account. Therefore, the thickness of the preheating layer ahead of the compression shock layer is on the same order of the thickness of the equilibrium layer behind the compression shock layer:

$$d_{preheat} \sim \frac{\chi_e}{U_{shock}} \sim \frac{v_e \lambda ee}{U_{shock}} \sim (\frac{m_i}{m_e})^{1/2} \lambda_{ii}$$

2.3.3 Electric field Generation at Shock Front

At a plasma shock front, where dramatic density drop occurs, huge gradients are also present along with temperature and pressure profiles. Due to the higher mobility of electrons, they tend to be pushed further along the shock propagation direction due to the imposed pressure at the shock front. Due to the huge difference in mass, spatial charge separation between electrons and ions can be built up, consequently giving rise to an electric field. This electric field tends to keep the electrons from further separation with ions, thus restoring the quasi-neutrality of the plasma. When it comes to a quasi-equilibrium state, the electric force by the self-generated field and the imposed pressure by the shock reach balance on the electrons.

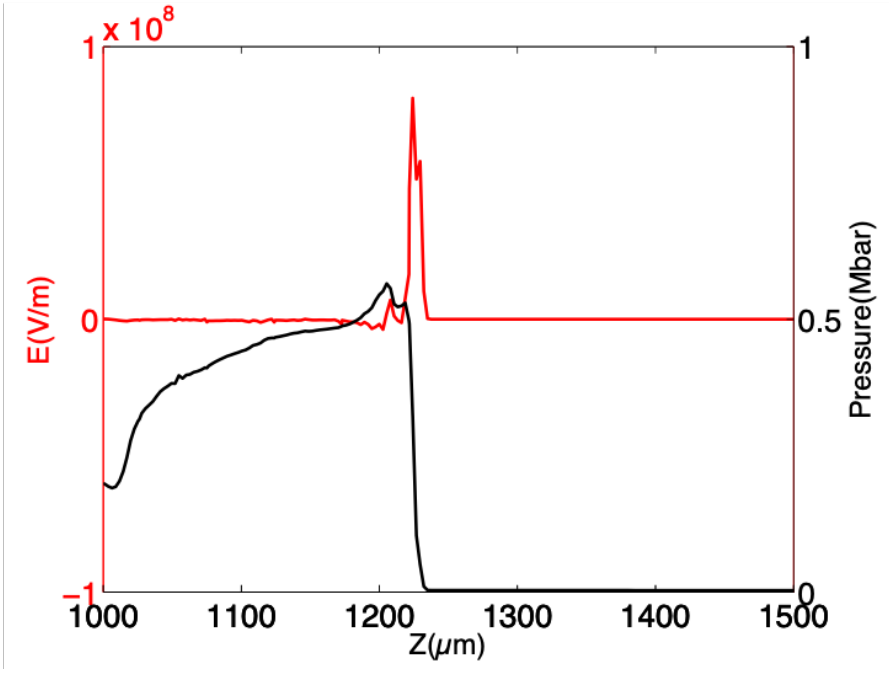

Figure 2.3: FLASH simulation for self-generated electric field profile (in red) at a shock front. The shock propagtes from left to right. The black curve plot the pressure profile, along which a dramatic drop is observed at the shock front.

Fig.2.3 shows an example of a shock front that characterized by the sharp gradient in electron pressure and a self-generated electric field. On the plot, a shock is propagating from left to right, and the shock front is recognized by the dramatic drop in electron pressure, which is plotted in black. The profile of the electric field in V/m is plotted in red, along which a peak is observed at the shock front.

The generation of such an electric field is attributed to the gradient in electron pressure present at the shock front. Despite both ions and electrons are imposed by the considerable pressure. Due to the exceedingly small mass, free electrons can be pushed slightly ahead of ions, resulting in spatial charge separation. Because of such separation, an electric field is built up, which tries to restore the neutrality of the plasma. Due to the self-generated electric field, the electrons cannot go too far from ions because of the restoring electric force by the field. A balance is reached at some distance. Formal math for the above description comes from the generalized Ohm's law, in which plasma is

treated as two fluids, ions, and electrons:

$$E + v_i \times B = \frac{j}{\sigma} - \frac{\nabla P_e}{en_e} + \frac{1}{en_e} j \times B + \frac{m_e}{e^2} \frac{\partial}{\partial t} (\frac{j}{n_e}) \tag{2.32}$$

where v_i is the ion thermal velocity, σ is the electric conductivity, j is current, P_e is the electron pressure and n_e is the electron density. The terms involving j and B typically vanish for zero external magnetic fields and do not spontaneously generate a field, leading to the simplified formula:

$$E = -\frac{\nabla P_e}{en_e} \tag{2.33}$$

Equation 2.33 provides the relation of the electric field intensity at a specific location given the pressure gradient and electron density there.

Next, we focus on the derivation of the potential of the entire electric field, which is on the order of electron thermal energy (its temperature). When the electrons of higher mobility move further along the shock propagation and separate with ions, they are slowing down by the restoring electric force and lose all their energies at some point. Therefore, the electric field vanished at the point when the electrons lose all their thermal energy. In other words, the potential of the self-generated electric field is on the order of the electron thermal energy. Together with the correction term from diffusion that is corresponding to the density jump at the shock front, the potential can be written as:

$$\Delta\phi \approx (k_B T_e / e) \ln(\rho_2 / \rho_1) \tag{2.34}$$

where, ρ_1 and ρ_2 are the densities of shocked and un-shocked materials.

2.3.4 Biermann battery effect and magnetic field generation at shock front

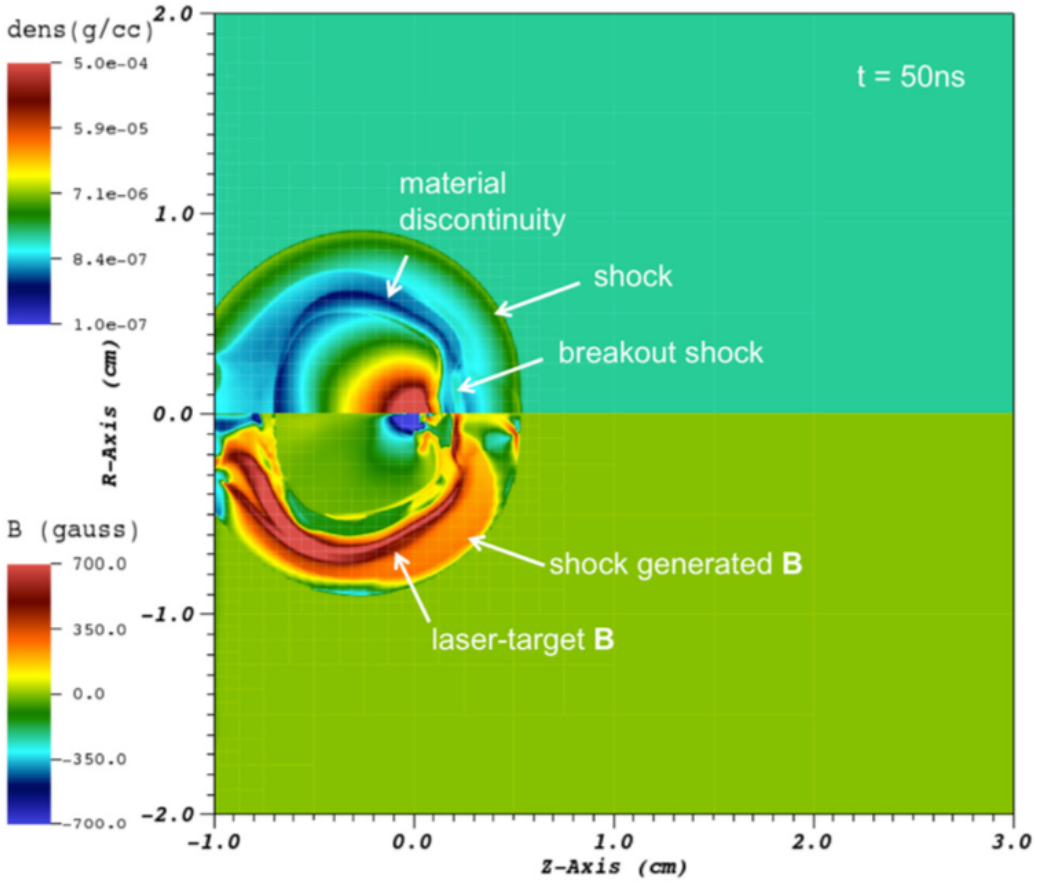

Figure 2.4: FLASH simulation results for density profile (top) and magnetic map (bottom) at a shock front. The shock was launched by the expanding plasma from a carbon rod pushing into the surrounding. The plasma was created by laser irradiating on the carbon rod. Image courtesy of Tzeferacosa.

Simultaneous generation of the magnetic field takes place in the plasma as well when un-parallel components between gradients in density and temperature exist. A mathematical expression can be derived by substituting 2.33 into the Maxwell-Faraday equation, which states that a time-varying magnetic field always accompanies a spatially

varying (also possibly time-varying), non-conservative electric field, and vice versa.

$$\nabla \times E = -\frac{\partial B}{\partial t} \tag{2.35}$$

It produces the Biermann Battery equation:

$$\frac{\partial B}{\partial t} = \frac{1}{en_e} \nabla T_e \times \nabla n_e \tag{2.36}$$

where $p_e = n_e \cdot T_e$. It is worth noting that, the equation is independent of external magnetic field. Therefore, this source can generate magnetic field as long as there are temperature and density gradients that are not parallel.

The detailed explanation of this generation mechanism uses the fact that our two charged species have very different masses. If there is a pressure gradient in the plasma, the particles become accelerated. The electrons gain greater acceleration than the protons due to their smaller mass. If the electron density n_e is constant in space, the electric field stays static. However, the spatial dependence of n_e gives rise to an electric current and thus to the generation of a magnetic field [55, 56].

An example of self-generated magnetic field at a shock front is shown in Fig. 2.4 [57]. The images show the results by FLASH simulation for the 2D density and magnetic profiles. The shock was created by laser illuminating on a cylindrical carbon rod. In the shock expansion, the density evolution, determined by advection and the temperature evolution, determined by thermal diffusion, obey different physical processes and therefore eventually evolve into different spatial distributions during the shock propagation. The unparallel components in density and temperature give rise to the growth of a magnetic field.

The primary work of this dissertation is concerned with the characterization of

the electric field as well as the magnetic field at the shock front in plasma to help better understand the underlying physics of the shocks propagating in plasma.

Chapter 3

OMEGA EP Laser Facility and the

Experimental Design

3.1 Overview of OMEGA EP Laser Facility

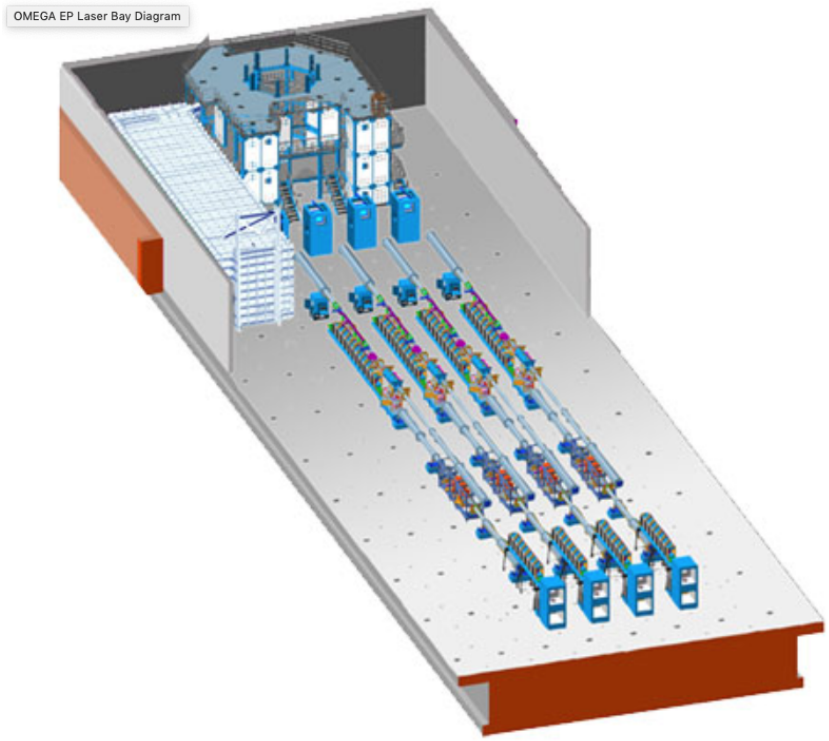

Figure 3.1: A 3D model of the Omega EP Laser Facility at the Laboratory for Laser Energetics

The OMEGA EP (extended performance) Laser System is in operation since 2008. It is an extension of the 60-beam UV OMEGA Laser System. OMEGA EP has four, frequency-tripled (wavelength ~ 0.35 μm), kilojoule class, independently configurable beamlines. Two of these can be compressed to a petawatt-class short pulse. A flexible diagnostic system is applied to the facility. The combination of high intensity and high energy in short-pulse and long-pulse operation and the diagnostic systems enables

a wide range of experimental configurations for cutting-edge plasma, high-field, high-pressure materials, and high-energy-density (HED) research as well as the development of advanced radiation sources for applications. A full-system shot cycle takes approximately 1.5 hours. It is typical to have 7 to 8 shots per day. Besides, interleaved beam operation on a 45-minute shot cycle is possible for compatible experiments with 2$\times$ more shots per day.

OMEGA EP beams 1 and 2 can be compressed for short-pulse operation. From the fiscal year 2019, these beams can provide 1.053 μm light with different pulse durations: up to 0.5 kJ in 0.7 ps, 1.25 kJ in 10 ps, and 2.3 kJ in 100 ps The best focus is of $\sim$ 30 μm diameter containing 80% of laser energy. The peak laser intensity is above 2 $\times$ 10^20 W/cm^2, with an intensity contrast of approximately 1000. Other pulse durations between 0.7 ps to 100 ps can also be available. The two short-pulse beams can be operated together to propagate along two perpendicular off-axis parabolas in the OMEGA EP target chamber, or combined to co-propagate along a single ”backlighter” axis. OMEGA EP beams 3 and 4 can provide simultaneous long-pulse operation for target preconditioning in any short-pulse configuration The short-pulse Beam 2 (and Beam 1 in co-propagation mode) can also be transported to the OMEGA chamber for joint operation with the OMEGA 60 laser.

All four OMEGA EP beams can provide long-pulse (0.1 ns to 10 ns) operation to the OMEGA EP target chamber. In this mode, the beams provide frequency-tripled light (0.351 μm) in individually configured pulse shapes containing up to 5 kJ. Distributed phase plates are used to produce smooth super-Gaussian focal spots with diameters of 400 to 2000 μm. The best focus without the distributed phase plates produces a spot size of 100 μm.

A wide range of flexible diagnostic systems is available for experiments at the OMEGA EP chamber. Three dedicated Target Positioning Systems enable control for

multi-target geometries. Five ten-inch manipulators (TIMs) provide a standardized fielding platform compatible with over 30 instruments, in addition to many fixed-port diagnostics. Commonly used techniques include gas-jet plasma generation, externally generated magnetic fields up to 50 T, x-ray imaging, spectroscopy and radiography, proton radiography, electron/positron, and ion spectroscopy, powder x-ray diffraction, velocimetry (VISAR) and streaked optical pyrometry (SOP), and 4ω optical probing.

3.2 Experimental design

In this section, we discuss the experimental design of a side-on proton radiography platform to study the self-generated electric and magnetic fields at plasma shock fronts using the OMEGA EP Laser Facility. The deviation between the experimental observations and simulation results as well as the lack of studies for the associated magnetic field necessitate the development of such a platform. Details about the design have been published in Ref.[58].

3.2.1 Experimental setup

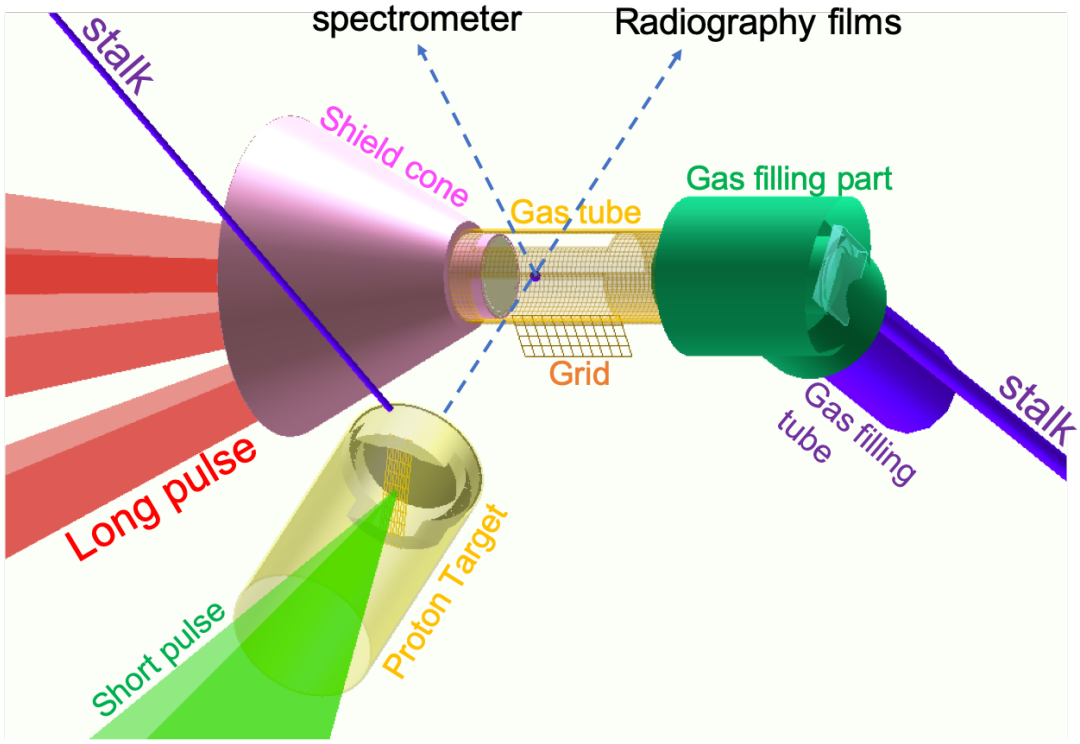

Figure 3.2: Schematic of the proton radiography system setup. The shock is generated by long pulse laser beams irradiating on the ablator. A beam of protons is generated by a short pulse laser beam illuminating on a thin metal foil (40μm). They travel through the objective and deposit on a stack of radiographic films placed on the other side. Two windows on the gas tube were designed to reduce stopping along the proton path. A soft-Xray spectrometer was placed to record the self-emission from the plasma at the shock front through a 1 μm window.

Up to three long-pulse ultraviolet (UV) laser beams are available to drive a strong shock by the ablation of a piece of plastic or glass foil. For OMEGA-EP long-pulse laser parameters (using 1-ns duration and 400μm focus), the laser intensity can be as high as $310^15W/cm^2$ using all three long-pulse beams. Using the interaction of the OMEGA-EP short-pulse infrared laser, a beam of protons can be generated by high-intensity laser foil interaction through the TNSA(target normal sheath acceleration) mechanism.

A schematic experimental platform studied in this thesis is shown in Fig.3.2.

Three long pulse UV beams were used to drive a strong shock by the ablation of a piece of foil located on the left side of the tube. Two options for the foils used in this platform are either a 50μm thick CH plastic or a 2μm thick SiO_2 glass. Details of the gas target configuration are discussed in section 3.2.3. The proton beam axis is perpendicular to the gas tube axis. The proton backlighter foil is positioned 7.5 to 8 mm away from the center of the gas cell and typically driven with the short-pulse laser at best focus, at different delays relative to the long pulse driver. The radiochromic film (RCF) pack is positioned 8 cm20 cm away from the center of the gas cell on the opposite side, depending on the desired magnification. The entire RCF pack has a broadband spectral coverage from 3 to 30 MeV. Each film was sampling a different energy range (separated by 1 to 3 MeV) and having a narrow bandwidth (0.1 MeV). Details is present in Sec.3.3.1.

The proton target is a cylinder containing two foils spaced 1 mm apart. The first foil, typically 3μm thick tantalum, shields the second foil, typically 40μm copper, from target plasmas. The short-pulse laser focuses on the second foil to produce the TNSA protons for radiography.

The gas cell is a 5 mm long, 1.8 mm diameter tube with 50μm thick Kapton wall. Two 2.5 mm by 1.5 mm rectangular windows along proton trajectories are laser-cut along the Kapton tube and patched over with 1μm thick Kapton film to minimize stopping to probing protons. Another 2.5 mm by 0.5 mm window on top is open to increase the X-ray transmission rate to a soft X-Ray spectrometer. A mesh is attached outside the gas cell to provide spatial fiducials. At the other end, a gas plug with a tube attached to the gas station was placed for gas filling before each shot. Gases used were typically helium, neon, and argon.

Experimental spatial resolution is $\sim$ 30μm for proton energies $\sim$ 15 MeV, as inferred from radiograph images of the Cu mesh attached to the gas cell. The bar width of the Cu mesh is 55μm, and the whole width of the Cu mesh is 285 m. The resolving

power increases along with the proton energy. The spatial resolution is estimated from the full-width-half-maximum of the mesh bars as they appear on proton radiographs of different energies.

Using this configuration, shock strength (and temperature) can be tuned by either varying the drive laser energy or changing the ablator material. Variation of the shock strength allows proton radiography of the shock front as a function of relevant plasma parameters. Experiments on this platform have radiographed shock-front propagation in pure helium and neon at different times and different drive intensities. It also studied shock propagation in binary plasma mixture of helium and neon of different compositions. Those experimental results will be discussed in details in Chap4, 5 and 6.

3.2.2 Gas cell design

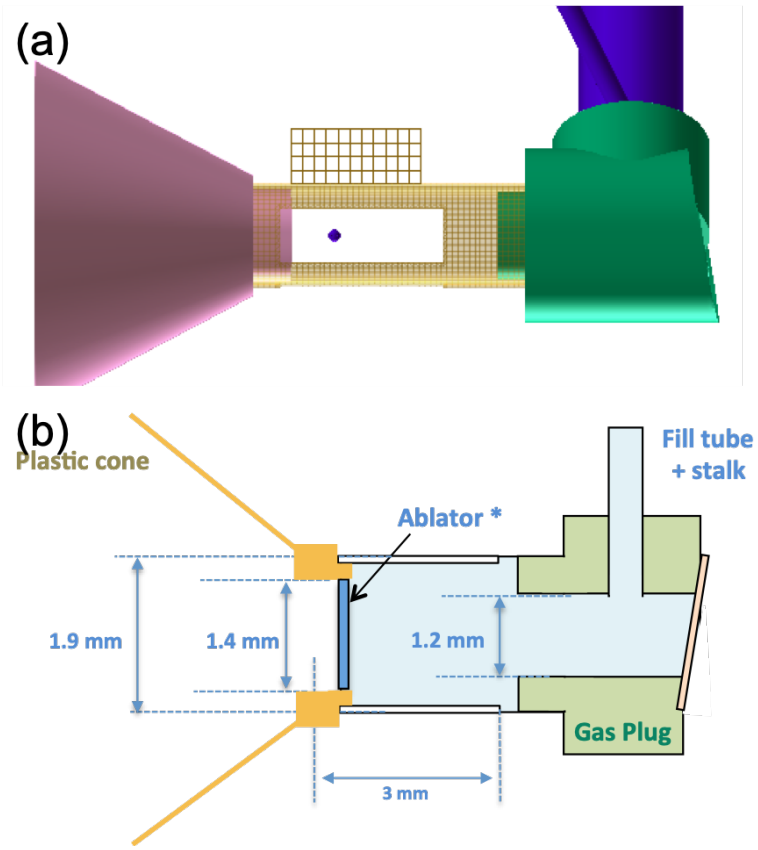

Figure 3.3: Cross sectional view of the gas target along proton path.

A cross sectional view along the proton path of the gas cell target is shown as Fig.3.3. The shielding cone is made of engineering plastic that is of better mechanical and thermal properties compare to the widely used commodity plastic (such as polystyrene). A washer housing the ablator is attached to the narrower end of the shielding cone, connecting it with the cylindrical tube. The ablator is $\sim 1.4mm$ in diameter in adaption to the inner diameter of the washer. The material of the ablator was improved from a 50μm CH to a 2μm SiO_2 for the generation of stronger shock. The cylindrical tube is made of Kapton with the outer radius $1.9mm$ and wall thickness 50μm. A gas plug shown in green, attached to the other end of the tube, was connected to the gas station for filling

before each shot. Helium or neon gases were typically filled $\sim$ 5 minutes before shots to ensure the required gas pressure

3.2.3 Proton target design

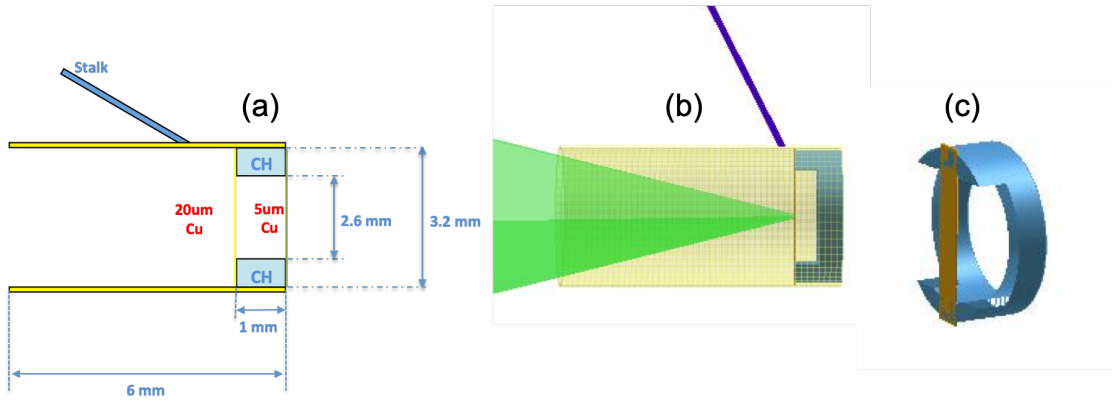

Figure 3.4: Cross sectional view of the proton target.

A cross-section view and a 3D diagram of the proton target is shown respectively in Fig.3.4(a) and (b). The main components of the proton target are two metal foils separating from each other by $\sim$ 1mm. They are housed by a plastic washer shown as Fig.3.4(c), of which the inner diameter is 2.6 mm and the outer diameter is 3.2 mm. A rectangular volume cut the washer for alignment purpose. The metal foil for proton generation usually is a slice of 40µm copper that is suitable for the TNSA mechanism when illuminated by short laser pulses. The duration of the laser is on the order of ps and the intensity can reach $10^{18}\mathrm{W/cm^2}$. A shielding foil is placed in front of the copper to protect it from the debris, which is usually a 3µm titanium. The entire washer was protected by a Kapton cylindrical tube around 6 mm long with a wall thickness of 50µm. A stalk connecting the proton target to the OMEGA EP chamber is shown in purple.

3.3 Diagnostics

This innovative experimental platform adopts two principle diagnostics, proton Radiography, and X-ray spectrometer. Proton Radiography diagnoses the electric and magnetic fields as the charged particles are sensitive to the existence of fields. A soft-Xray spectrometer called VSG (variable line spacing grating) was used to record the self-emitted X-ray light from the shock front, thus inferring the temperature and density of the plasma for the generation of the electric and magnetic field. A detailed discussion of those diagnostics is provided in this section

3.3.1 Proton Radiography

The most important diagnostic is proton radiography in this platform. The proton beams were generated by the interaction between a short-pulse laser with a piece of thin metal foil via the TNSA (Target Normal Sheath Acceleration) mechanism. After generation, the protons were sent to the shock front area to probe the self-generated electric and magnetic fields. After traveling through the gas-cell area, the protons were collected by a stack of radiographic films that were placed along their paths at a distance $\sim$ centimeters from the gas-cell.

Proton radiography is a technique widely used in laser-plasma interaction and inertial confinement fusion relevant experiments for electric and magnetic field detection. The whole system is composed of three primary parts: proton source, probing objective and the detector. Energetic protons are generated via the TNSA mechanism, as discussed in the following section 3.3.1.1. The probing objective in this study is the self-generated electric field and the magnetic field associated with a shock traveling in the plasma environment. Those fields are going to be discussed in details in chapter 4 and 5. The detector is typically a stack of radiochromic films or CR-39 films[59]. The full discussion,

including the mechanism for TNSA protons, and calibration of the radiographic films are provided in this section.

3.3.1.1 TNSA protons

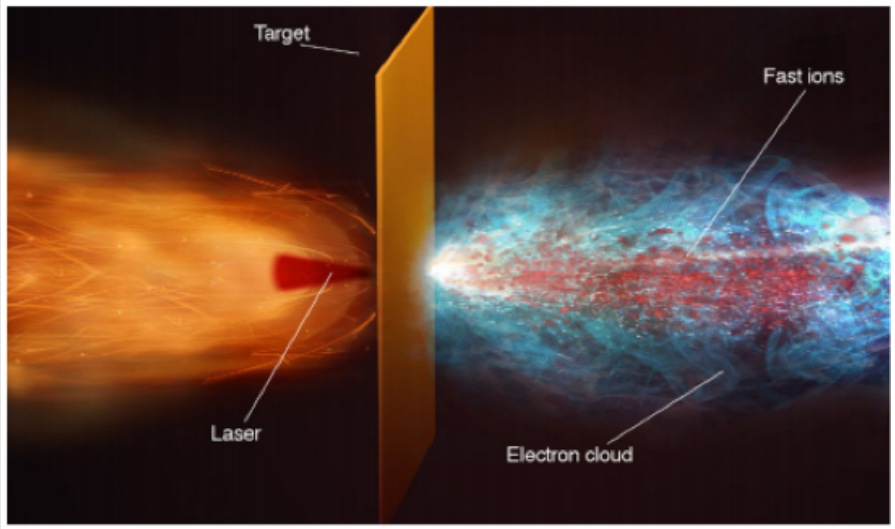

Figure 3.5: A 3D diagram qualitatively showing the TNSA (Target Normal Shealth Accelaraion) proton scheme.

The mechanism of target normal sheath acceleration (TNSA) for ion beam generation has attracted significant attention in recent decades. Extensive studies are performed including experimental demonstration [60, 61] and numerical analyses [62, 63].

When high-intensity laser pulse illuminates on a target, electrons gain energy and heat up first due to the smallness of their mass. Hot electrons generated by the laser target interaction can travel through the target and escape from the rear surface with a large angle. Although some of the electrons become free of the target, most of them are piled up at the rear surface due to the Coulomb potential. An electron cloud is formed. The density of these electrons n_e is distributed continuously in space and corresponds to a Boltzmann distribution, $n_e = n_{e0} exp(\frac{e\phi}{k_B T_e})$, where n_{e0} is the electron density in the unperturbed plasma, Φ is the electrostatic potential, and T_e is the electron temperature.

On the other hand, ions stay in the target without significant movement due to their exceedingly large mass. Because of the charge separation, a strong electric field sheath can be built up, and its scale length is on the order of Debye length of the hot electrons [64] as described by the following formulas.

$$E_{sheath} = \frac{k_B T_{ehot}}{el}\left(\frac{MV}{\mu m}\right) \tag{3.1}$$

$$l \sim \lambda_D = \sqrt{\frac{kT_{ehot}}{4\pi nehot e^2}} \tag{3.2}$$

At the very front of the expanding plasma, the Debye length of the hot electrons becomes greater than the scale length of a contaminant layer. The contaminant layer, composed of hydrocarbon, is generally formed from the air or pump-oil vapor on the rear surface. This electric field can generally reach TV/m, which is strong enough to ionize the atoms in the contaminant layer and accelerate the ions.

A large number of protons from the contaminant are accelerated normal to the target surface by the generated electric field due to their highest charge-to-mass ratio. This process of proton acceleration is displayed in Fig.3.6.

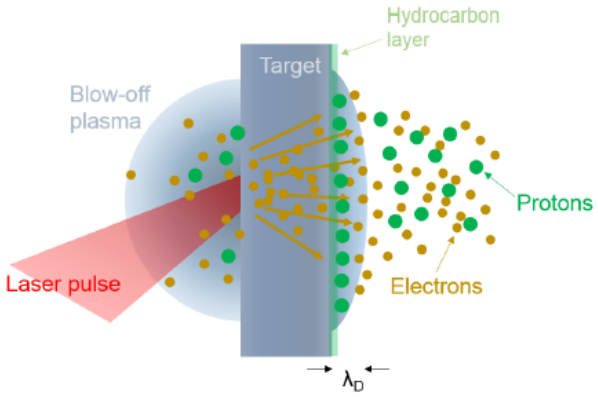

Figure 3.6: Cartoon showing target normal shealth acceleration mechanism. Hot electrons are generated by laser pulse interacting with a piece of thin target. They travel through the target and form an electron cloud at the rear surface. A strong electric field is generated on the scale of the Debye length of the hot electron near the rear surface of the target. The electric sheath field ionizes atoms in the hydrocarbon layer and protons are accelerated normal to the target surface.

3.3.1.2 Proton stopping

The stopping power on traveling charged particles by matter is inversely proportional to the square root of the particle velocities. When penetrating through a material, the deeper a charged particle goes, the smaller its velocity becomes; therefore the larger stopping force it experiences. In other words, the deceleration of a moving particle increases along with the depth it penetrates through. As a result, a traveling particle typically loses most of its kinetic energy right before it stops. If we plot the energy loss per unit distance against the penetration depth of a charged particle, a strong peak appears at the end of its trajectory, which is called the Bragg peak[65].

Because of the Bragg peak, when penetrating through a material, protons tend to deposit most of their energies into a narrow layer. The energy intensity (energy/unit volume) becomes great within the layer of the particle stops. This large energy intensity could change the chemical character and leads to the color change of some particular material. If we make this particular material into a thin film and place it along the proton

trajectory, it can image the distribution of protons of specific energy. With the utilization of multiple films, each film at different depth can collect protons of the corresponding energy. The entire film pack can provide proton radiography for the shock front at different proton energies.

Fig. 3.7 shows the energy lost per micron again the penetration depth of a proton into a typical film stack. The stack is made of 20 layers of HD-v2 films followed by 8 layers of MD-v2 films. A 100 μm thick aluminum filter is placed in front of the entire stack. Three representative initial energies, respectively $5MeV$, $10MeV$ and $20MeV$ are plotted. The three corresponding Bragg peaks are recognized at different locations.

The radiochromic film composes the particular material, as mentioned before. When energetic particles hit onto the material, if the energy intensity deposited by the particles becomes strong enough to ionize the atoms in the material, its color will change. The radiochromic film can be activated by ions, electron, X-rays, etc. Activation of different kinds of radiographic film requires a different amount of energy densities. The three most commonly used films are HD, MD, and EBT. The energy intensities they are sensitive to are listed as follows:

HD-v2	$10 \sim 1000Gy$
MD-v3	$10 \sim 100Gy$
EBT-3	$0.01 \sim 40Gy$

If the deposited energy intensity is smaller than the lower limit, the corresponding pixel can not be activated. Otherwise, the deposition of energy intensity greater than the upper limit results in the saturation of the corresponding pixel. The pixel then can not reflect the correct number of deposited particles.

Utilization of the radiochromic films is popular in the inertial confinement fusion experiment for its superior spatial resolution, which reaches $2.5\mu m$ [66], and its immediate response. It allows quick and dirty observation for the results right after a shot in the

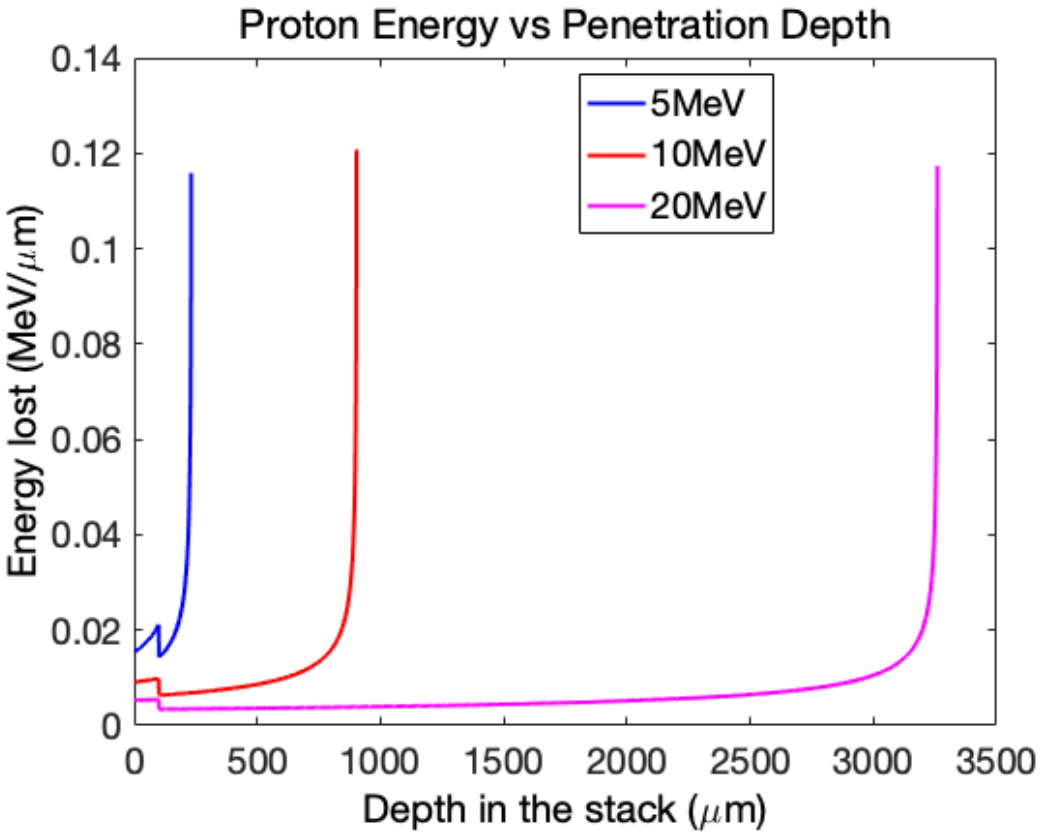

Figure 3.7: Energy loss curve over penetration depth of protons in a typical RCF stack composed of 20 HD followed by 8 layers of MD. a 100μ*m* aluminum foil was placed in front of the whole stack. Protons deposit most of their energy onto a highly localized region due to the Bragg peak. Therefore, each film in the stack displays the information carried by protons in a narrow energy range. Proton stopping power curves were simulated for protons with three representitative energies: 5 MeV, 10 MeV, 20 MeV.

high energy density plasma relevant experiment and doesn't require processing time.

Table 3.1: Composition data for GafCrhomic film used in this thesis. Table from [67]

Material	Thickness (μm)	Density (g/cm^3)	Composition(Atom %) H	C	O	N	Li	Cl	Na	S	Br	Al
HD-v2												
Active layer	8	1.2	58.4	27.9	11.7	0.1	0.6	0.6	0.5			0.3
polyester layer	97	1.35	36.4	45.5	18.2							
MD-v3												
active layer	15	1.08	56.8	29.1	47.12	6.94						
Polyester film	120	1.35	36.4	45.5	18.2							
EBT-3												
Active layer	30	1.2	58.33	29.61	10.79	0.06	0.82	0.19	0.11	0.03	0.06	
Polyester layer	125	1.35	36.4	45.5	18.2							

Typically, a single film is composed of an active layer sandwiched by the protecting plastic. Table. 3.1 provides the composition information of those films.

3.3.1.3 Radiographic films

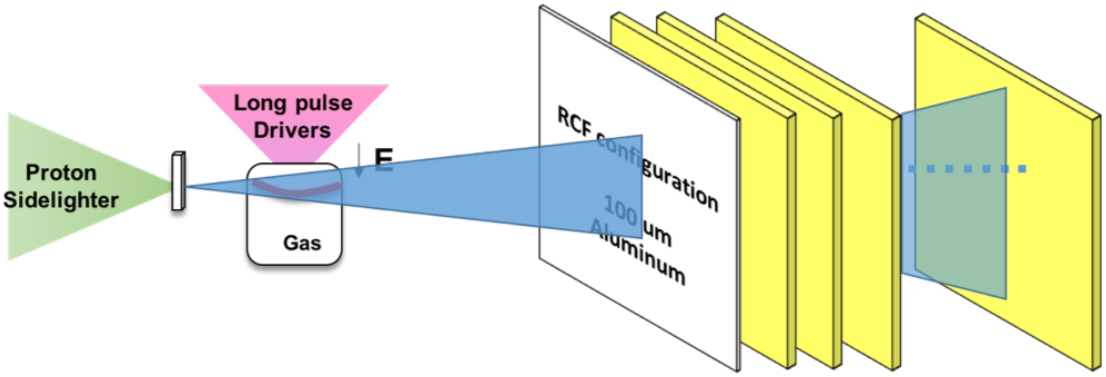

Figure 3.8: Schematic of the proton radiography system setup. A beam of protons is generated by a short pulse laser beam illuminating on a thin metal foil (40μm). They travel through the objective and deposit on a stack of radiographic films placed on the other side. The film pack is composed of multiple layers of radiography films. Each of them corresponds to protons of specific energy in a narrow range. The corresponded proton energy increases from the front layer to the back layer.

One of the detector pack used in the experiments in the current thesis is made of 28 pieces of film in total, configured as 20 layers of HD-v2 in front followed by another 8 layers of MD-v3 in the back. A 100μm aluminum foil is placed in front of the entire stack for protecting the films from debris and filtering the co-moving electrons with the proton beams.

The entire film stack covers proton energy from $3MeV$ to $22MeV$, details of the corresponding energy by each layer is displayed in Table. 3.2.

Table 3.2: Proton energy corresponding to each layer of RCF film in the stack. There are in total 28 layers in the film pack and a aluminum filter in front, covering proton energy spanning from $\sim 3MeV$ to $\sim 22MeV$.

Layer in the RCF stack	Film type	Corresponding proton energy(MeV)
	Al 100μm	
1	HD-v2	3.42
2	HD-v2	4.72
3	HD-v2	5.75
4	HD-v2	6.64
5	HD-v2	7.45
6	HD-v2	8.19
7	HD-v2	8.88
8	HD-v2	9.53
9	HD-v2	10.14
10	HD-v2	10.73
11	HD-v2	11.29
12	HD-v2	11.83
13	HD-v2	12.35
14	HD-v2	12.85
15	HD-v2	13.33
16	HD-v2	13.81
17	HD-v2	14.27
18	HD-v2	14.71
19	HD-v2	15.15
20	HD-v2	15.58
21	HD-v2	16.47
22	HD-v2	17.43
23	HD-v2	18.35
24	HD-v2	19.23
25	HD-v2	20.08
26	HD-v2	20.9
27	HD-v2	21.7
28	HD-v2	22.47

3.3.1.4 Calibration to dose

An Epson XL10000 scanner was used to scan the RCF films. Settings for the scanning are as follow:

Table 3.3: Epson XL10000 settings for RCF film scan

Mode	Professional mode
Document Type	film
Film Type	Color Negtive Film
Image Type	16-bit Grayscale
Resolution	800 dpi
Scale	100%

Conversion from the transmission to dose follows the calibration formula derived in [68], an overview for which is present in the following paragraphs.

The films were scanned into RGB files and calibration of the green channel of the HD-v2 film was performed. The films were cut to 2 2 cm2 and irradiated with 10 MeV photons with the following doses: 1, 2, 5, 10, 20, 50, 110, 250, 550 Gy.

To convert the raw numbers reading from the green channel of the film to doses, we first get the transmission using the raw intensity numbers:

$$Transmission = I/I_0 \tag{3.3}$$

where I is the raw pixel value reading from the green channel and I_0 is the maximum pixel value. Then the optical density can be calculated as:

$$OD = -log(T). \tag{3.4}$$

A plot of the optical density against the doses is shown in Fig.3.9. The curves can be fitted with the formula as:

$$OD(Dose) = 0.00832 + 0.000831x4.410^{-7}x^2. \tag{3.5}$$

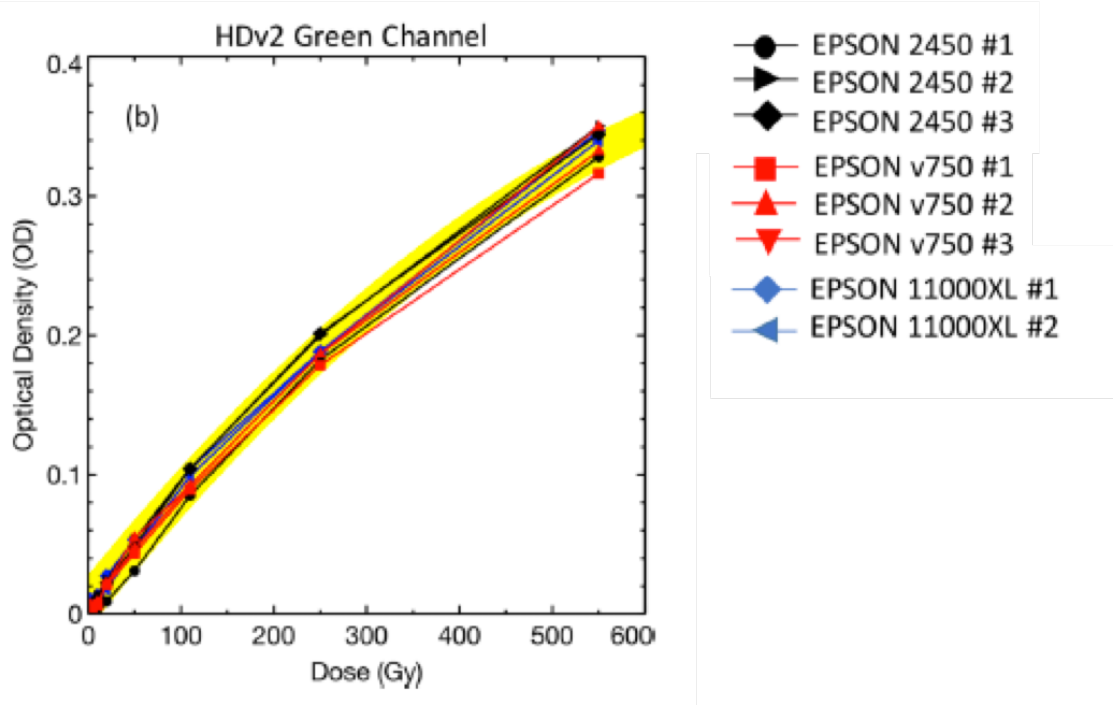

Figure 3.9: Optical density versus deposited dose of the GREEN channel of the irradiated HDv2 films with fitting the function of Equation 3.5. The film was scanned in RGB. Note that the width of the fitting functions is only for illustration purposes and does not reflect any quantitative values. Image courtesy of Chen.

3.3.2 Xray spectrometer

Another primary diagnostic in this experimental platform is a soft X-ray spectrometer. The spectrometer records the self-emission from the hot plasma at the shock front, thus providing the information of the temperature and density at the shock front. In general, two types of X-ray spectrometers are widely used: gratings and crystals. The gratings are used for a soft X-ray spectrometer that covers photons of energy up to 2 keV. In contrast, the crystals are used for hard X-ray spectrometer that covers photon energy from 2 keV to 10 keV. In our experiments, a variable-line spacing grating spectrometer was employed, which allows the spectrum to be recorded onto a flat film.

3.3.2.1 Variable-line spacing soft-Xray spectrometer

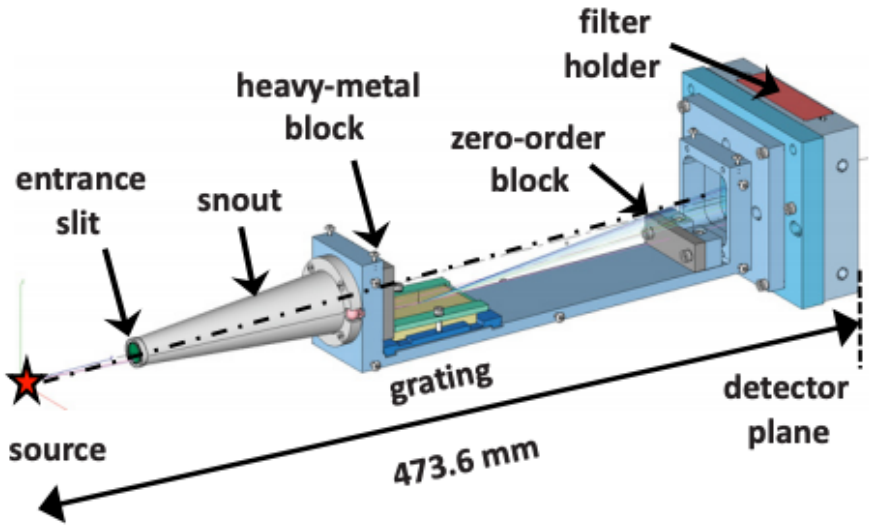

Figure 3.10: 3D model of the VSG soft x-ray grating spectrometer. Image courtesy of K. V. Cone.

The VSG was designed and built at the Lawrence Livermore National Lab [69, 70]. It has been regularly used at the Omega Laser facility[71] at the University of Rochester. Fig.3.10 shows the 3-D diagram of the VSG. A horizontal entrance slit 1 mm long and 20μm width positioned at the front tip of the snout provides a line of sight for x rays from the target onto the grating. A heavy-metal tungsten alloy block at the front of the aluminum body prevents straight-through x rays from directly illuminating the detector. A second block is positioned before the detector plane to block the zero-order diffracted x rays reflected off the grating from illuminating the detector. A filter composed of 1600$\mathring{A}$ aluminum-coated onto 5000$\mathring{A}$ of polypropylene positioned between the grating and detector reduces the background signal due to scattered optical light within the instrument.

The grating was designed with variable line spacing to focus the diffracted light onto a flat field [72] as shown by Fig.3.11. The utilization of the variable line spacing

grating makes it possible to use a flat detector without suffering a substantial loss of resolution across the covered spectral range. The VSG records spectra in the range of the 20 to 200 (6 to 60Å) by using a 2400 lines/mm diffraction grating.

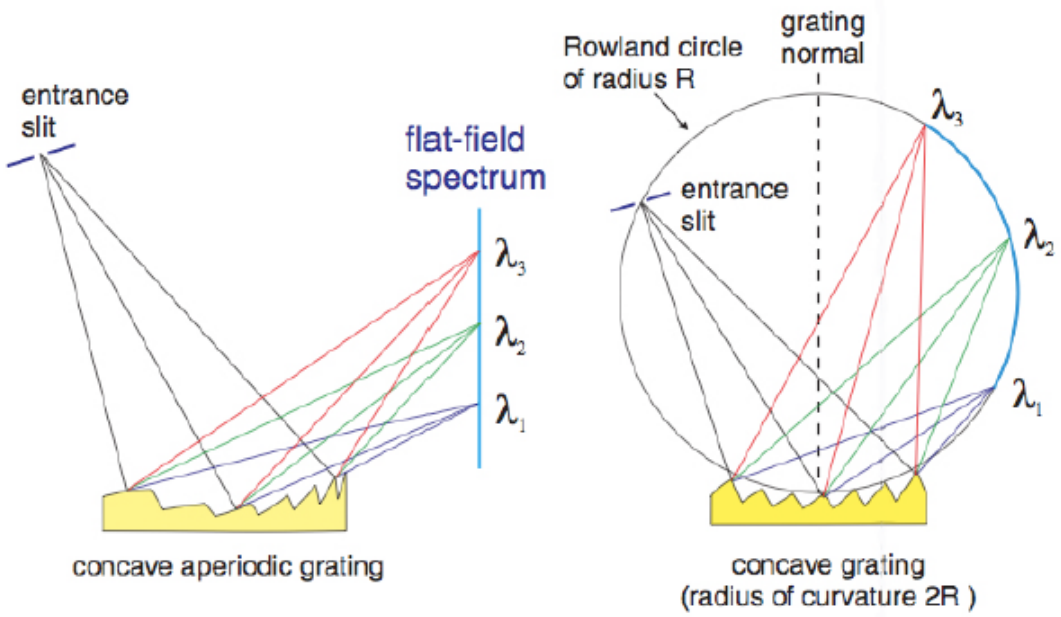

Figure 3.11: The use of a concave aperiodic grating allows the spectrum to be recorded on a flat plane, rather than on a curved surface. Image courtesy of M.-Y. Shen.

3.3.2.2 Calibration of the VSG

The calibration of the dispersion of the VSG is provided in Ref[70]. In this section, we give a brief review of the reference.

Line emission from the hydrogen and helium-like ions of carbon, nitrogen, oxygen, neon, and aluminum were used for the calibration. The result is shown in Fig. 3.12. The equation used to fit the curve is the standard grating equation given by:

$$m\lambda = d(sin\alpha - sin\beta) \tag{3.6}$$

where m is the diffraction order, d the line spacing in the center of the grating, α the normal incident angle 88.7°, and β the dispersion angle given by $[arctan(236/(y-y_0))-1.8°]$ where y is the spectral line position in millimeters and y_0 is the offset.

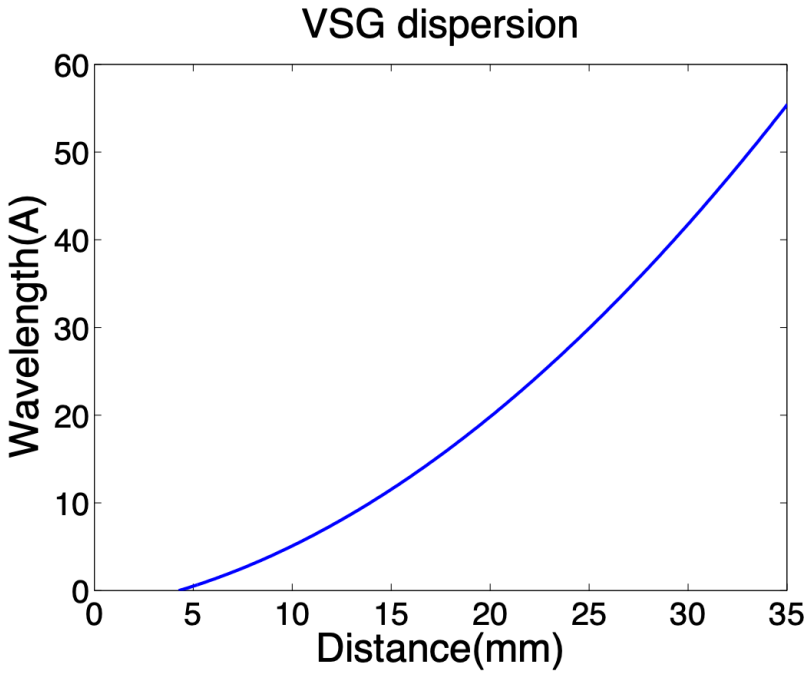

Figure 3.12: Wavelength of the emission lines versus their positions on the detector. Image courtesy of J.Park

3.4 Simulation tools

In the process of unraveling the self-generated field structure at the shock front, multiple simulation tools are used. The most important three are rad-hydro simulation code FLASH, hybrid particle in cell code LSP (large scale plasma) and a particle tracking code. FLASH is used to give an overview of the shock propagation and provide the associated plasma parameters, density, temperature and pressure for instances. LSP is used to simulate the field generation as the Biermann Battery mechanism has not been fully implemented in FLASH. The particle tracking code is used to simulate the

proton trajectory and their deposition on the detector given the structure of the electric and magnetic field, thus to constrain the field by forward fitting the observation from experimental data. Here we discuss FLASH simulation in more detail.

3.4.1 FLASH

The FLASH code is a parallel simulation code capable of handling radiation-hydrodynamic problem, for instance, the shock propagation studied in this thesis. A module of the laser-plasma interaction part, which calculates the laser absorption due to inverse bremsstrahlung is also included. Therefore, the full process from shock initiation by laser illuminating on a piece of ablator to the shock propagation into gases can be modeled by FLASH simulation. For a shock simulation, the primary modules in the input deck include radiation and opacity parameters, for which EOS tables for various materials are used, laser parameters, conduction parameters, hydro parameters, initial conditions, time and mesh parameters. An example of the laser parameters set up is shown in Fig. 3.13

```
############################
#                          #
#     LASER PARAMETERS     #
#                          #
############################
useEnergyDeposition = .true.
ed_maxRayCount      = 10000
ed_gradOrder        = 2

# Activate 3D-in-2D ray trace:
ed_laser3Din2D           = .true.
ed_laser3Din2DwedgeAngle = 0.1


### LASER IO OPTIONS ###
ed_useLaserIO                 = .true.
ed_laserIOMaxNumberOfPositions = 10000
ed_laserIOMaxNumberOfRays      = 128

### SETUP LASER PULSES ###
ed_numberOfPulses = 1

# Define Pulse 1:
ed_numberOfSections_1 = 4
ed_time_1_1  = 0.0
ed_time_1_2  = 0.1e-09
ed_time_1_3  = 4.9e-09 ### 2ns pulse
ed_time_1_4  = 5.0e-09

ed_power_1_1 = 0.0
ed_power_1_2 = 4e+10
ed_power_1_3 = 4e+10 ### 5ns 200J
ed_power_1_4 = 0.0

### SETUP LASER BEAM ###
ed_numberOfBeams = 1

# Setup Gaussian Beam:
ed_lensX_1                    =  0.0e-04
ed_lensY_1                    =  0.0e-04
ed_lensZ_1                    =  -1000000.0e-04
ed_lensSemiAxisMajor_1        =  100000.0e-04   ### look up on visrad
ed_targetX_1                  =  0.0e-04
ed_targetY_1                  =  0.0e-04
ed_targetZ_1                  =  0.0e-04
ed_targetSemiAxisMajor_1      =  400.0e-04
ed_targetSemiAxisMinor_1      =  400.0e-04
ed_pulseNumber_1              =  1
ed_wavelength_1               =  0.351
ed_crossSectionFunctionType_1 =  "gaussian2D"         #"uniform"       #"gaussian2D"
ed_gaussianExponent_1         =  4.0
ed_gaussianRadiusMajor_1      =  300.0e-04
ed_gaussianRadiusMinor_1      =  1300.0e-04
ed_numberOfRays_1             =  4096
ed_gridType_1                 = "radial2D"
ed_gridnRadialTics_1          =  64
ed_semiAxisMajorTorsionAngle_1=  0.0
ed_semiAxisMajorTorsionAxis_1 = "x"
```

Figure 3.13: example of the setup in laser parameter module in flash simulation.

Fig. 3.14 displays an example of the FLASH simulation results. It shows the 2D density and pressure maps of shocks propagating in silver targets and the snapshots were taken 5ns after the shock initiation. Initial density of the targets were $\sim 10.5 \mathrm{g/cm}^3$. The

shocks were created at position zero along Z axis by laser illumination onto 500μm thick silver targets. The laser delivered respectively 200J, shown as Fig. 3.14(a), and 2J, shown as Fig. 3.14(b), total energy during 5ns onto a 100 m spot.

From the snapshot showing the shock driven by the 200J laser on Fig. 3.14(a), the shock traveled for $\sim$ 130μm with a velocity of $\sim$ 26 km/s. The peak pressure and density at the shock front reach to 70 Mbar, and $\sim 60 \mathrm{g/cm}^3$, resulting in a compression $\sim$ 6x. In comparison, the shock driven by the 2J laser traveled for $\sim$ 45μm with a velocity of 9km/s. Despite its compression, $\sim$ 6x, being comparable to that by the 200J laser, the maximum pressure $\sim$ 6 Mbar is smaller than that by a factor of more than 10.

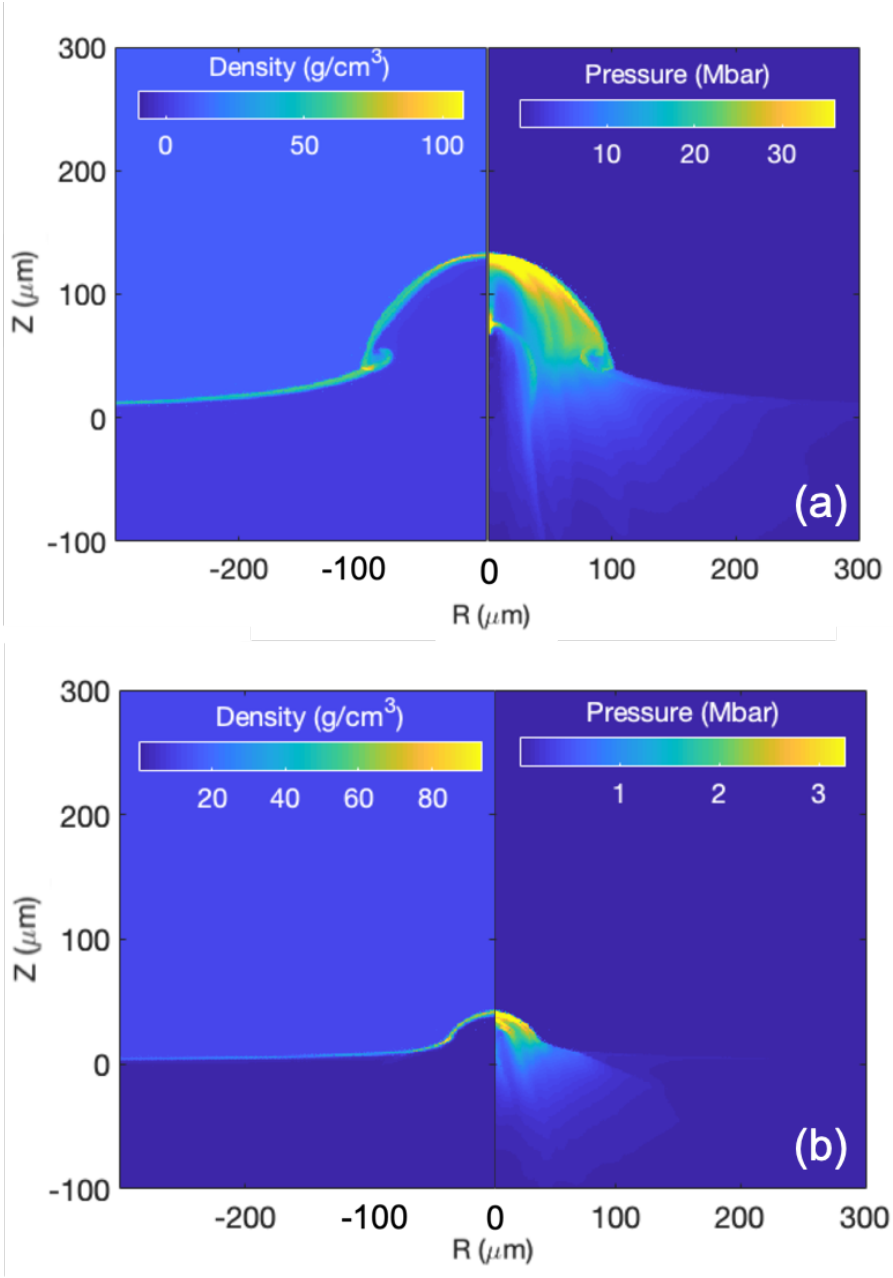

Figure 3.14: 2D density (left) and pressure (right) maps for shocks respectively driven by 200 J, 5 ns laser and a 2 J, 5ns laser. The spot size for the square shaped laser pulse was 100 m. The snapshots was taken at 5 ns after the shock initiation.

Another example of the shock created by the laser ablation of a piece of foil in helium gas is shown as Fig. 3.15. The 2D density and electron temperature maps are displayed.

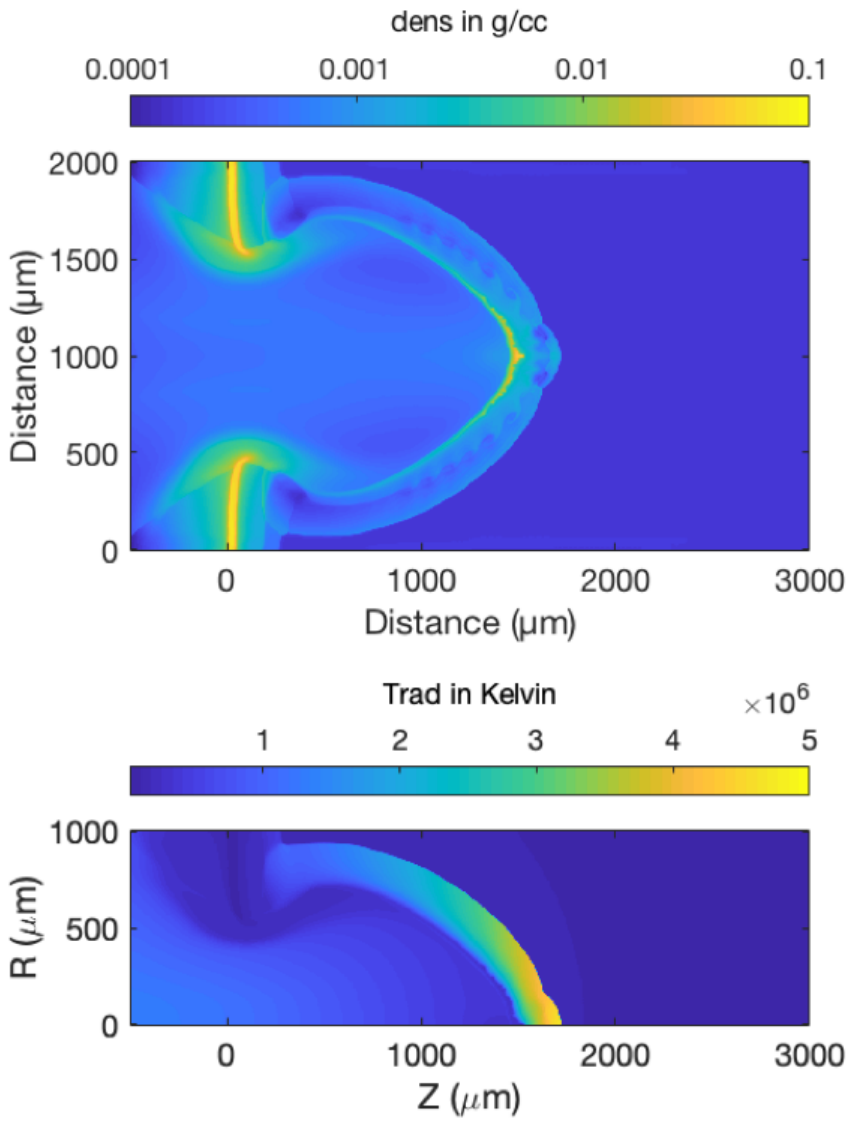

Figure 3.15: 2D density (top) and electron temperature (bottom) maps for shocks driven by 700 J, 0.5 ns laser. The laser comes from the left. The shock is propagating from left to right in helium gas and a 2µm glass has been placed on the left illuminated by the laser for the shock initiation. The spot size for the square-shaped laser pulse was $\sim$ 750µm. The snapshots were taken at 3 ns after the shock initiation.

Chapter 4

Electric field at the shock front

In this section, we describe results from experiments on the study of field generation at the shock front in low-density gas configured in quasi-planar geometry using broad-energy proton probing. Experiments were conducted using three long-pulse laser beams with a total energy of 6.4 kJ in 2 ns for shock generation and an 850 J, 10 ps short-pulse laser to produce broadband protons for radiography. Observations of the deflection pattern of probe protons show the existence of self-generated electric fields at the shock front with the electric potential on the order of 300 V. Analytical and particle tracking methods support this conclusion. The content presented in this section has been published in [27].

4.1 Introduction

Self-generation of electric fields at the plasma shock front is a kinetic effect that could affect the shock convergence phase[13, 34, 33]. Several candidate mechanisms explaining the formation of these fields were first proposed by Amendt et al[73], and

ion-kinetic simulation work was later performed by Bellei et al[31]. These fields, which are generated on the basis of charge separation[17, 18], are present at the fronts of strong plasma shocks, where large electron pressure gradients exist[5, 22]. Electrons, being more mobile than ions, are pushed slightly ahead of the shock, producing a negative charge surplus in the front of the shock. This creates an electric field pointing along the shock propagation direction.

Direct observations of the field were made by Rygg et al[26] and Li et al[23] in implosion experiments using monoenergetic proton radiography. However, limited by the spherical geometry, detection of the inward propagating shock fronts and the associated electric fields could not be distinguished from the ablator encompassing them by proton radiography. Besides, it is difficult to accurately constrain the field strength using the single energy datum provided by mono-energetic protons.

In this letter, we present results from a recently developed platform[58] using planar geometry and broadband proton radiography to investigate the shock front on the OMEGA-EP laser[74, 75]. Data from multiple proton energies are collected for each shot, which enabled the discrimination of the ablator and the shock front as well as the quantitative constraining of the field strength. An electric field on the order of a few microns wide and 300 V potential at the front of a 0.5 Mbar, Mach 10 shock is reported.

4.2 Shock Initiation and Proton Radiography images

A schematic diagram of the experimental setup is illustrated in Fig. 1(a). The main target was a cylindrical tube of 2 mm diameter and 5 mm length. The tube had 50 lm Kapton walls and two 1 lm thick Kapton windows along the line-of-sight of proton trajectories towards the radiochromic film (RCF) stack[76]. Pure helium gas filled the gas tube through the filling tube, which is at the right end of the gas tube in green and

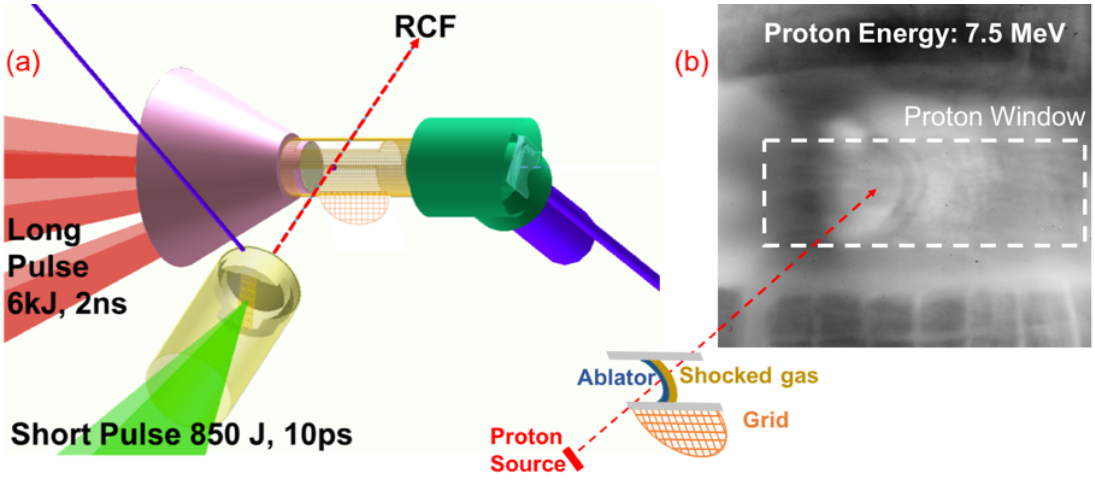

Figure 4.1: (a) Schematic of the experimental setup. (b) A typical proton radiograph taken with 7.5 MeV protons at 4 ns after the start of the long pulse. The gas-cell target was filled with 3 atm helium and driven by three lasers with 6.4 kJ over 2 ns.

purple. A strong shock was created in the gas by laser ablation of a polystyrene (CH) foil located on the left end of the gas tube. Three synchronized long-pulse laser beams were used to drive the shock by delivering total energy of 6.4 kJ in a 2 ns square pulse. A plastic cone was mounted around the CH foil on the left of the gas tube for plasma debris shielding. A semicircular copper grid with 55 lm wires and 340 lm period was attached to the bottom of the tube as a spatial reference.

The proton imaging scheme is composed of a back-lighter target and the RCF stack, respectively located at 7.5 mm and 12 cm on either side of the tube, corresponding to a magnification of 17 for the radiography. The proton backlighter consisted of a 40 lm copper foil strip protected by a plastic sleeve and a front foil. The front foil was 5 lm copper and separated from the copper foil strip by 1 mm to shield it from the target plasma. The Cu strip was illuminated by a short pulse laser with 850 J in 10 ps. A proton beam with energy spanning 20 MeV was generated from the target normal sheath acceleration mechanism[62].

The film stack had a 100 lm aluminum filter in the front, followed by 20 layers

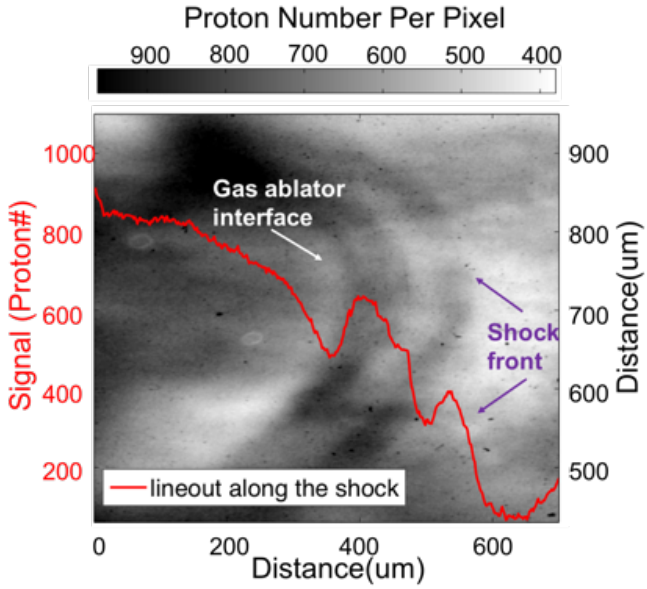

Figure 4.2: Shock front area captured by 7.5 MeV protons at 4 ns. A lineout across the center of the shock is plotted in red. The x-axis represents the distance from the initial ablator position. The spatial scale is adjusted to the objective plane by dividing the film measurements by the magnification of 17.

of GAFChromic HD-V2 films and then 8 layers of GAFChromic MD-V3 films[77, 78]. Each film is most sensitive to a specific energy band of 12 MeV. Thus, the entire stack can produce up to 28 radiograph frames using protons spanning 3 MeV to 22 MeV.

A typical radiograph taken by 7.5 MeV protons 4 ns after the start of the laser drive is shown in Fig4.1(b). The fill gas was pure helium at 3 atm (corresponding to an initial density of $0.5 \mathrm{mg/cm}^3$). Two dark rings are detected inside the window area, which are shown on a larger scale and with higher contrast in Fig4.2. In the figure, a 2D space map of the proton signal is plotted on the grayscale, and a lineout along the center of the shock is plotted in red. The spatial scale of Fig4.2 is adjusted to the objective plane by dividing the measurements on the film by the magnification of 17.

The origins of the two rings are identified to be the density scattering effect from the gas-ablator interface and field deflection at the shock front using the 2-D radiation hydrodynamic code FLASH[39]. Figure4.3(a) shows simulation results including pro-

files along the shock propagation direction for density (blue) and the electron pressure (green). Experimentally, the shock traveling distance at 4 ns is around 1.2 mm from the radiography measurement, which is in good agreement with the shock front position in the simulation as shown in Fig4.3(a). The two rings spacing is measured to be around 140μm accounting for the magnification of the radiograph, which is reasonably close to the separation between the shock front and the gas-ablator interface predicted by simulation (160μm) as in Fig4.3 (a). Therefore, we attribute the two rings to correspond to the shock front and the gas ablator interface. In addition to the data point at 4 ns, a data point from a nominally identical shot with proton probing at 3 ns is also included in comparison with the simulation as shown in Fig. 4.3(b). At 3 ns, only one ring is observed by the radiography, whose position is plotted in black. Likely, the shock front is not sufficiently separated from the ablator such that it cannot be resolved by the proton radiography at that time. The simulated distances of the ablator gas interface and the shock front are plotted vs time in solid blue and dashed green lines, respectively. The experimental data are displayed by circles with error-bars. The shock breakout from the ablator at an early time and its propagation away from the ablator at a later time are well depicted in Fig. 4.3(b). Overall, the FLASH simulation is in agreement with all three data points within the error bars, confirming our identification of the two rings.

We here discuss the calculation of the density scattering by the simulated ablator gas interface using Highlands formula[79]. In this calculation, the target density is $0.1 g/cm_3$ as in simulation and the target thickness is 1 mm (radius of the tube cross-section). Using the calculated scattering angle, a proton ring of 70μm wide is expected on the radiography film, which shows good agreement with the measurement of the inner rings width. This gives us additional confidence that the FLASH simulation is reasonable in reproducing our experimental conditions. Therefore, outputs such as pressure and temperature are used in the analyses described below.

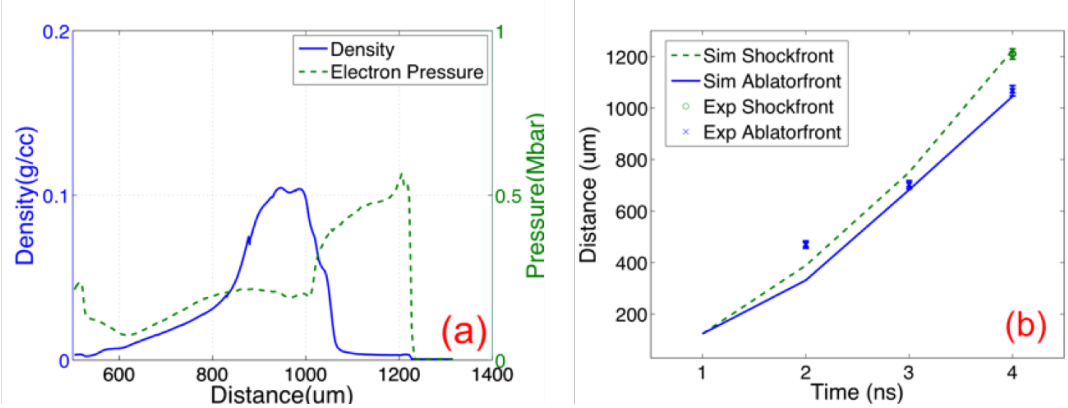

Figure 4.3: (a) FLASH simulation result for the shot shown in Fig. 4.2, which was filled with 3 atm and driven by a laser with 6.4 kJ in 2 ns. The x-axis represents the distance from the initial ablator position (zero point), where the shock was initiated. The snapshot was taken at 4 ns. The density profile across the shock center is plotted in solid blue, and the electron pressure is shown by a dashed green line. The pressure at the shock front is ~ 0.5 Mbar. (b) Simulated shock front (dashed green curve) and ablator-gas interface (blue curve) movement as a function of time. The circles with error-bars correspond to the data. Only one ring is observed at 3 ns, which could be the combination of both the interface and the shock front, and is plotted in black.

Not all layers in the RCF stack record deflection ring features that can be used for measurements, limited by the field potential as well as the image quality. The front-most layers collect signals from low energy protons. The deepest layers, collecting protons with up to 22 MeV, did not show a detectable ring with good contrast to the background presumably because these high energy particles were less susceptible to the fields. This phenomenon is also observed using a ray-tracing program for proton imaging that will be discussed later.

As there is a density gradient at the shock front, density scattering can also be a factor for the outer ring generation. To figure out this possibility, we estimate the scattering angle by the density gradient at the shock front using the Highland formula again. The densities on the leading and trailing sides of the shock front are 3.3mg/cm_3 and 0.5mg/cm_3 (compression is about 67 for a single shock with the radiation effect taken into account), respectively; the scattering effect is only able to make a ring up to 1

μm wide on the film for protons with energies between 5 and 8 MeV. Compared to the measurements of 50 μm, density scattering is negligible at the shock front.

4.3 Electric Field Calculation

4.3.1 Analytical method

Now, we will discuss the process used to extract the E field information, which is obtained by analyzing the outer ring observed in the radiographs. This ring is observed with the decreasing width for increasing proton energy because slower protons are more deflected by the field. The analytical solution of the proton deflection angle due to a radial electric field at a spherical surface was studied by Kugland et al[80]. The process is described as follows: the deflecting component of a proton traveling in the Z-direction through a field transversely can be described by the following equation

$$\frac{dV_x}{dt} = -\frac{e}{m}\frac{\partial \phi}{\partial x} \tag{4.1}$$

where x is along the field pointing direction, v_x is the deflecting component caused by the field, mp is the proton mass, e is the electric charge, and ϕ is the electric potential. Based on the relation that $d_z = v_z dt$, the deflection angle then can be expressed as

$$\alpha_x = \frac{v_x}{v_z} = -\frac{e}{2Ep}\frac{\partial}{\partial x}\int \phi(x,y,z)\, dz \tag{4.2}$$

Transforming the equation into spherical coordinates and assuming that the field profile is a delta function right at a spherical surface (a valid assumption when the field

width is significantly smaller than the radius) give the deflection angle

$$\alpha = -\frac{4er}{Ep}\int \frac{dr}{\sqrt{R^2 - r^2}}\frac{d\phi}{dr} = \frac{4e\phi}{E_p}\frac{R}{\sqrt{2R\Delta x}} \tag{4.3}$$

in which R is the spherical radius and δx is the proton displacement along the deflecting direction in the field. R is 935μm by the measurement and δx is assumed to be on the scale of the ion ion mean free path at the shock front, 0.4μm[5]. The ring width is determined by the spread between the protons experiencing no deflection ($\alpha = 0$ when a proton passed by the sphere) and those experiencing maximum deflection by the field. Therefore, the potential is calculated using the measured ring widths and their corresponding proton energies as shown in Fig4.4. The FWHM (full width half maximum) of the rings is measured from the lineouts from three layers in between 5 MeV and 8 MeV. One example of the lineouts is shown as the red curve in Fig4.2. Data points are plotted as blue circles, from which the electric potential is estimated to be $320 \sim 350$ V within the measurement errors. The black dashed line shows the expected behavior using the above equation when potential equals 330 V.

4.3.2 Numerical method

In addition to these calculations, a ray-tracing program to model the proton trajectories in the presence of electric fields is used to reproduce the images recorded by the film. In this process, a hemisphere shell-shaped electric field pointing outwards is implemented with a potential of 330 V. The field is uniformly distributed, and the radius of the sphere is 935μm. The proton source size is taken to be 10μm[81]. The output image has been adjusted such that the resolution is about the same as the data. Two simulated images by protons of 5.8 MeV (a) and 12.3 MeV (b) are displayed in Fig4.5. As expected, the results show strong energy dependence. In the simulated images, widths

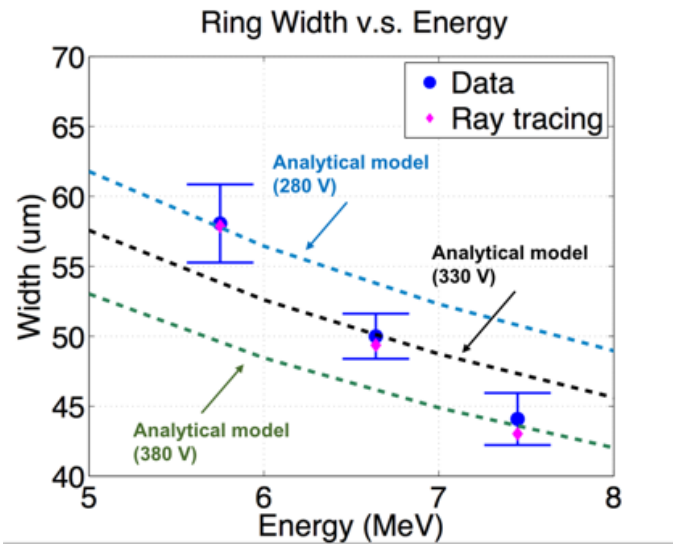

Figure 4.4: Ring width versus probing proton energies. The dark blue dots with error-bars are experimental data, and the pink dots are results from a ray tracing program. The three dashed curves are from Eq. 4.3, which show the result for potentials of 320 V, 330 V, and 345 V

are also measured at the same three proton energies as shown in Fig4.4 and are plotted in pink dots.

4.3.3 Discussion

Now, we discuss the reasons for these fields. A couple of candidate mechanisms have been proposed to explain the field existence since its observation. One such mechanism is attributed to the gradient in electron pressure, which can give rise to an electric field. In this case, free electrons can be pushed slightly ahead of ions due to their higher mobility, thus creating the electric field pointing along with the shock. The field strength can be expressed as $E = -\nabla P/en$, where n is the electron density, P is the electron pressure, and t is the electric charge. With the pressure profile shown in Fig4.3(a), the electric potential created at the shock front is 600 V.

The second approach compares the potential with the thermal energy[82]. In this mechanism, the electrons, being more mobile than ions, will diffuse ahead of the

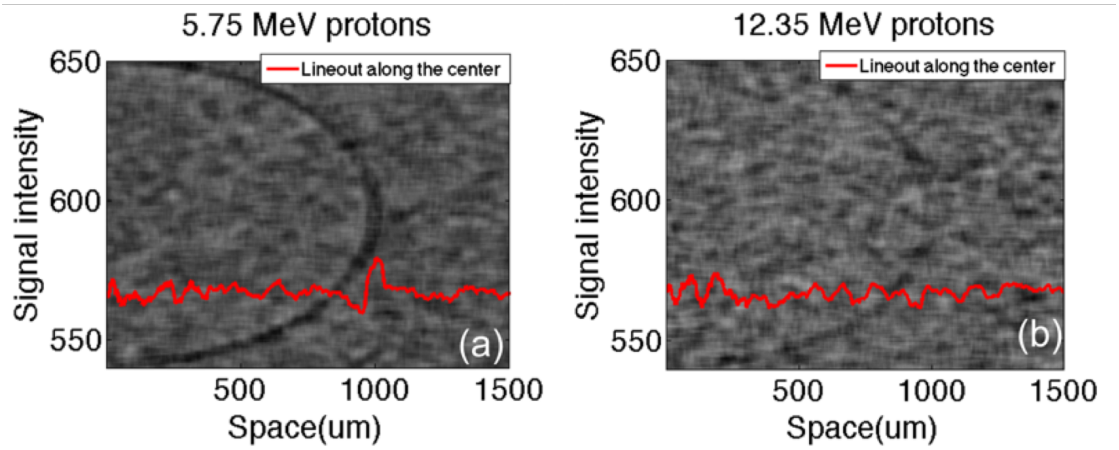

Figure 4.5: Proton images by the ray tracing program at two energies, 5.8 MeV (a) and 12.3 MeV (b). The electric field was set up to be 330 V, and the energy dependence is seen.

shocked ions due to the density gradient existing at a shock front, thus giving rise to an electric field. The potential formed in this process is mostly dependent on the electron temperature as expressed by $\Delta\phi \approx (k_B T_e/e)\ln(\rho_2/\rho_1)$, a simple expression that electrons can go no further than when they have lost all their thermal energy in overcoming the field potential. Here, ρ_1 and ρ_2 are the densities of shocked and un-shocked materials. As the electron temperature is around 300 eV and the compression is around 67, the field potential is about 600 V predicted by this model.

These theoretical considerations predict a higher electric potential compared to the experimental data. There are a couple of possibilities for this difference; first, the FLASH simulations were conducted in 2D, which might contribute to a sharper jump at the shock front when compared to the experiment. Further, in the analytical equation, the proton displacement in the field is considered to be 0.4μm according to the ion mean free path calculation, which might have underestimated the potential since in reality the displacement could be longer than the mean free path.

In summary, a strong self-generated electric field at a 0.5 Mbar shock front created in a low-density system has been both experimentally observed using broadband

proton radiography and theoretically predicted to be on the same scale. Additionally, 2-D radiation hydro simulations have been conducted, and the E field inferred from them also is favorably comparable with the experimental results. Possible reasons as to why the results are not an exact match are presented.

Chapter 4, in full, is a reprint of the material as it appears in Applied Physics Letter: R. Hua, H. Sio, S. C. Wilks, F. N. Beg, C. McGuffey, M. Bailly-Grandvaux, G. W. Collins, and Y. Ping "Study of self-generated fields in strongly-shocked, low-density systems using broadband proton radiography" *Applied Physics Letter*, 2017. The dissertation author is the primary investigator and author of this paper.

Chapter 5

Magnetic field at shock front

In this chapter, we discuss the observation of a magnetic field at the front of a Mach ~ 6 shock propagating in a low-density helium gas system. Proton radiography from different projection angles not only confirms the magnetic field's existence, but also provides a quantitative measurement of the field strength in the range ~ 5 to 7 Tesla. X-ray spectrometry allowed inference of the density and temperature at the shock front, constraining the plasma conditions under which the magnetic and electric fields are generated. Simulations with the particle-in-cell code LSP attribute the self-generation of the magnetic field to the Biermann Battery effect. The content presented in this section is under review.

5.1 Introduction

In recent decades, the electric fields associated with shock fronts have attracted great attention and are widely studied with proton radiography [23, 24, 25, 26, 27]. However, the extremely small scale of shocks and the finite resolving power of proton

probing highlights the difficulty of not only differentiating between electric and magnetic fields but also of providing a quantitative description of the field structure. As a result, the critical role played by the magnetic field has been underappreciated and only the electric field has been included in the experimental analysis, which has resulted in an aberration of up to a couple of orders of magnitude between experiments and simulation [23]. In addition, the numerical difficulties associated with magnetohydrodynamic simulation (MHD) of shocks imposes limitations on our ability to account for their effect on shock evolution [35]. Consequently, the magnetic fields associated with shocks remain unexplored both experimentally and theoretically.

While the existence of the magnetic field in laser-target interactions has been reported [83, 84], study of their evolution associated with shock propagation is rare in current literature. Recently, Rinderknect *et al.* [85] measured the spatial profiles of the ion temperature and density in strong plasma shocks; 3-D simulations predict strong magnetic fields ~ 10 to 10^2 Tesla are present during the stagnation phase in ICF [86], which could reduce the thermal loss from the hotspot [87, 88, 89]. Improved observations are necessary for comprehensively understanding plasma shocks, as well as benchmarking codes.

In this Letter, we report the direct observation and quantitative description of a (Mach ~ 6) shock-associated magnetic field by varying the projection angle of probing protons. The experiments were conducted on the Omega-EP facility. The measurement of the self-generated electric field has been reported in 2017 using the same platform but with normal incident protons to the apex of the shock front [27]. The explanation that a magnetic field was diagnosed in the current article using oblique incident protons whereas an electric field was probed in the previous chapter by normal incident protons is discussed in detail in Section 5.1.1

5.1.1 Normal and oblique proton incidences for electric and magnetic field

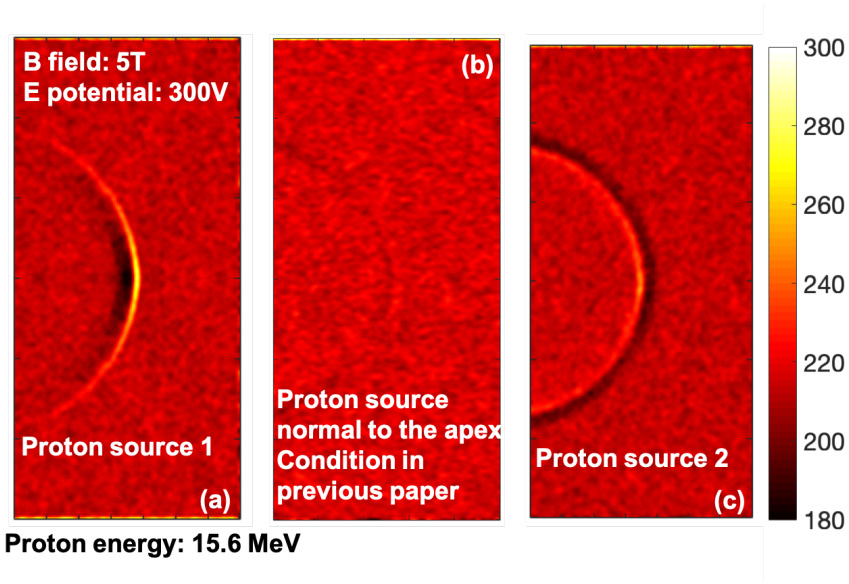

Figure 5.1: Simulated RCF images for protons from behind the apex in (a), normal to the apex in (b) and beyond the apex in (c). (a) and (c) respectively correspond to the proton source '1' and '2' in this article while (b) displays the result corresponding to the proton source position used in previous chapter.

A seeming contradiction arises from an article in 2017 that reported the measurement of the electric field using a similar experimental configuration [27]. A detailed discussion regarding this problem is provided in this section.

The reason that the field type probed in the previous chapter was identified as an electric field, whereas it is predominantly a magnetic field in the current article, arises from the different proton probing angles, which is the result of an improvement in our technique. In the previous article, the proton source position was perpendicular to the apex, while in the current study we intentionally explored oblique angles.

The magnetic force exerted on protons strongly depends on the proton incident angle while the electric force does not. As the radiographic data in Fig. 5.1 show, in the presence of a sufficiently strong magnetic field, a bright or dark ring respectively

forms on the detector plane when probing the shock front from behind or beyond the apex (Fig. 5.1 (a) and (c)). In contrast, when the protons probe the apex perpendicularly, the effect of the magnetic field will cancel and only the electric field effect will appear. Therefore, the magnetic component at the shock front did not reveal itself in the previous chapter using normal proton incidence. The lack of signal fluctuation in Fig. 5.1(b) is consistent with the previous article, where only less energetic protons can detect the electric field due to its weak intensity.

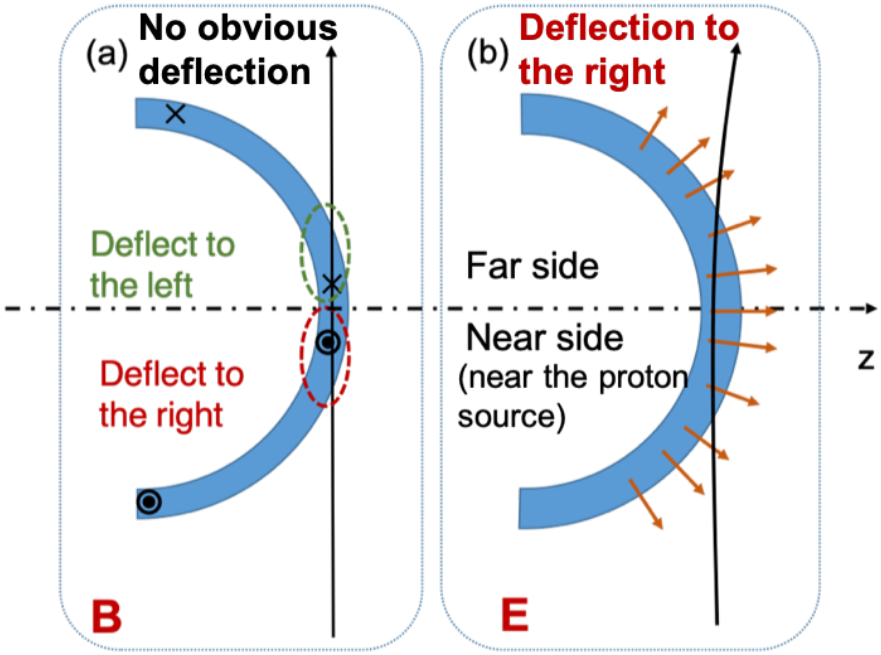

Figure 5.2: Normal proton incidence to the apex and their interaction with the magnetic field in (a) and electric field as shown in (b). The normal incident protons end up with no net deflections by the magnetic field due to their nearly symmetric movements at the near and far sides of the shell, therefore only deflections by electric field can be disclosed.

Fig. 5.2 sketches how magnetic field (a) and electric field (b) deflect protons in the case of normal incidence. Under the cross-sectional view, the azimuthal magnetic field points into the screen on the far side of the shell and out of the screen on the near side as shown in Fig. 5.2(a), and the electric field points radially outward as shown in

Fig. 5.2(b).

The perpendicular proton trajectories are nearly symmetric with respect to the z-axis (the center axis of the shell), on different sides of which the magnetic forces are opposite. Therefore, the magnetic effect eventually cancels as shown by Fig. 5.2(a), and the net proton deflection only arises from the electric field as shown in Fig. 5.2(b).

The case of oblique proton incidence is illuminated by Fig.3 in the main manuscript and a paragraph of the corresponding explanation is presented.

5.2 Shock Creation and Proton Radiography Data

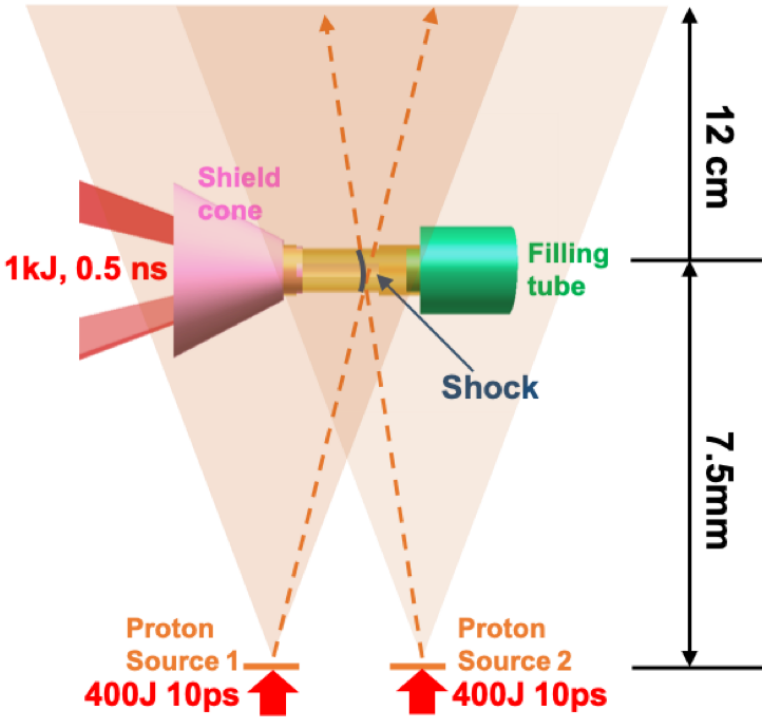

Figure 5.3: (a) Schematic diagram of the experimental setup. Proton source '1' is located $\sim$ 800 μm behind the shock longitudinally and 1 mm away from Proton source '2' that is $\sim$ 200 μm in front.

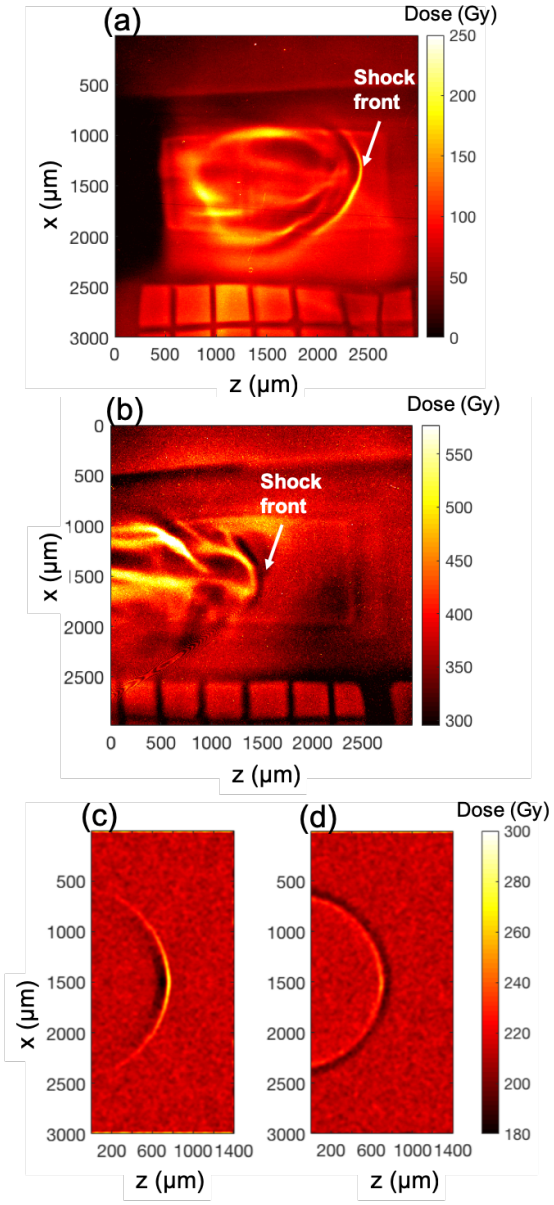

Figure 5.4: RCF image from 'proton source 1' by (a) and 'proton source 2' location by (b). Shocks were initiated at location '0' along the z-axis by the ablation of a SiO_2 foil, which was placed 200μm inward relative to the left window edge. The images were captured 3ns after the shock initiation by 15.6 MeV protons. Values in the color-bar represent the dose in Gy unit (J/kg). The two shocks are of identical conditions, only the proton source location varied. (c), (d) Simulated images from 'proton source 1' and '2' produced by a 3-D particle tracking code. The white dashed lines indicate the corresponding window boundaries' position.

The main target is a cylindrical tube 2 mm wide and 5 mm long, filled with pure helium gas at 1 atm. The tube is made of 50 μm polystyrene (CH) with three 1 μm-thick windows along the axis, two of which reduce the stopping of probing protons while the other minimizes the absorption of emitted light collected by a soft X-ray spectrometer.

A strong shock was created when two synchronized long-pulse laser beams delivered 1 kJ total energy in 0.5 ns square pulses to ablate a 2 μm SiO_2 foil located on one end of the tube [58]. The shock velocity is ~ 600 km/s. The calculation of Mach number as the ratio of shock velocity to the sound speed of the rest medium took into account the preheat ahead of the shock front, as observed from the VGS spectra shown in Section 5.4.

The probing protons, spanning 20 MeV [62] in energy, were produced by a short pulse laser (400 J, 10 ps) interacting with a 40 μm copper strip. This proton side-lighter target was positioned 7.5 mm laterally from the tube axis and the RCF stack was opposite it 12 cm from the tube axis, corresponding to a magnification of $17\times$. Two proton sources were located 1 mm apart as labeled in Fig. 5.3: 'proton source 1' was located 800 μm behind the shock front along the tube axis and 'proton source 2' was located 200 μm ahead. Protons from the two sources probed the shock at two different lines of sight, thereby confirming the structure and magnetic nature of the field by geometrical considerations. A semicircular copper grid with 55 μm bar and 340 μm gap size was attached to the bottom of the tube as a spatial reference.

Fig. 5.4(a) and (b) show the RCF images of two identical shocks probed from proton source '1' and '2', where the color scale represents dose per pixel in Gy unit (J/kg). Each shock was generated in 1 atm pure helium gas by two 0.5 kJ, 0.5 ns laser pulses. The white arrow on each image identifies the shock front positions 3 ns after the shock creation. We analyzed each shot through the entire RCF stack, observing an energy-dependent change of the ring structure over 7 MeV to 16 MeV. However, because

the resolving power is better at higher proton energy, we focus our analysis on the image produced by 15.6 MeV protons, due to their superior contrast. Analysis of radiography data from lower energy protons provided similar results but of lower precision, examples of which are provided in the Section 5.6.

The contrary proton flux pattern in Fig. 5.4(a), a higher flux (bright ring) ahead, and (b), a lower flux (dark ring) ahead, allows us to conclude that the field at the shock front deflects protons in a manner dependent on their incident angles. This signature confirms the domination of the magnetic field over the electric field, since electric fields deflect charged particles independently of their incident angles. Fig. 5.7 displays the detailed process of how a magnetic field at the shock front deflects protons, in which three scenarios are discussed under the cross-sectional view. Given the azimuthal symmetry of the system, the field points out of the paper at the bottom part of the shell (nearer the proton source) and oppositely into the paper at the top part. Interaction between protons and the field within the shell can be categorized into two scenarios: one is shown as Fig. 5.7(a), where the proton trajectories intersect with the shell twice at both the near and far parts; the other is shown as Fig. 5.7(b) and (c), where the protons interact only the near or far side of the shell respectively. For the former case, regardless of the source location, deflections by the two intersections cancel each other, thus unbending the final proton trajectories. For the latter cases, where a proton grazes only the near or far part of the shell, as shown by Fig. 5.7 (b) and (c), the signal from source '1' and '2' will be deflected in opposite directions. Consequently, protons from 'source 1' are deflected to the right given the out-of-paper B pointing and produce the bright leading ring as observed in Fig. 5.4(a); while protons from source position '2' are deflected to the left and result in the dark leading ring as shown by Fig. 5.4(b). When it comes to the electric field, protons are deflected to the right regardless of their incident angles due to the radially outward directionality of the field [27].

Although both field types must exist simultaneously at the shock front, we will show later that the magnetic field dominates and the contribution from electric field is ignorable in the following, where we quantitatively unravel the structure. Before doing so, it is important to address the effect of density scattering that could also cause proton deflection due to the sharp density gradient at the shock front. A detailed discussion of this process is included in Section 5.2.1, which shows that the density effect is negligible under our condition.

5.2.1 Density scattering contribution in the radiography data

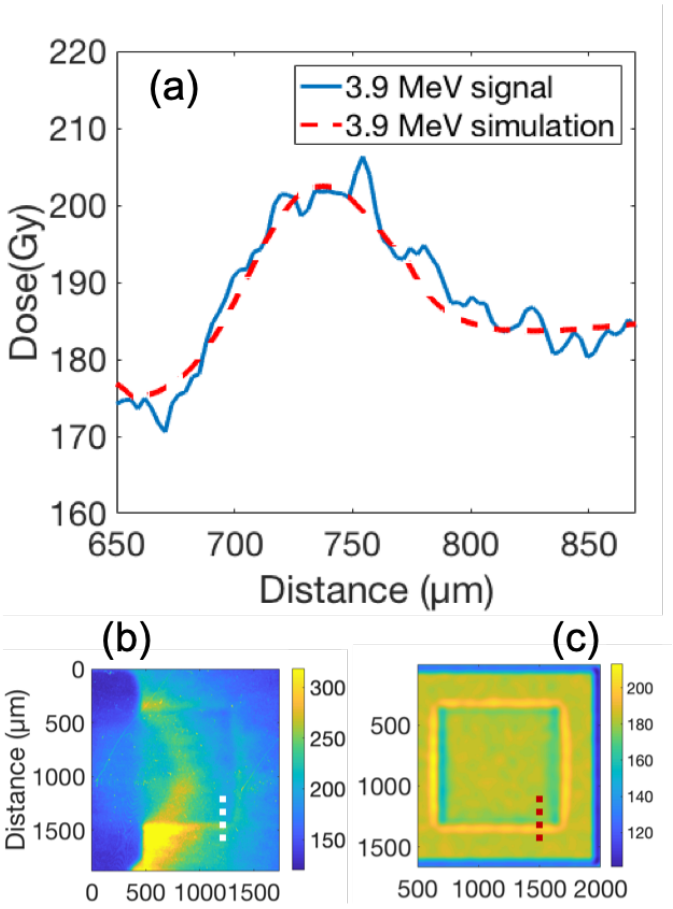

Figure 5.5: (b) and (c) are the experimental and simulated RCF images for the SiO_2 foam target. (a) lineouts from proton radiography of the foam target: solid blue and dashed red are respectively experimental and simulated proton signals from the edge of the SiO_2 foam target.

Here we show that the observed features in the proton radiographs cannot be explained by scattering in the vicinity of sharp density gradients. Two sites where such gradients exist are at the shock front and at the material interface between the ablator and gas.

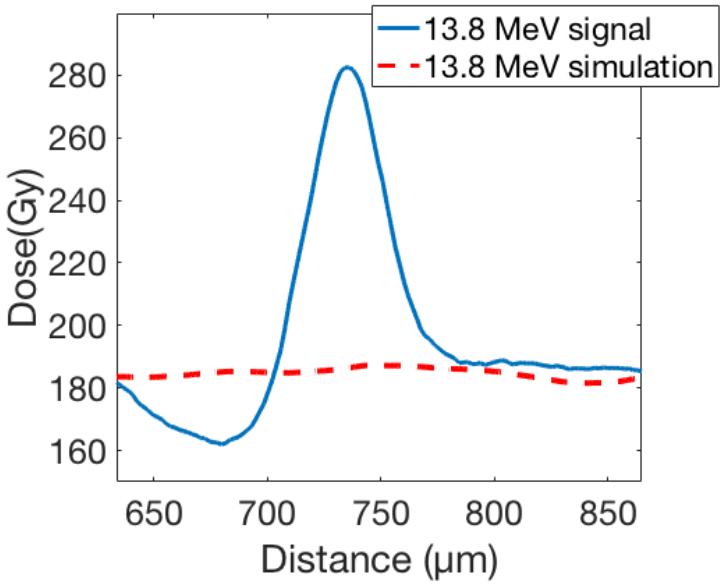

Figure 5.6: Lineouts from proton radiography of the shock: solid blue is the measured signal across the shock front. Dashed brown is the simulated proton signal by density scattering.

We employed a 3D particle tracking program to do the estimation, in which Highland formulation [79] was used to calculate the proton trajectories as they experienced scattering on a density gradient. To benchmark this method, the predicted scattering was compared to experimental radiographs of an unshocked density gradient - the limb of a cylindrical SiO2 foam target of $50\text{mg}/\text{cm}^3$. The comparison process is displayed in Fig.5.5: (b) and (c) respectively show the experimental and simulated RCF images of the foam target by 3.9MeV protons. The reason for choosing data at 3.9MeV is that during this shot, the short pulse for proton generation was only 50J instead of 400J, thus the proton energy only reached to $\sim$ 5MeV. In the experiment, a shock was launched into the foam and reached to about half the tube when proton arrived. The unshocked part is used for comparison. We compared the lineouts across the edge of the cylinder shadow between experimental data, in solid blue, and simulation result, in dashed red, as plotted in Fig. 5.5. The good agreement confirms the accuracy of the method.

Based on this fair agreement, we simulated the density scattering effect for the shock scenario. The density profile across the ablator and shock is calculated by a radiative hydrodynamic code FLASH [90]. The reliability of the simulation has been discussed in [27]. Density drops from $20\text{mg}/\text{cm}^3$ in the ablator region to $1.3\text{mg}/\text{cm}^3$ in the shocked gas and then to $0.17\text{mg}/\text{cm}^3$ in the un-shocked region. This configuration was simulated with the tracking code to observe the effect of scattering, and the simulated dose profile is plotted as the dashed red curve in Fig.5.6. The variation is imperceptible compared to the observed proton signal across the shock front as plotted in the solid blue curve.

The Highland formula can provide additional confirmation through consideration of its scalings: the scattering angle is inversely proportional to the proton energy and directly to the square root of density. By comparing the condition of the shock with the SiO_2 target, we can make the following estimation. The scattering effect on 13.8MeV protons by the $20\text{mg}/\text{cm}^3$ ablator would be $\sim 5.6\times$ weaker than that to 3.9MeV protons from the $50\text{mg}/\text{cm}^3$ foam edge. Therefore, as the scattering signal (solid blue on Fig.5.5(c)) from the edge is $\sim 20\%$ of the measured signal (solid blue on Fig.5.6) form the shock front (by comparing the bumped area), the density scattering from the shock front would only be $\sim 3.5\%$ of the measured signal, which can be neglected.

5.3 Data Analysis by 3D particle tracing Program

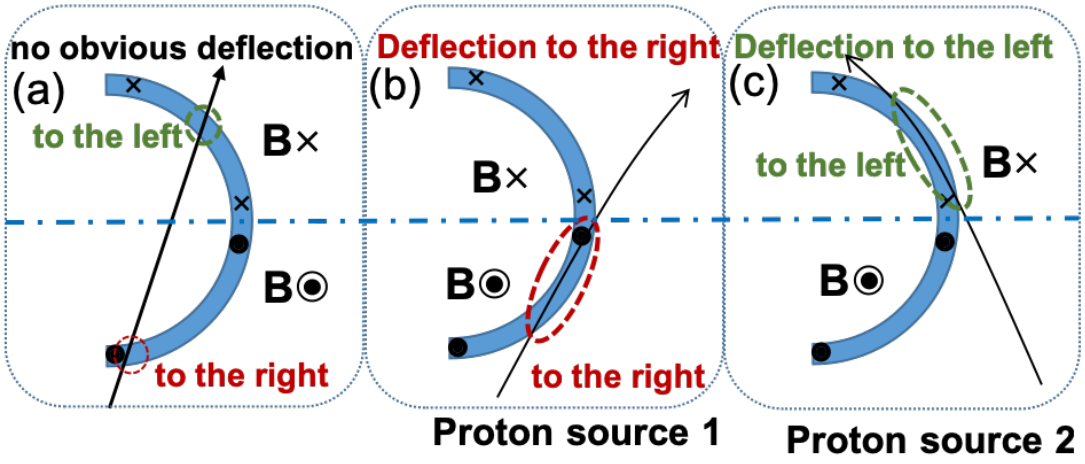

Figure 5.7: Cross sectional top view of the hemispherical shell model of the shock front B field. (a) shows the case where a proton intersects the shell twice, resulting in deflections right then left located at the red and green dashed circles respectively. Because the deflections are opposing, no obvious variation can be observed on the film. (b) and (c) show the cases where a proton intersects only the near or far side of the shell, respectively. The figure conveys the idea of right deflection and left deflection qualitatively and the incident angles of the proton trajectories are not drawn to scale.

We employed a 3D particle tracking program to simulate the proton probing scheme and study the field structure by quantitatively matching the experimental data with simulation results. The geometric diagram in the simulation replicates the proton probing setup. At the shock region, an azimuthal magnetic field is implemented given the cylindrical symmetry of the shock. The 3D field has non-zero magnitude only within a hemispherical shell of 1mm radius and its direction points clockwise as viewed from the apex. The Leapfrog method [91] was used to compute the proton trajectories as they experience the Lorentz force in the prescribed fields. By adjusting the field parameters: magnetic strength, shell thickness, and its spatial distribution along both x and z axes, we are able to quantitatively forward fit the experimental data.

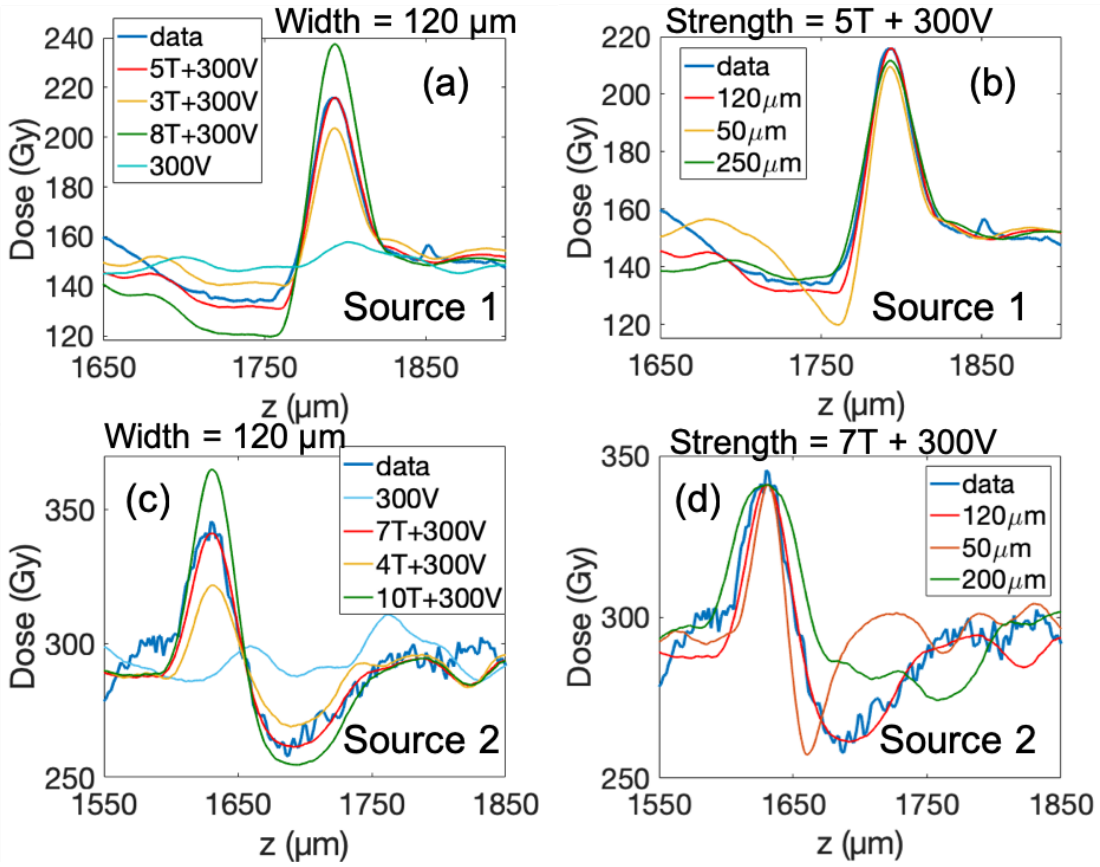

Figure 5.8: Lineouts from the center axis of the proton rings both from experimental and simulated data. The first row of the plots show fittings for 'proton source 1' image and second row for 'proton source 2'. On each plot, the dark blue curve represents the data and the red curve is best fitting. The two additional curves show the misfit when a certain parameter deviates from its best-fit value: (a) and (c) show the deviation of magnetic strength. The spatial profile is fixed triangular and the field thickness is 120μm; (b) and (d) show the deviation of the shell thickness. The spatial profile is fixed as triangular and the peak magnetic strengths are at 5T and 7T respectively; The light blue curve on (a) and (c) plot the results from the pure electric field of 300 V potential, which is negligible compared to the measurement.

To include the possibility of both magnetic and electric fields' influence, an electric field corresponding to a 300V potential and given varied width is included. The electric field was obtained from another diagnostic, a 1-D resolved soft X-ray spectrometer, known as a VSG (Variable line Spaced Grating spectrometer) [70], which measured the shock temperature and density to be $\sim$ 140eV and $\sim$ 1.5mg/cm^3. A

detailed discussion of the measurement process is provided in the Supplementary Material Section III.

According to the expression $\Delta\Phi \approx ln(\rho_2/\rho_1)k_BT_e/e$, the electric field potential is $\sim$ 300 V based on the shock front condition. In contrast to previous work [23] which only considered the effect of the electric field on the proton trajectories, we find the electric field's contribution is always negligible in comparison to the experimental data when varying the simulated width from a few to hundreds of μm. The 30μm case is shown in Fig. 5.8. It is clear that the magnetic field dominates the deflection.

Fig. 5.4(c) and (d) show the simulated results by 15.6 MeV protons from source '1' and '2' respectively. From these images, which qualitatively reproduced proton flux pattern from each proton source, we scanned through the field thickness from zero to millimeter scale, magnetic strength from zero to hundreds of Tesla and varied the field spatial profile along the z-axis from a uniform distribution (square) to triangular distribution until the best match was found. The spatial profile along the shell is assumed to be uniform in the calculation. Fig. 5.8 here shows the fitting processes for magnetic strength and the field thickness. Spatial profiles of the fields are also analyzed, details of which are provided in Section 5.3.2. Before comparison, the raw simulated images were convoluted with the experimental spatial resolution $\sim$ 25 μm.

In order to make the best quantitative comparison, we compared experimental and simulated transverse dose lineouts taken from the center axes (position at x = 0) of the rings as indicated by the horizontal white dashed line in Fig. 5.4(b). Our best fit to the data indicates the magnetic field is well represented by the combination of an electric field of 300 V potential and a magnetic field of triangular-shaped spatial profile that spans over 120 μm within the shell with a peak intensity of 5 T and 7 T, respectively for the proton source '1' and '2'. In Fig. 5.8 : plots (a), (b) show the fits corresponding to proton source '1' and plots (c), (d) show those from '2'. On each plot, the dark blue curve

represents the experimental data and the red curve displays the best fit. Two additional curves describe the sensitivity by showing the deviation in overall fit when a certain parameter deviates from its best-fitting value. For example, in the plot (a) we fixed the field spatial distribution and thickness at 120μm then varied the peak magnetic intensity. The simulation curves noticeably differ from the experimental curves when the field strength deviates from 5 T to either 3 T or 8 T. Similarly, plots (b) displays the fitting sensitivity of the shell thickness.

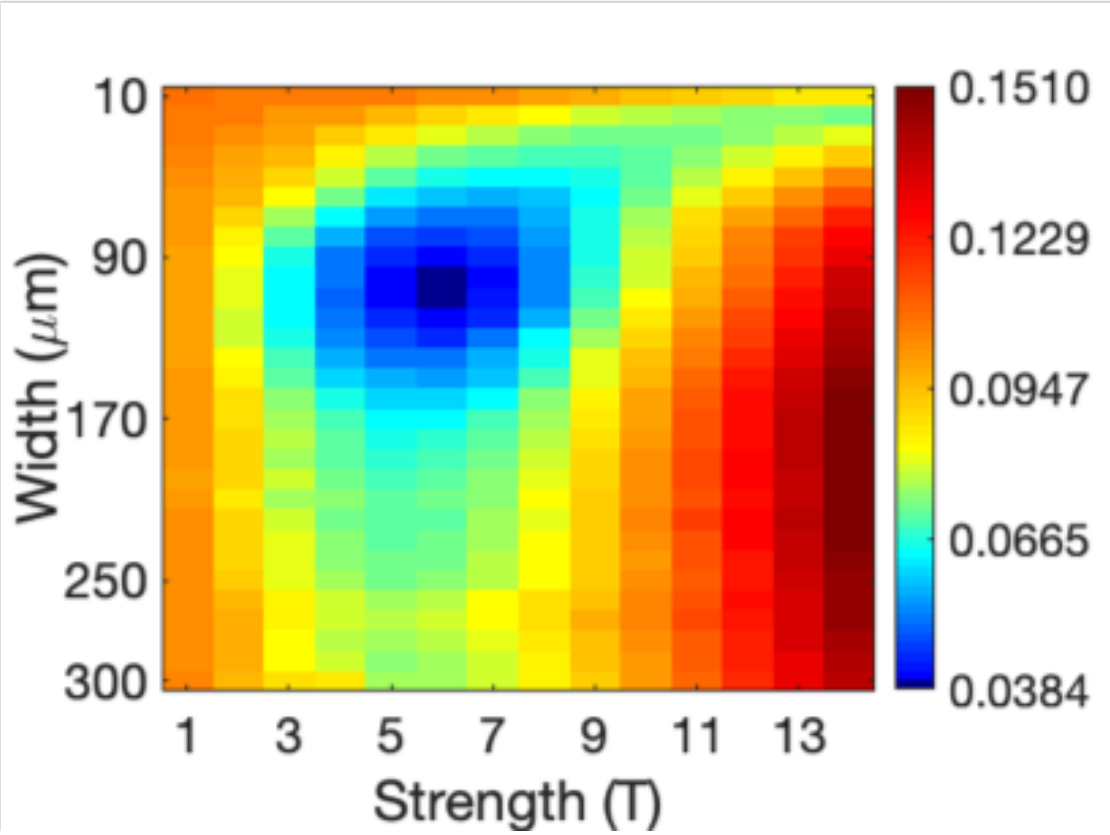

Figure 5.9: The fitting error map. Blue color indicates smaller error, better fitting and red color indicates larger error, worse fitting.

To confirm the magnetic field extracted by forward fitting the experimental data, a thorough scan for the field amplitude from 1 T to 14 T and width from 10 μm to 300 μm was performed and the result is displayed by Fig. 5.9.

The fitting error from 1600 μm to 1850 μm along z axis is calculated as $\sqrt{\frac{1}{n}\Sigma\frac{(D_i-S_i)^2}{D_i^2}}$, where D_i represents the data, S_i is from the simulated image and n is the number of the sampled points. The region at $z < 1600$ μm is the ablator area behind the shock which displays complex 3D structure and is not included in our simple model of the magnetic field at the shock front. Fig. 5.9 shows the average of four error maps including the two radiographs of 15.6 MeV protons for both sources discussed in the section and the other two of lower proton energies, 11.2 MeV from source 1 and 9.5 MeV from source 2. The amplitude and width of the magnetic field determined by the four radiographs converge to 6 ± 1T, 110 ± 20μm to fit the data within 5%. Each of the individual fitting error maps and more discussion on the error analysis is provided in Section5.3.3.

5.3.1 Analytical and numerical calculation for the proton deflection

In this section, we present precise calculation for the proton deflection by the magnetic field both analytically and numerically. Protons injected into the shock front from 'proton source location 2' is used in the derivation. The incidence angle is 1.53° according to the geometry. The detailed calculation shows that, though small, this angle still produces a recognizable change to the shape of the signal on the radiochromic film (RCF) by the adopted proton imaging system. First, we provide a simplified illustration for the proton deflection by the analytical method.

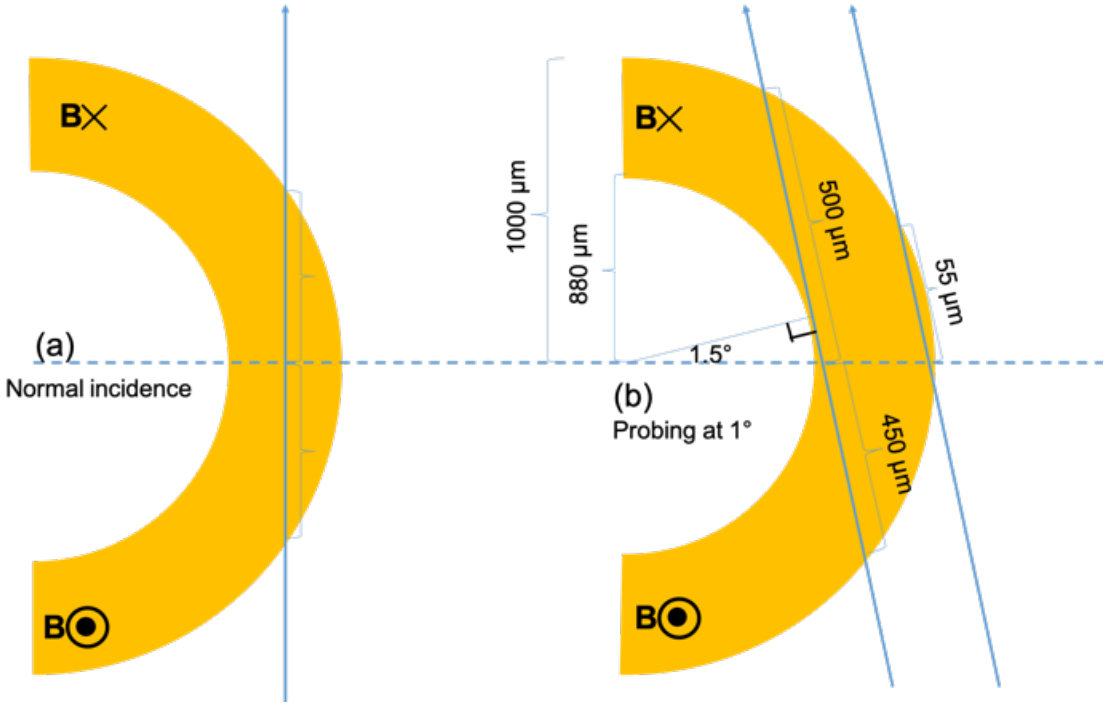

Figure 5.10: (a) Scheme of normal proton probing (b) scheme of oblique proton probing at 1.53°

Fig. 5.10 shows the scheme of normal incidence proton probing (a) and oblique proton probing at 1.53° (b). In order to make the small deflection process clear, the figure is not drawn to scale, although the reported lengths are correct. For simplicity, we assume the protons intercepting the semi-spherical shell representing the shock front are parallel with each other based on the fact that the distance to the proton target 7.5 mm is much larger than the thickness of the shell 120m. In addition, we assume small deflection for all protons due to their exceedingly large kinetic energies 15MeV.

For the normal incident case, the distances traveled in the near side (bottom side of the shell) and the far side (top side of the shell) are always approximately equal. Therefore no obvious deflection would be observed for the illustrated ray nor for rays further back. For the oblique incident case, the reviewer is right that most of the protons traveled through both sides of the shell, and only a small amount of them purely interacted

with the far side (top side of the shell drawing). However, the distance a proton traveled on each side is different due to the oblique incident angle. By precisely measuring the proton ray paths using the exact geometry of our model, we find that a large number of protons travel for a longer distance on the far side (top side) than on the near side (bottom side) by about 50 to 60 microns. Therefore, the deflection by the near and far side could not be canceled out.

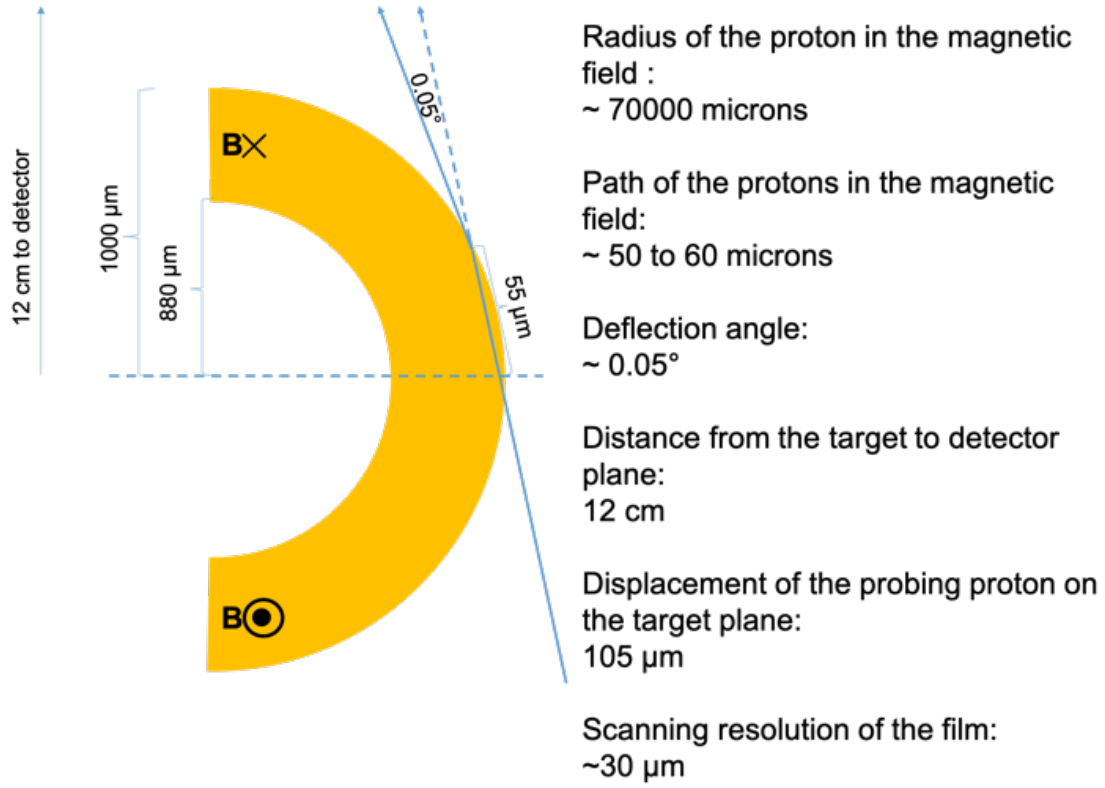

Figure 5.11: Diagram showing the deflection of the oblique incident proton by the magnetic field.

As a back-of-the-envelope calculation, the final deflection effect can be considered the same as if a proton would purely interact with the top part of the hemisphere for a distance of 50 to 60 microns. According to the Lorentz force formula and the theory of particle movement in fields, protons will go in a circular path in a magnetic field with

only direction change. The radius of the circle can be calculated by the equation

$$qvB = m\frac{v^2}{R} \tag{5.1}$$

where q is the particle charge, v is the particle velocity, m is the particle mass and R is the radius of gyration. The deflection angle by a magnetic field of a particle can be expressed as:

$$\alpha_{deflection} \approx \frac{eB\Delta l}{\sqrt{2m_p E_p}} \tag{5.2}$$

where $\alpha_{deflection}$ is the deflection angle, B the magnetic field intensity, d the distance a proton traveled within the magnetic field, m_p the mass of the proton and E_p the kinetic energy of the proton. By substituting numbers from the studied case, where E_p is $\sim$ 15 MeV, B is $\sim$ 7 T, Δl is $\sim$ 60 μm, the deflected angle of a proton by the field is $\sim 0.05^\circ$ as shown in Fig. 5.11. Given the distance from the target to the radiography detector plane 12 cm, the displacement of a proton on the detector plane will be $\sim$ 105 μm, which is larger than the scanning resolution of the film $\sim$ 30 μm by a factor of more than 3. Consequently, the protons' accumulation or depletion due to such a deflection is observable on the radiography films.

In spite of the qualitative description above, the imagination of the particle trajectory in 3D space is not trivial, and therefore, we present some quantitative results calculated by the 3-D particle tracking program, which illuminated the details of proton movements in the field. The tracking program is capable of performing precise calculations of proton probing at various angles by simulating the trajectories of a large number of proton rays individually for statistical analysis.

Fig. 5.12 shows the projection of proton trajectories on the x-z plane (detector plane) by the 1.53° probing angle. A calculation for more than a thousand protons is

shown. On the scatter plot Fig. 5.12 orange dots represent the undeflected positions of the protons and blue dots show their positions after field deflection.

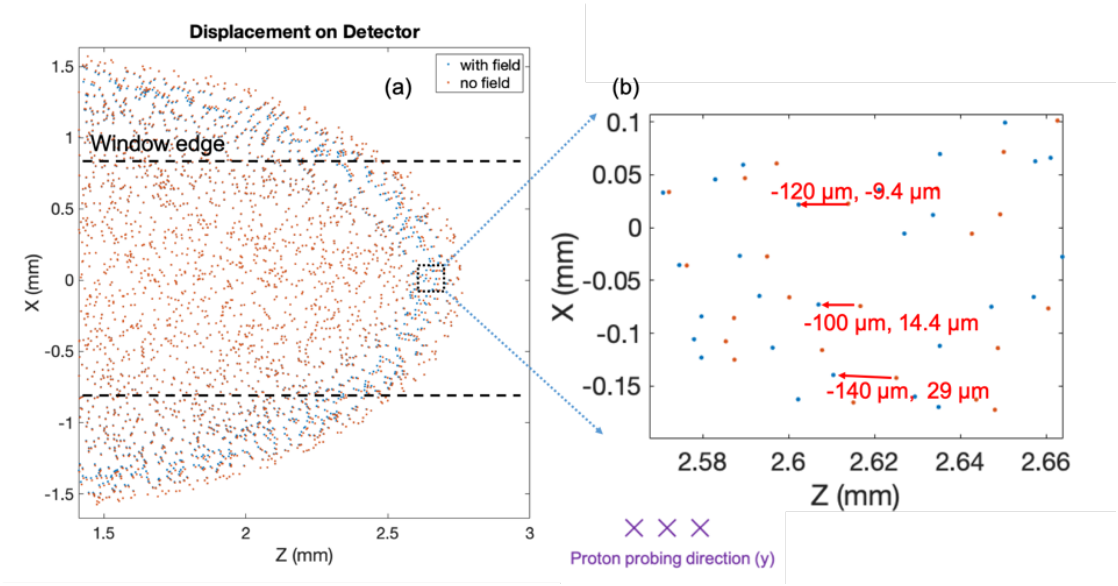

Figure 5.12: projection of proton trajectories in the x-z plane for oblique incident angle 1.53°. The orange dots denote the undeflected position of protons and the blue dots show their position after field deflection. On (b) red arrows indicate the displacements of several representative protons and the exact deflection values are labeled in the format (delta x, delta z).

The separation between the orange and blue dots takes place along the boundary of the semicircle (corresponding to $-1°$ as the reviewer mentioned). In the middle area within the window (corresponding to close to $-6°$ as the reviewer mentioned), the blue and orange dots overlap due to negligible deflection. The area surrounded by the dashed black box is zoomed in on Fig. 5.12(b), where some examples of the displacement values are labeled, which are consistent with our estimation above. To compare, we present the displacement plot for the normal incidence (0°) case shown in Fig. 5.13, on which deflections are too small to be recognized.

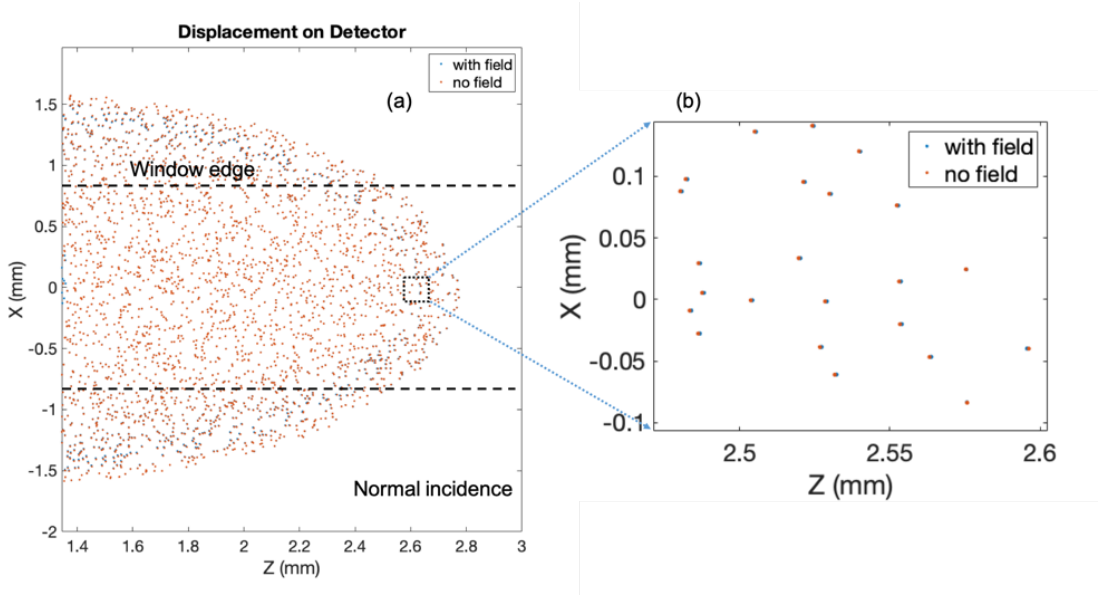

Figure 5.13: Proton displacement plot for the normal incident case.

5.3.2 3-D Magnetic field spatial distribution

According to the geometry of the experimental system, the magnetic field can be considered as azimuthally symmetric. Here, we investigate the spatial variation of the field along the other two axes given a spherical coordinate, the radial distance 'r' and polar angle 'θ', the angle from the z-axis.

5.3.2.1 Along radius within the shell

Similar to the analysis for the magnetic strength and field thickness, we investigate the field variation along the radius in the shell by forward fitting the experimental data. Given the fact that the width of the shell is on the order of 120μm, $\sim$ 5 times of the resolution limit, it was expected to sketch the outline of the field spatial profiles without depicting the detailed structures. Two basic models that were tested are the uniform distribution and triangular-shaped distribution as displayed in Fig. 5.14(a).

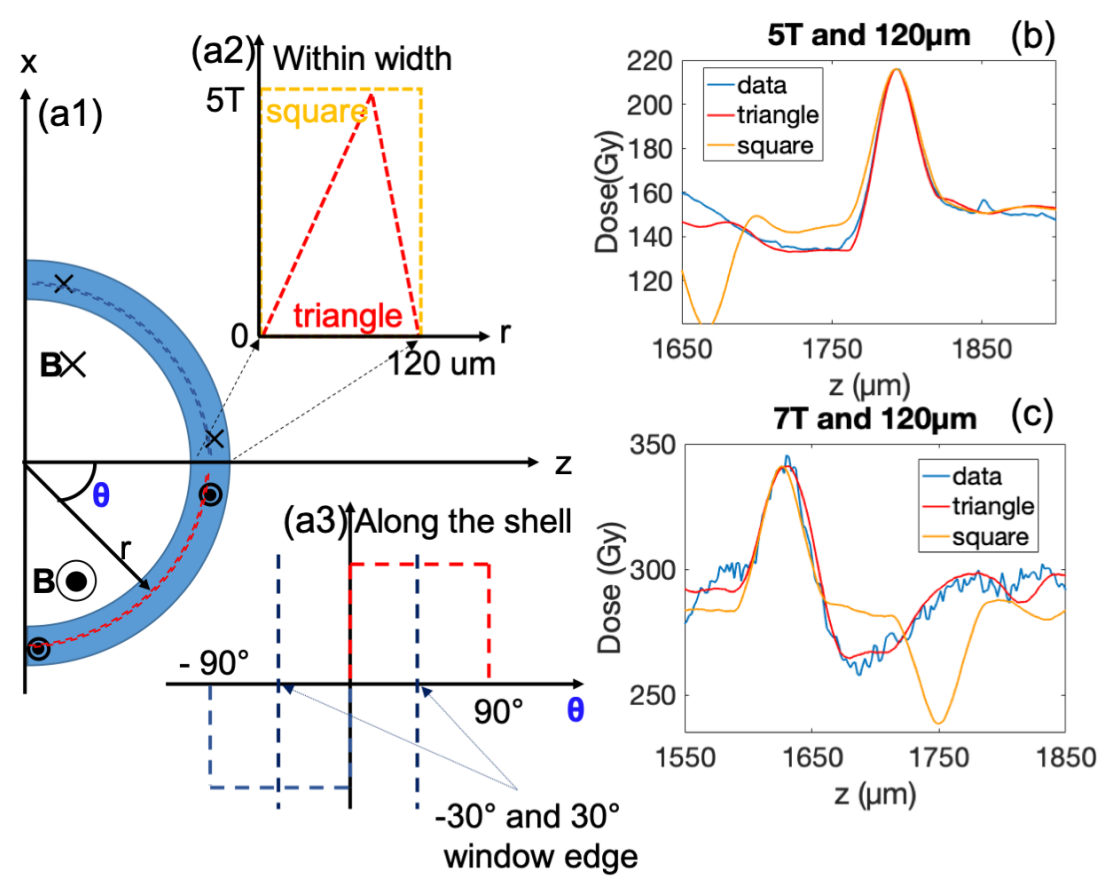

Figure 5.14: (a1)the azimuthal B field polarity within the shell. (a2) the square and triangle profiles along the radius in the spherical coordinates, zero in r-axis is the inside position of the shell. (a3) the uniform field distribution along the polar angle θ (angle from z-axis). (b) and (c) respectively show for 'proton source 1' and 'proton source 2' the good agreement between the experimental RCF data and the simulated RCF with a triangle profile B field.

The latter case, though simple, provides a reasonable approximation. Lineouts from simulated radiography images in comparison to that from the experimental measurement are plotted in Fig. 5.14(b) and (c) respectively for data from 'proton source 1' and 'proton source 2'. The blue curves in both plots represent the experimental data and the yellow curves show the results from the square distribution. The sharp edges of the square profiles lead to much deeper depletion ($\sim$ 1650 in (b) and $\sim$ 1750 in (c) along the z-axis) in the simulated proton signal than that in experimental data. This indicates a

more smooth field variation within the shell and inspires us to test the triangular-shaped distribution. The results are plot in red in plot (b) and (c) respectively for proton sources '1' and '2', both of which reach good agreements with the experimental profiles. The peak position of the triangle was also a free parameter in 25μm increments. In Fig. 5.14(b), the best fit was a triangle with peak 25μm from the outside, while for (c) the best fit was for a triangle with centered peak. This difference is considered reasonable given the shot to shot variation.

5.3.2.2 Along the shell (polar angle)

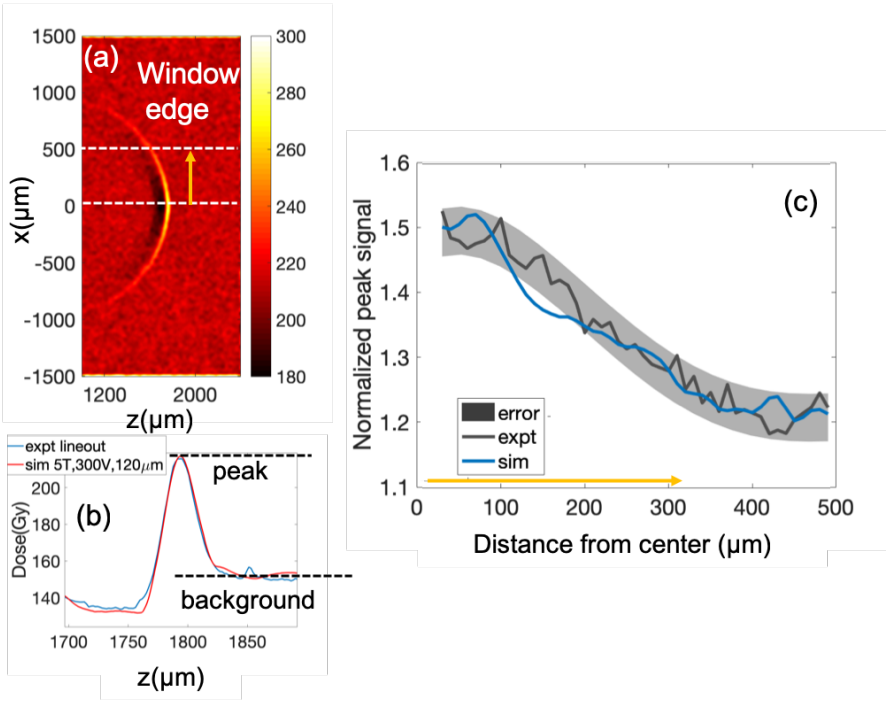

Figure 5.15: (a) the simulated RCF image. (b) the lineout from the center axis of the ring. The blue curve represents the experimental data and the red curve represents the simulation result. (c) Normalized peak signal along the longitudinal direction. the y-axis is the ratio of peak signal to the background signal and x-axis is the distance from the window edge (as indicated by the arrow in (a))

The field strength along the shell is uniformly distributed in the 3-D particle tracking program as shown by Fig. 5.14 (a3), on which θ represents the polar angle

from the z-axis. Within the window size, which corresponds to θ varying from -30°to 30°(sinθ = 500μm/1000μm = 0.5), this simple uniform model is found to be a reasonable approximation to properly interpret the data. To avoid invoking an infinite axial current density exactly on the axis, we artificially set the field strength to be zero within a few steps from the axis, which addressed the concern without posing noticeably impacts on the particle trajectories because the step size is as small as less than one percent of the shell width.

The fair agreement is noticed between the experimental and simulated results in terms of the proton signal variation (ratio of the peak value to the background value) along with the shell as shown by Fig. 5.15(c). A detailed explanation of this plot is provided next. Fig. 5.15(a) shows a simulated radiography image from the magnetic field, whose strength, thickness and spatial profile along z-axis within the shell are all set at their best-fitting values and uniform distribution along the shell is applied. From the image, we extracted the horizontal lineouts at 50 different vertical positions from the central axis to the window edge, and then obtained the ratio of the peak signal value to the background signal value for each slice. An example of the peak and background signals along the lineout is shown in Fig. 5.15(b), which is taken from the center axis. Variation of the obtained ratio along the shell is plotted in Fig. 5.15(c), the horizontal axis of which represents the vertical distance from the central axis of the shell and the vertical axis represents the normalized peak signal. The dark gray curve in Fig. 5.15(c) shows the result measured from the experimental image with the error-bar displayed by the light gray zone. The blue curve shows the result from the simulated image, which reasonably matches the experimental profile.

The magnetic field topology described in this section in the particle tracking was qualitatively based on the LSP prediction in terms of azimuthal polarity, the nearly triangular width profile and uniform along-shell distribution. The strength 5 to 7T found in the

particle tracking fit is comparable to the 4T calculated in LSP. A quantitative agreement for scale length was not expected due to the much smaller simulation box. While the field shell model is very simple, it allowed a rapid search of possible field topologies and ultimately found well-fit solutions reproducing the experimental radiographs.

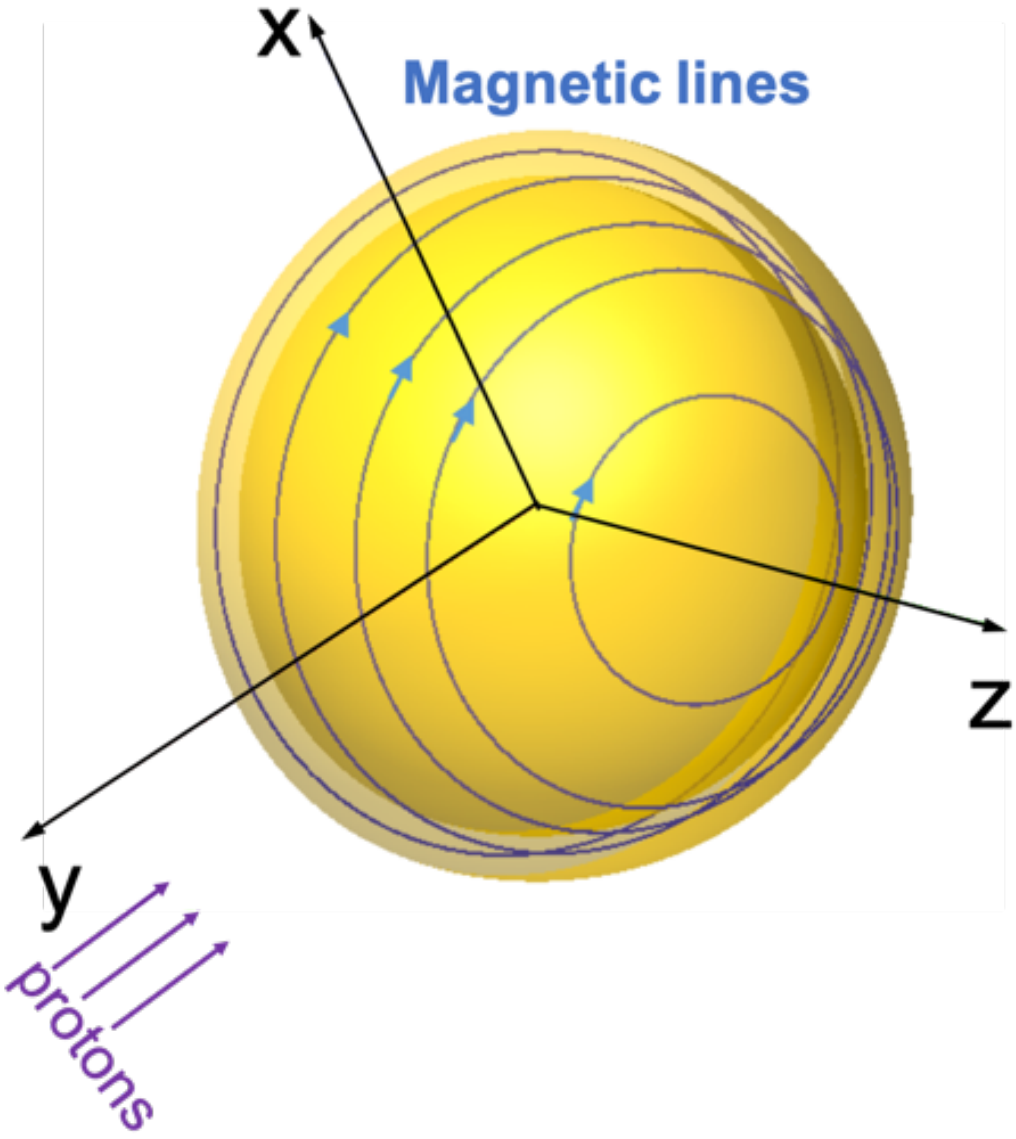

Figure 5.16: 3D diagram showing magnetic field orientation in a semi-spherical shell. Magnetic lines are shown in blue circles.

A 3D diagram of the magnetic fields located in a semi-spherical shell is displayed in Fig.5.16, on which the blue circles with arrows represent the magnetic lines and protons are traveling against y-direction.

5.3.3 Fitting Error Analysis

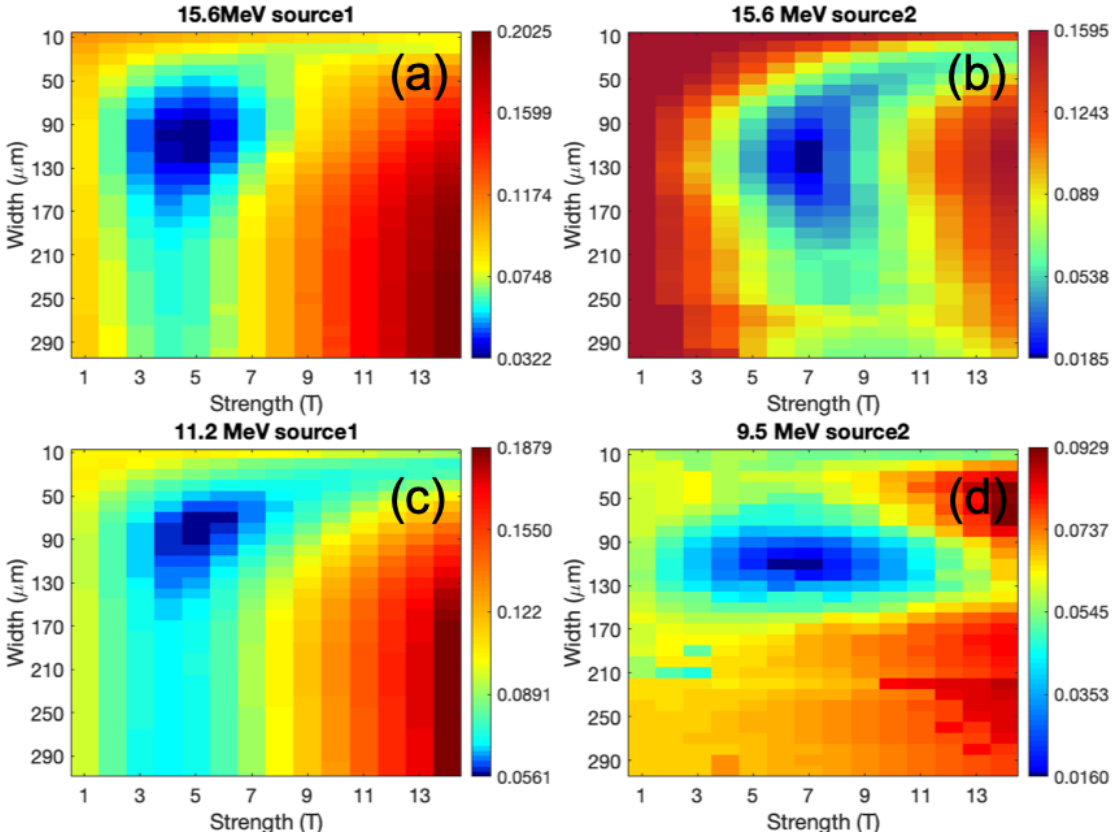

Figure 5.17: Fitting error maps for (1) 15.6 MeV proton radiograpy data at source 1, (b) 15.6 MeV proton radiograpy data at source 2, (c) 11.2 MeV proton radiograpy data at source 1 and (d) 9.5 MeV proton radiograpy data at source 2.

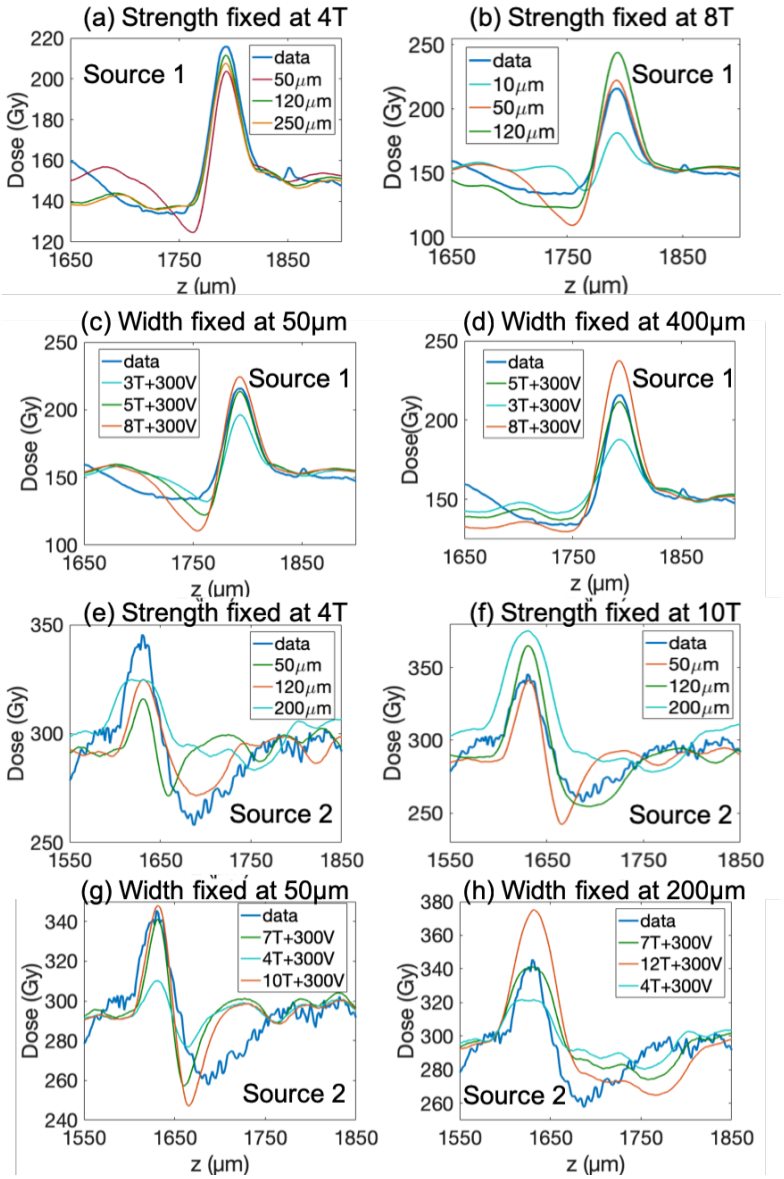

Figure 5.18: Lineouts from the center axis of the proton rings both from experimental and simulated data. The blue curve on each plot represents the experimental measurement. The top row shows the results from 'proton source 1' and the bottom row shows those from 'proton source 2'. (a), (e) display the cases when magnetic intensity is 4T, smaller than best-fitting value and (b), (f) display when its larger at 8T and 10T respectively for the two sources. (c), (g) show the cases when the field thickness is 50μm, narrower than the best-fitting value and (d), (h) show when it is wider, 400μm and 200μm respectively.

Fig. 5.17 displays the four individual error maps. As mentioned in the manuscript, the fitting error is calculated as $\sqrt{\frac{1}{n}\Sigma\frac{(D_i-S_i)^2}{D_i^2}}$, where D_i represents data, S_i the simulation, and n is the number of points selected. The area from 1600μm to 1800μm along the z-axis is covered. The blue color on the color bar represents for smaller error thus better fitting and red color for larger error thus worse fitting. The best fit magnetic field for each radiography from (a) to (d) respectively converges to: 5T, 120μm; 7T, 120μm; 5T, 90μm and 7T, 110μm. Taking into consideration the average fitting error map displayed in Fig. 5.9, the magnetic field determined by the four radiography data is 6 ± 1 T, 110 ± 20 μm.

Next, we show some misfit examples. As indicated by the fitting error maps, when one of the two parameters, field thickness, and magnetic strength, diverge from its best-fitting value to a certain degree ($\sim \pm 50\%$), the experimental images cannot be reasonably fit regardless of the other parameters. As Fig. 5.18 shows: if the magnetic strength is too small as shown in (a) and (e), the peak signal in the experimental profile cannot be reached no matter what spatial profile is used and how narrow or wide the scale length is. If the strength is too large as shown in (b) and (f), though the peak signal is reproducible, the overall experimental profile cannot be precisely fit by the simulation regardless of the magnetic strength and spatial profile. When the field thickness is too narrow as shown by (c) and (g), the variations of the simulated profiles happen in a narrower scale length in comparison to that in the experimental profile; On the contrary, when the field thickness is too wide as shown by (d) and (h), the scale length of the variation is wider in the simulated profiles compared to that in the experimental data no matter what magnetic strength is used.

5.4 Shock front temperature and density by an X-Ray spectrometer

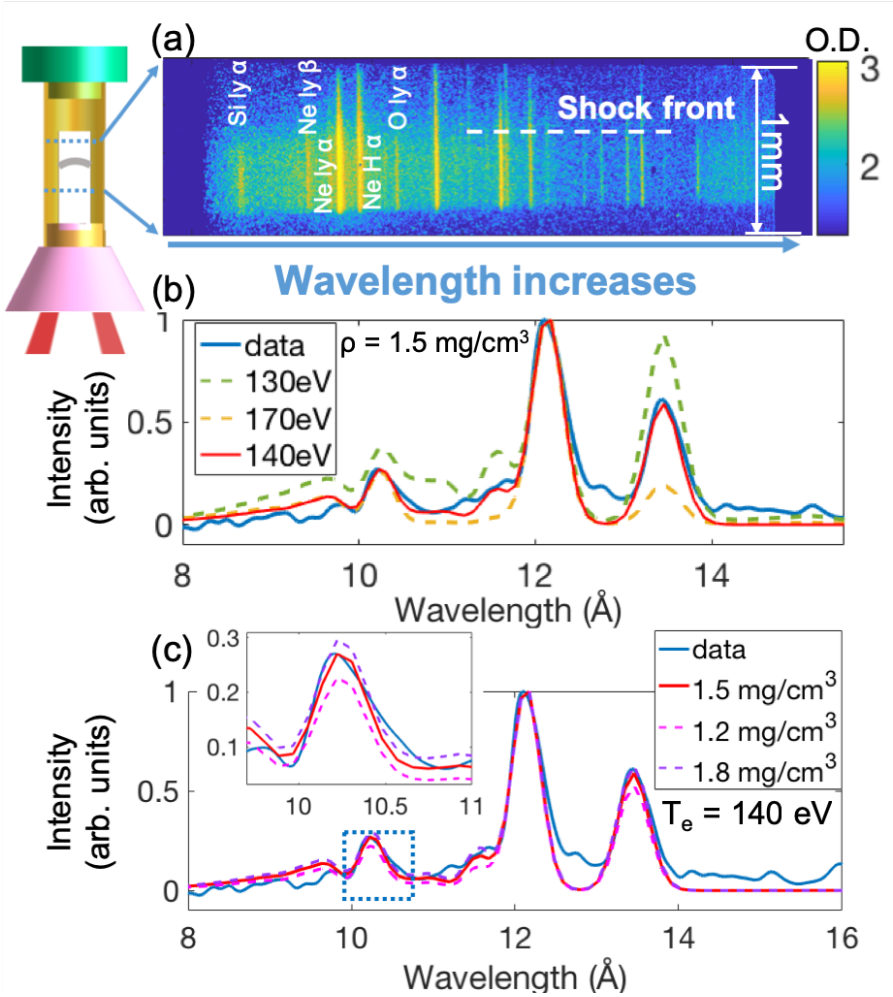

Figure 5.19: (a) Typical VSG data of a shot with 90% helium and 10% neon initially at 1 atm, 0.24 mg/cm^3. Silicon lyman-α, oxygen lyman-α from the ablator and neon lyman-β, neon lyman-α from the gas are labeled. (b) Spectrum showing neon lines within 8 Å to 16 Å. Blue curve is experimental data and red curve is the best fitting at 140 eV and 1.5 mg/cm^3. The two dashed curves display the temperature sensitivity when it deviates from 140 eV to 130 eV or 170 eV while density is fixed at 1.5 mg/cm^3. (c) Magnified region over lyman- β line to show the density sensitivity by varying it to either 1.2 mg/cm^3 or 1.8 mg/cm^3. Temperature is fixed at 140 eV.

Another primary diagnostic, a 1-D resolved soft X-ray spectrometer, known as a VSG (Variable line Spaced Grating spectrometer) [70], measured the shock temperature and density by looking through one of the windows, constraining the conditions for both magnetic and electric field generation. Four snapshots at different times can be taken during each laser shot using a framing system. Its field of view is ~ 1 mm along with the shock and it captures photons in the energy range ~ 0.2 to 2 keV.

Fig. 5.19(a) displays typical VSG data taken 2.6ns after the shock initiation. The horizontal axis here represents increasing wavelength (decreasing photon energy) and the vertical axis represents the spatial length (along which the shock propagates from bottom to top). We identify the abrupt change in continuum emission as the location of the shock front. By the designed fiducial, a clip on the bottom of the raw data, we were able to correlate the VSG data with the radiography data in terms of space, therefore identifying the shock front location, which coincides with the abrupt change in the continuum emission marked as the horizontal white dashed line.

On the gas tube, the front edge of the VSG window (the edge close to the ablator) was designed to fall into the field of view of the spectrometer as shown by Fig. 5.20. Fig. 5.20 (c) shows a shadowgraph of a target before shot, on which the VSG window is marked by a white dashed box. The left edge of the window was designed to be within the field of view of the x-ray data, which can be recognized on Fig. 5.20(b) as labeled in white. The black horizontal line indicates the determined shock front position. The black vertical line on Fig. 5.20(a) marks the shock position at 3 ns by RCF, for which the corresponding position at 2.6 ns, timing for VSG data, is drawn as a white semicircle on Fig. 5.20(c). According to the geometry, the position of the shock front position recognized in VSG data is consistent with that from the RCF measurement.

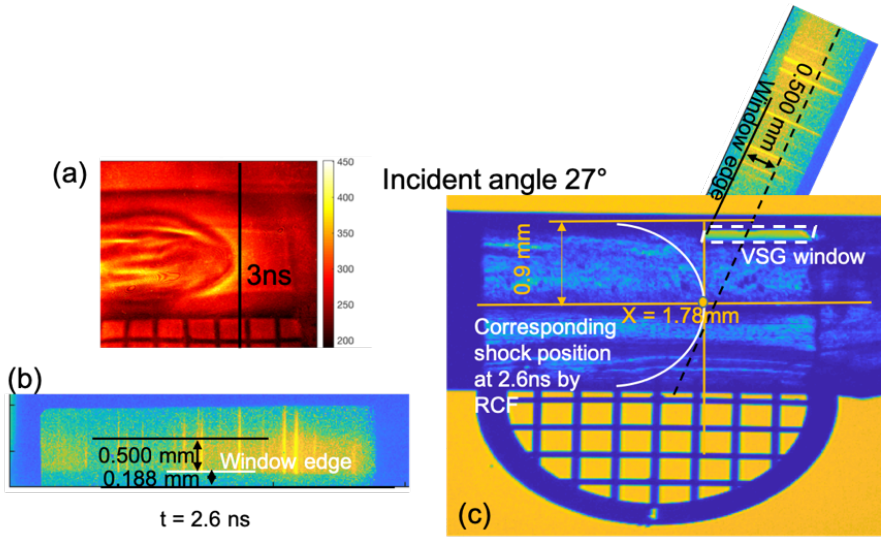

Figure 5.20: Scheme showing the correlation of shock front positions observed by RCF and VSG

Since helium lacks detectable lines within the spectral range, 10 % neon gas was added as a tracing gas, from which lyman-α, lyman-β and helium-like-α lines are identified. Lines corresponding to silicon and oxygen, present in the ablator material, are also shown.

As the line ratios change with temperature and density, we are able to infer the conditions at the shock front to be 140 ± 5 eV and ~ 1.5 mg/cm^3 by best fitting the data with simulation results from the collisional-radiative atomic code PrismSPECT [40]. The ratio of Lyman-α to helium-like-α is mostly sensitive to and constrains the temperature, while the ratio of Lyman-α to Lyman-β constrains the density. Plots (b) and (c) in Fig. 5.19 show the fitting process. On each plot, the solid blue curve represents neon emission lines at the shock front and the red solid curve displays the best fit. Two additional dashed curves describe the fitting sensitivity of temperature, on plot (b), and density, on plot (c), by showing the deviations when the parameters depart from their best-fitting values. The small measurement error in temperature arises mainly from the uncertainty of background subtraction.

An electric potential of ~ 300 V can be obtained from the above shock conditions according to $\Delta\Phi \approx ln(\rho_2/\rho_1)k_B T_e/e$. In contrast to previous work [23] which only considered the effect of the electric field on the proton trajectories, we find the electric field's contribution is negligible in comparison to the effect of the magnetic field. For reference, the light blue curves in Fig. 4(a) and (b) in the main manuscript show the simulation results by a 300 V electric potential from the two proton sources. Regardless of the field spatial profile, its contribution is negligible in comparison with the experimental data.

5.5 Particle in Cell Simulation of Shock Propagation

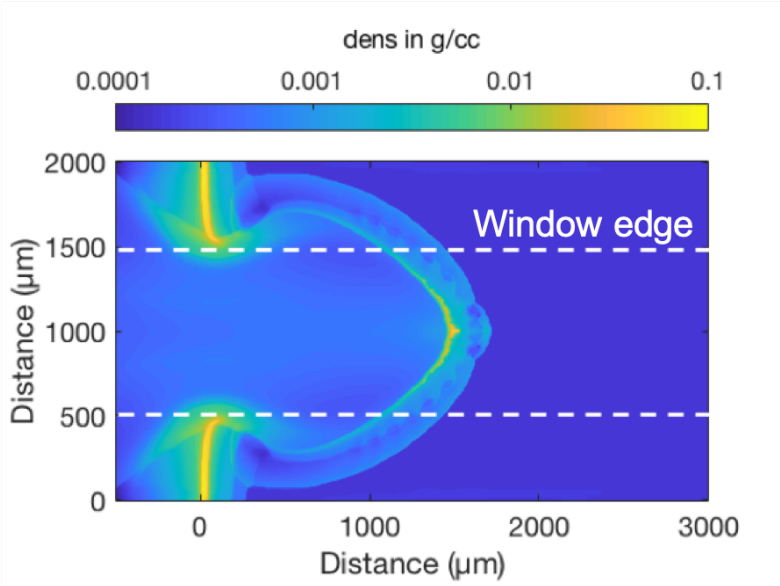

Figure 5.21: 2D density profile at 3ns by FLASH simulation. A laser beam, whose intensity was adjusted to be 50% of that used in the experiment, was used in order to match the shock propagation distance ~ 1.8μm. The spot size of 750μm for the laser was applied. The ablator was set as a 2μm SiO_2 and the inital filled gas as helium at 1 atm.

The generation of the discussed magnetic field is attributed to the Biermann Battery effect. The ablator is $\sim$ 1.9mm in diameter, the central part $\sim$ 750μm of which pushed into the gas with extremely high velocity by laser ablation. The density evolution, determined by advection and the temperature evolution, determined by thermal diffusion, obey different physical processes and therefore eventually evolve into different spatial distributions during the shock propagation. To further investigate the field evolution, we simulated the shock propagation using the particle-in-cell code LSP [92] with an implicit, hybrid method [15]. The initial density and temperature conditions are taken from the VSG measurement at 2.6ns and the initial density variation along the x-axis calculated by the radiation-hydrodynamic code FLASH [39] was applied. In the simulation, a hot-dense plasma – n_e of 2.4×10^{21} cm^{-3} (Gaussian profile in the transverse direction) and T_e of 150 eV – moves toward a uniform low-density plasma – n_e of 0.34×10^{21} cm^{-3} and T_e of 10 eV – with a velocity of 600 km/s. The simulation box is 400μm by 400μm, smaller compared to the target size due to the consideration of computational expense. The central part of the compressed region penetrates further into the low-density plasma due to its higher initial density, resulting in a slight bulge at the shock front as shown by Fig.5.22(a). The temperature contour becomes curved as the shock propagating, thus resulting in a transverse gradient as displayed by the arrow on Fig.5.22(b). According to the Biermann battery effect [55], non-parallel density and temperature gradients drive an azimuthal magnetic field, shown in Fig.5.22(c). The peak value reaches more than 4 T in the simulation at 200 ps and is sustained until 300 ps, when the simulation ended. The magnitude of the magnetic field fluctuates within $\sim$ 15% when the flux limiter varies from 0.1 to 0.8. Besides, the shock driven electric potential reaches $\sim$ 500V in the simulation, which is the same order of magnitude as the experimentally-derived estimate shown above.

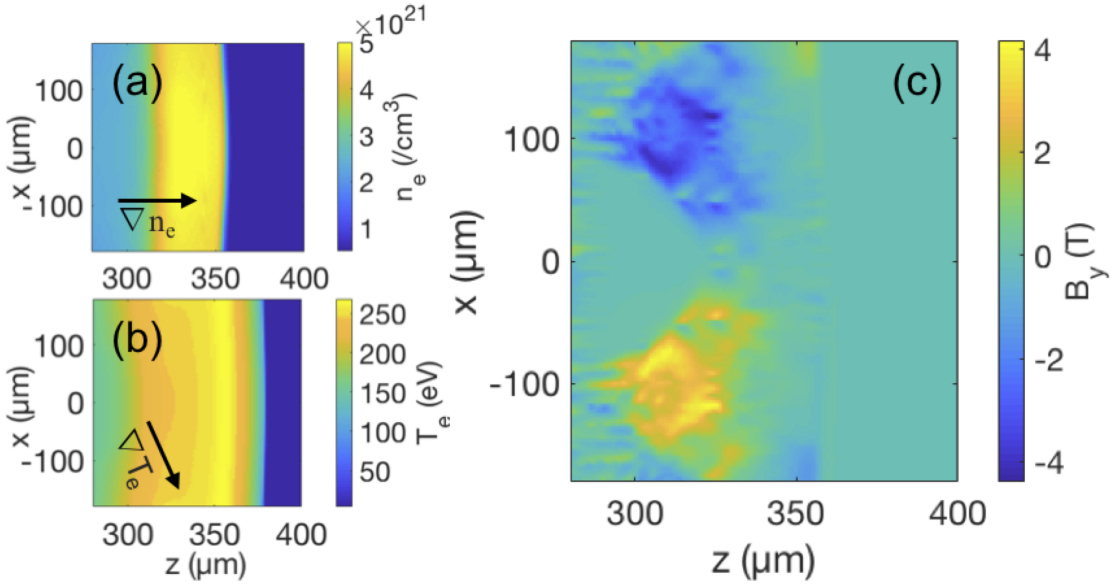

Figure 5.22: (a) and (b) Density and temperature map from the PIC simulation by LSP at 300 ps. (c) Simulated azimuthal magnetic field structure at 300 ps.

5.6 Analysis for data by lower energy protons

The manuscript is focusing on the 15.6 MeV proton data due to its superior image quality. The same analyzing process was also applied to data by multiple energies below $15.6MeV$, from which consistent results with the variation within 1 to 2 T in terms of magnetic field intensity were extracted. Here, radiography data by 9.5 MeV protons from the proton source location 2 and 11.2 MeV protons from the source location 1 as well as their best fittings from simulation results from the 3-D particle tracking code is present as shown on Fig.5.23 and Fig.5.24.

On the plots, (a) and (b) respectively represent the experimental and simulated radiography data from 9.5 MeV and 11.2 MeV protons. (c) shows the quantitative comparison in terms of the central lineouts across the shock front, on which the blue curve represents the experimental data and the red curve shows the fitting by simulated image. The field setup for best fitting the 9.5 MeV data includes a magnetic field of peak

intensity at 7T, thickness of 110μm and a 300 V electric field. To best fit the 11.2 MeV data, the fields are set to be a magnetic field at 6T, thickness of 90μm and an electric field of 300V. Despite the observed shock front signals are not as sharp as that by the 15.6 MeV protons due to the inferior resolution as probing proton energy decreases. Reasonable fittings are achieved by applying the structure of the fields that are in good agreement with those extracted from radiography data by protons at 15.6 MeV.

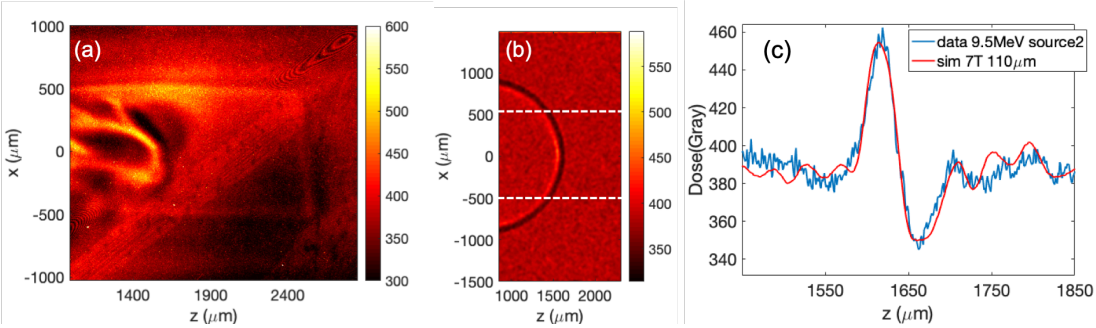

Figure 5.23: (a) RCF image from proton energy of 9.5 MeV from proton source location 2.(b) simulated RCF image. (c) quantitative comparison of lineouts between experimental measurement and simulation result, profiles of which are respectively represented by the blue and red curves. The field setup for the best fitting in the simulation includes a magnetic field of peak intensity at 7T and thickness to be 110μm as well as the 300 V electric field.

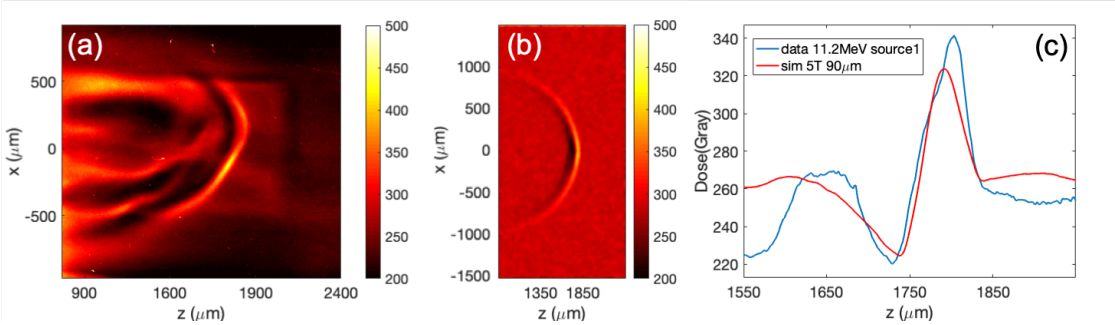

Figure 5.24: (a) RCF image from proton energy of 11.2 MeV (b) simulated RCF image from proton source location 1. (c) lineouts comparison. The blue curve shows the experimental profile and the red curve shows the simulated profile. The simulation setup including a magnetic field of peak intensity at 5T and thickness to be 90 μm. A 300 V electric field is included.

In summary, we have observed the magnetic field associated with a Mach ~ 6

shock front and characterized its structure by varying the incident angle of probing protons. Quantitative analysis indicates the field profile $\sim$ 5 to 7 T with a characteristic width of $\sim$ 120 μm. An X-ray spectrometer inferred the density and temperature at the shock front, constraining the electric potential to be 300 V. Contrary to the common interpretation that proton deflectometry is mainly caused by the electric field, we find the effect of the magnetic component of the Lorentz force dominates the signal. Further investigation with PIC simulations indicate that the field is mostly generated by the Biermann Battery mechanism.

Chapter 5, in full, is currently being prepared for publication as R. Hua, J. Kim, M. Sherlock, M. Bailly-Grandvaux, F.N. Beg, C. McGuffey, S. Wilks, H. Wen, A. Joglekar, W. Mori, Y. Ping "Self-generated magnetic and electric fields at a Mach-6 shock front in a low density1helium gas by dual-angle proton radiography", The dissertation author was the primary investigator and author of the paper.

Chapter 6

Study of shock precursor in low-density Multi-Species gases

Spatial profiles of density and temperature of a strong shock including the entire precursor region are observed respectively in a helium gas mixture (90 % helium, 10 % neon)and a pure neon gas using a 1-D resolved soft X-ray spectrometer. With comparable peak electron temperatures at the shock fronts, a precursor layer, where electron temperature is far more than ion temperature, extending for more than $\sim$ 500 μm was observed in the helium gas mixture. While in the pure neon gas, the distance of the precursor was observed to be less than 30 μm. At the shock front, the electrons are strongly collisional with their mean-free-path two orders less than the characteristic length of the shock. The radiation-hydrodynamic simulation is performed to investigate the impact of thermal conduction on the formation of the precursors. PIC simulation is also performed since the ion movement falls in the kinetic region. The results indicate that hydrodynamically, the dependence of heat flow on the charge state Z plays a role in the formations of precursors in the two gases. Kinetically, there is a group of fast

streaming ions ahead of the shock existing only in the helium gas mixture, which also potentially contribute to the formation of longer precursor layer in the helium shock. The content presented in this section is in preparation for submission.

6.1 Introduction

Strong shocks are ubiquitous in astrophysical systems and play a driving role in inertial confinement fusion (ICF) efforts. In the context of ICF with a spherical fuel capsule [2, 93], shocks[5] travel to the center in a low density plasma at high velocity ($\sim 10^2$ to 10^3km/s), resulting in a dramatic increase in the ions' kinetic energy and mean-free-path that eventually becomes comparable to the characteristic length of the target. Consequently, the kinetic effects of the ions become significant. Similarly, in the astrophysics system, the plasma is so tenuous that the ion-ion mean-free-path can become large so that ions behave kinetically [6, 7]. As a consequence, those phenomena accentuate the role played by kinetic effects on shock physics [11, 12], and inspire the studies both based on Vlasov-Fokker-Planck theory [13, 14] and particle-in-cell simulations [15]. Application of those theoretical and simulation tools to these areas led to the discoveries of new effects such as electric current[16], charge separation[17] and electro-diffusion [18] at the shock front.

The shock structure has been studied extensively with theoretical frameworks. Traditional hydrodynamic treatment of a plasma shock consists of three layers: (i) the ion and electron equilibrium layer trailing the shock, (ii) the compression ion shock layer in which density drops dramatically, and (iii) the precursor layer which consists of heated electrons and cold ions [53, 12]. The length of both the equilibrium and precursor layers are $\sim \sqrt{m_i/m_e}\,\lambda_{ii}$ (where m_i and m_e are the ion and electron masses, respectively, and λ_{ii} is the ion-ion downstream mean free path), whereas the compression region is a few

ion-ion mean free paths long.

More details of a shock front structure are uncovered with the consideration of kinetic behavior. Discovery of a double-humped (non-Maxwellian) ion distribution in the precursor region [13], by Fokker Plank derivations, suggested the existence of a group of forward streaming ions in excess of the shock velocity [94]. It was also reported that such ions cause enlargement of the precursor as they undergo stopping by electron friction, heating electrons effectively [14]. Keenan *et al.* [12] quantitatively described the dependence of the shock width on the Mach number. Those authors later emphasized the existence of species' separation effects when multiple ions are present [54]. In a two-ion plasma shock, the concentration of the lighter ion species is kinetically enhanced throughout the shock front, particularly in the precursor layer.

Despite the multiple studies from theoretical and computational approaches on the shock structure, experimental evidence is deficient. Recently, Rinderknecht *et al.* [85, 95] reported the observation of double velocity components in a precursor ahead of a shock front. However, the single measurement taken in hydrogen gas is insufficient for comprehensively understanding the dependence on the material of the shock structure.

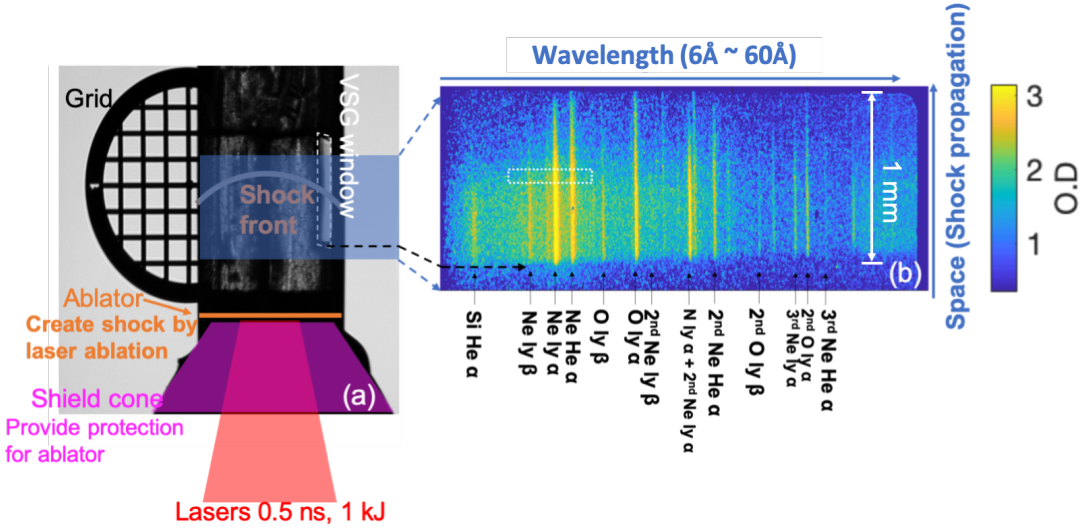

Figure 6.1: (a) shows the experimental layout of the horizontal gas target, which is oriented vertically here. The laser irradiates an ablator inside a shield cone with the direction indicated in the drawing, creating a shock traveling to the top. (b) Typical VSG data of a shot with 90% helium and 10% neon initially at 1atm, 0.24mg/cm^3. The vertical axis represents space along the shock propagation direction and the horizontal axis represents the dispersion of photon energy. The color-bar unit is optical density as labeled by O.D. The white box indicates the location of the spectrum that will be discussed in Fig. 6.2.

This paper presents the measurement of the spatial structure spanning from the shock front through the entire precursor region for two gas types: a helium gas mixture (90% helium and 10% neon) and a pure neon gas. Different precursor distances are detected depending on the gases. In the helium gas mixture, a long precursor over 500μm is observed while in the pure neon gas, the precursor is not measured. Radiation hydrodynamic simulation displays qualitative agreement with the experimental observation of the preheat region scale when setup with an appropriate background temperature. Particle-in-cell simulation reveals a population of fast streaming ions streaming from the shock that is present in the 90% helium gas mixture but not in the pure neon, potentially contributing to the precursor formation.

The paper is organized as follows: Section 6.2 describes the experimental design

and data analysis that shows a much longer precursor length in the helium gas mixture than that in pure neon shock. Section 6.3 discusses the collisionality of the particles involved in the shock and interprets the simulation results by a rad-hydro code in 6.3.1 and a particle-in-cell code in 6.3.2. A comparison of these simulations to data is included. Section 6.4 provides conclusion.

6.2 Experimental setup and data analysis

The experiment was performed on the OMEGA-EP Laser Facility. Two square-shaped laser pulses delivering a total of 1kJ in 0.5ns were used for shock initiation. The spot size of these overlapped beams was $\sim$ 750μm. The main target was a cylindrical Kapton tube containing either a gas mixture of 90% helium and 10% neon or pure neon at 1atm [58].

The layout is shown in Fig. 6.1(a). The target was a cylindrical tube, and lasers came along the tube axis, initiating strong shocks by the ablation of a 2μm SiO_2 foil placed on the end of the tube [27]. The shocks traveled into the gas tube at a velocity of $\sim$ 450 to 600km/s respectively for the neon and helium gases. The pink cone attached to the cylinder is a debris shield to protect the ablator. The semi-circular shaped grid attached to the side of the tube was used as a spatial reference. Due to the smaller size of the flat-top laser spot with respect to the ablator $\sim$ 1.8mm, the central part of the ablator was pushed further, consequently leading to a hemispherical shaped shock front, as represented in the layout figure.

A 1-D resolved x-ray spectrometer, called VSG (variable line spaced grating), [70] was fielded to record the self-emitted light from the vicinity of the shock through a 1μm Kapton window on the tube. Analyses of the spectra recorded by the VSG provide constraints for density and electron temperature at the shock front. A shadowgraph of the

gas target is shown in Fig. 6.1(a).

The spatial field of view of the VSG is $\sim$ 1mm and its spectrum range is from 200eV up to 2keV ($\sim$ 6 to 60), covering some of the characteristic emission lines from neon, oxygen, carbon and nitrogen. The VSG is equipped with a framing camera acquiring four times during one shot to capture the shock at different instant snapshots. The exposure time for each frame is 400ps. The X-ray self-emission from the plasma at the shock front was recorded by a piece of film. a $\sim$ 0.5μm thick Aluminum filter was placed in front of the film to protect it from saturation.

An example of the raw soft X-ray data is shown in Fig.6.1 (b). The horizontal axis represents the dispersion of the wavelength that increases from the left to the right. The vertical axis represents the spatial length along which the shock traveled from the bottom to the top. The spatial resolution is on the order of $\sim$ 30μm.

The spectral and spatial analysis of the raw image are provided separately in the following sections 6.2.1 and 6.2.2.

6.2.1 Spectral analysis

In this section, we focus our analysis on the spectrum information from the raw image data. Along the wavelength axis of Fig. 6.1(b), several characteristic emission lines are detected and recognized. The neon lines come from the gas of interest, the silicon lines from the SiO_2 ablator, the nitrogen lines from the Kapton wall of the tube and the oxygen lines from the ablator and from the Kapton wall. Each line is labeled including the order of emission.

To get the information of the plasma at the shock front propagating in the gas, our analysis concentrates on the Ne lines coming from the filling gas. Specifically, the Ne Ly_α, Ly_β and He_α are forward-fit by the simulation results from the collisional-radiative

atomic code PRISM-SPECT [40] to determine the electron temperature and density of the plasma at the shock front. PRISM-SPECT can compute the ionization properties and the spectral properties, including emission and absorption, for given plasma conditions.

To infer the plasma condition at the shock front, a large set of simulations for various plasma temperatures and densities were performed and the corresponding spectra were calculated. Each simulated spectrum was compared with the experimental measurement. The plasma condition is then determined as the one that produces the simulation result which best fits the data.

An example spectrum measurement taken as a lineout from the raw image of the helium gas mixture shot is shown on Fig.6.2. The lineout location, indicated by the white dashed rectangle box on Fig. 6.1(b), was close to the shock front. The identification of the shock front position will be discussed in the next section. The spectrum plotted in has been zoomed in to display only the characteristic emission lines of Ly_{α}, Ly_{β} and He_{α} from the neon ions. In the analysis, we concentrate on the ratios among the characteristic lines rather than their absolute intensities. Therefore, the spectrum signal was normalized to the peak value as displayed by the vertical axis. background corrections corresponding to the applied aluminum filter and the 1μm Kapton window were performed.

The solid blue curves on both plots Fig. 6.2(a) and Fig. 6.2(b) show the measurements from the data. Three other curves are displayed showing calculations with PRISM-SPECT at various temperature and density that bound the data.

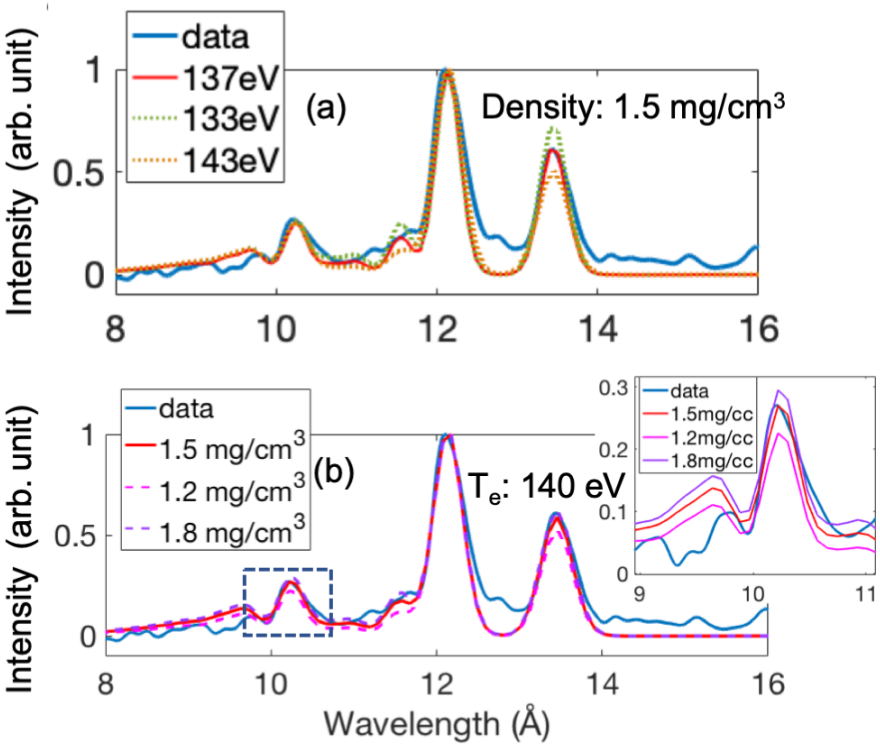

Figure 6.2: (a) Spectrum showing neon lines from 8 to 16, that covers the characteristic lines from neon ions. Blue curve shows the experimental data measured from the helium gas mixture and red curve is the best fitting obtained at 137eV. The two dashed curves display divergence when temperature deviates from 137eV to 133eV or 143eV. Densities for all simulated curves were set at 1.5mg/cm^3. (b) similar to (a) but shows the sensitivity to density change of the simulated curves. Temperature was fixed at 137eV.

To properly forward-fit the spectrum data, both the temperature and density were scanned within wide ranges.

The temperature was explored from as low as 10eV to $\sim$ 300eV and the density was adjusted from the initial undriven density (0.24mg/cm^3 for the helium gas mixture and 0.8mg/cm^3 for the pure neon) to a 20-fold initial density. To display the individual impact on the spectrum respectively for temperature and density variations, we plot the simulated spectra calculated from various temperature at a fixed density in Fig. 6.2(a) and various density at a fixed temperature in Fig. 6.2(b), together with the experimental data and the best-fit simulated curve. Fig. 6.2(a) illustrates the comparison between the

three calculated spectra from different temperature and a fixed density of $1.5\text{mg}/\text{cm}^3$ to the experimental spectrum. The best fit for the experimental spectrum is found at a temperature of 137eV displayed by the solid red curve. This value was inferred mainly using the ratio of Ly_α to He_α that we observed with simulation to be the most sensitive to temperature changes. Indeed, when temperature differs from the best fitting value by $\sim \pm 5$eV in the simulation, the ratio Ly_α to He_α starts to noticeably deviate from the experimental data. On the other hand, Fig. 6.2(b) illustrates the variations related to density changes at a fixed temperature of 137eV. The density that best fits the experimental data of the helium gas mixture shot is found at $1.5\text{mg}/\text{cm}^3$ and was inferred using the ratio of Ly_α to Ly_β which appears to be the most sensitive to density. When density differs from it by $\pm 0.3\text{mg}/\text{cm}^3$ in the simulation, the calculated curves start to diverge from the experimental data noticeably.

6.2.2 Spatial analysis and the comparison between helium and neon shocks

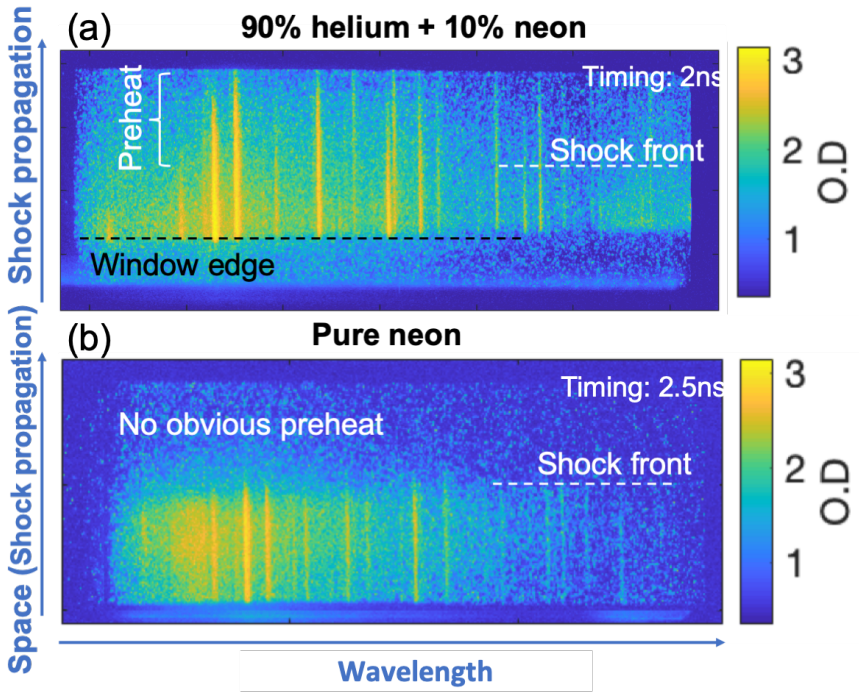

Figure 6.3: (a) VSG data of a shock in the gas mixture of 90% helium and 10% neon initially at 1atm. Timing of the image is at 2ns (b) VSG data of a shock in the pure neon gas. Timing of the image is at 2.5ns. The shocks were propagating along the vertical axes from the bottom to the top and the shock front positions are labeled by the white dashed lines.

In this section, we provide the spatial information inferred from the raw data and focus our analyses on building the spatial profiles of temperature and density along the shocks. Along the vertical spatial axis in Fig. 6.1(b), the shock was propagating from the bottom to the top. A clip, close to the bottom of the image, is visible on each soft X-ray data and labeled on Fig. 6.1 with a black dashed arrow, in correspondence with the designed window edge. This edge is used as a spatial reference to determine the information of the shock propagation distance. The spatial structure of the soft X-ray data showed a strong dependence on the type of gases used. The images were taken

from the shots of the helium gas mixture (90% helium, 10% neon) and the pure neon gas, respectively shown in Fig. 6.3 (a) and (b).

To get the spatial profiles of electron temperature and density along with the shock, the raw image data was sliced into multiple pieces along the spatial axis. The spectral analysis described above was then performed for each slice to extract the corresponding temperature and density. Each lineout was spatially averaged over 10 pixels which correspond to $\sim 37\mu$m on the target plane.

The above analysis was applied to two images from different gases as displayed on Fig. 6.3 (a) and (b) where the position of the shock fronts is indicated by the white dashed lines. The identification of the shock front came from the density profiles shown in Fig. 6.4 that will be discussed later.

The shock velocities are measured to be ~ 600km$/$s and ~ 450km$/$s respectively for the helium gas mixture and the neon shots. Due to the difference in velocities, the two displayed snapshots appeared at different timings for a given position along with the VSG window. The timing for the shock in the helium gas mixture is at 2ns and pure neon gas, it is 2.5ns. The helium shock at 2.5ns has passed the field of view of the VSG window and the neon shock at 2ns just started to appear from the bottom of the film, leaving most of it without signal. Though the timing of snapshots displayed in Fig. 6.3 (a) and (b) varied by 0.5ns, it is found from our data that for a single shock, the length of the precursor region changes by less than 20% from 2ns to 2.5ns.

Fig. 6.4(a) and (b) show the reconstructed shock structures respectively for the helium gas mixture (90% helium and 10% neon) and the pure neon gas shots. Shock propagation direction is from the left to the right on those plots. The red lines with dots represent the temperatures. In both cases, they span from ~ 60eV, the lowest measurable temperature, up to ~ 150eV, which is the peak electron temperature recorded at the shock front. Below 60eV, the signal smears into noise and is no longer discernable.

The blue lines with dots display the density profiles, where a dramatic drop is observed at the shock front for both cases. The horizontal axes of the two plots are of different scales due to the different scale of their precursor lengths. Errors in the measurements mostly come from the uncertainty in the background subtraction and the calibration of the spectrometer (VSG) which can be found in Ref [70].

Two vertical dashed lines on each plot specify the shock front position as well as the shock width. The shock width, defined by the length over which the densities drop from the peak value to the uncompressed value, was found to be $\sim$ 300μm for the helium gas mixture and $\sim$ 180μm for the pure neon gas. Given the exposure time of the framing camera of 400ps, the shocks could travel $\sim$ 240 in the helium gas mixture and $\sim$ 180μm in the pure neon gas. Therefore, the measured shock width is the maximum bound for the true shock width scale. Ahead of the shock front in the helium mixture case is a region characterized by high temperature and low density extending over $\sim$ 500μm. This is the precursor region with hot electrons and non-compressed material. However, no precursor is observed in the pure neon gas, where the signal vanishes within one resolvable step.

The different behavior of the shock precursors in the two gases explains some of the observations from the raw image data. On Fig. 6.3(b) for the pure neon, the shock front splits the data into two distinctive regions. Below the shock front (in the shocked region), a region of relatively higher X-ray emission intensities is observed while in the region above the shock front (the unshocked region), the flux of X-ray emission is significantly lower. Because shock fronts are characterized by sharp gradients of density, temperature, and pressure, the plasma conditions differ strongly between the post-shocked and pre-shocked area on each side of the shock front. In the post-shocked region, which corresponds to the bottom part of the image, the plasma exhibits large densities due to the shock compression and higher temperature due to shock heating, thereby yielding higher X-ray emission intensities. On the other hand, for the pre-shocked

region, the plasma is more tenuous and relatively colder, as shown by the lower flux of emitting X-rays observed from this region. However, it is more difficult to locate the shock front in the helium gas mixture (90% helium and 10% neon) due to the strong preheat ahead of the shock front. Instead of a sharp drop, the electrons maintained a temperature level above 100 eV, comparable to the shock front temperature, for a couple hundreds of microns ahead of the shock as shown in Fig. 6.4 (b). Therefore, on the two sides of the shock front, the change in terms of X-ray emission flux is not as dramatic as that observed in the neon shock.

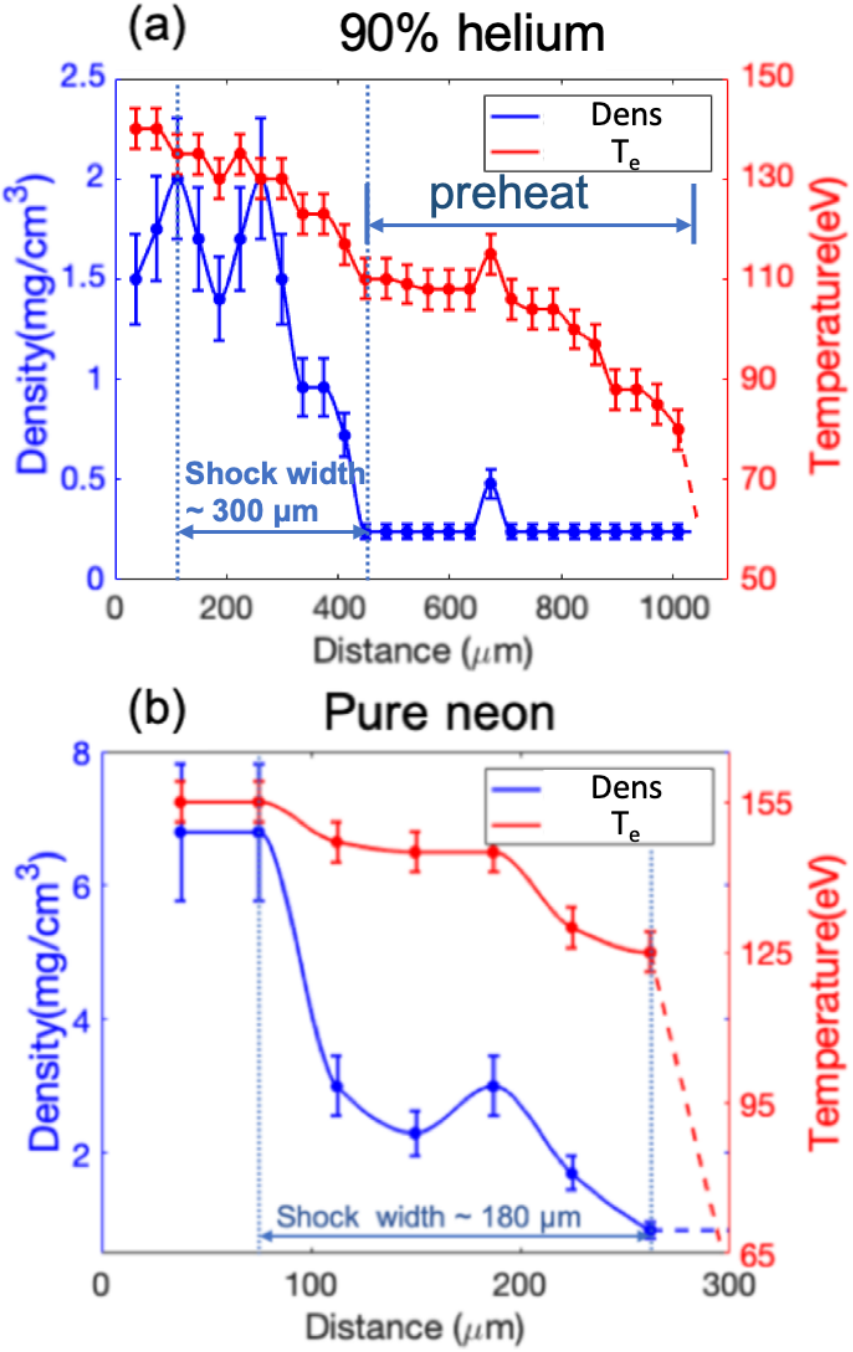

Figure 6.4: Spatial density and electron temperature profiles of the shocks travelling in (a) helium gas mixture composed of 90% helium, 10% neon and (b) pure neon gas. The shock widths are measured to be $\sim$ 300μm for the helium gas mixture and $\sim$ 180μm for the pure neon gas. The precursor distance for the helium gas mixture is $\sim$ 500μm. No precursor is measured in the pure neon gas.

6.3 Discussion and simulation

Table 6.1: Characteristic values about the shock and mean free paths among particles

characteristic length	value
$\lambda_{e,e}$	~ 1 μm
$\lambda_{he,e}$	~ 50 μm
$\lambda_{ne,e}$	~ 6 μm
$\lambda_{he,he}$	~ 100 μm
$\lambda_{ne,ne}$	~ 12 μm
shock width	≤ 180 μm
precursor width in neon	~ 30 μm
precursor width in helium	~ 500 μm

Discussion is provided in this section on the collisionality of electrons and ions and their behavior at a strong plasma shock front. Table. 6.1 lists some characteristic scale lengths of the shock, namely the shock width, the precursor length in both gas type, and the mean-free-path between multiple particles involved. Hereafter, we refer to the density jump front as the compression shock. All mean free paths are calculated by treating the particle in the shocked material as test particles and the un-shocked material as background. For example λ_{ee} means the mean free path of the hot electrons ($\sim$ 150eV) present in the un-shocked plasma.

For the formation of a collisional shock in a plasma, ions gain velocity from the pusher and eventually reach velocities on the same order of the shock. Then, collisions convert part of their kinetic velocity into thermal velocity on a time-scale defined by the ion-ion characteristic time τ_{ii}. Moreover, electrons of the background gain thermal energy from the collisions with the energetic ions on a time-scale defined by the ion-electron characteristic time τ_{ie}, which is larger than τ_{ii} by a factor of $\left(\frac{m_i}{m_e}\right)^{0.5}$. Therefore, at the fronts of the shocks studied here, electrons' motions are predominantly the thermal velocity, corresponding to $\sim$ 150eV, while for ions it is their streaming velocity, corresponding to 5keV for helium and $\sim$ 25keV for neon.

For each collision, ions only lose a moderate amount of their kinetic energy and several collisions are needed to significantly slow them down. The width of the compression shock is thus on the same order as a couple of ion-ion mean free paths, as shown by Table.6.1, which is consistent with the hydrodynamic theory.

Table. 6.1 also conveys the message that electrons are strongly collisional given their mean free path of ~ 1 μm, which is less than the shock widths by two orders of magnitude. However, ions, especially helium, reach a kinetic regime as a consequence of their mean-free-path being comparable to the scale of the shock. In light of those results, we performed both hydrodynamic and particle-in-cell (PIC) simulations to investigate the influence respectively from electron thermal conduction and ion kinetic effects on the formation of the observed precursors.

6.3.1 Radiation-Hydrodynamic simulation

A 1-D radiative-hydrodynamic simulation was performed to simulate the shock propagation, in which the Spitzer theory [96] was applied for the thermal conduction module. According to the classical formula[96, 97], the heat flow along one dimension x can be expressed by the following equation:

$$\begin{aligned} S &= \xi(Z)\frac{(k_B T_e)^{5/2} k_B}{m_e e^4 Z \ln\Lambda_{ei}}\frac{\partial T_e}{\partial x}, \\ &= \xi(Z) \times 1.93 \times 10^{-5}\frac{T_e^{5/2}}{Z\ln\Lambda_{ei}} \cdot \frac{\partial T_e}{\partial x}\left[\frac{erg}{cm^2\, s}\right], \end{aligned} \tag{6.1}$$

where T_e is the electron temperature, Z the ion charge status, $\ln\Lambda$ the Coulomb logarithm and $\xi(Z)$ is a number that depends only weakly on Z [82].

In addition to Z, the equation indicates the strong dependence of electron heat

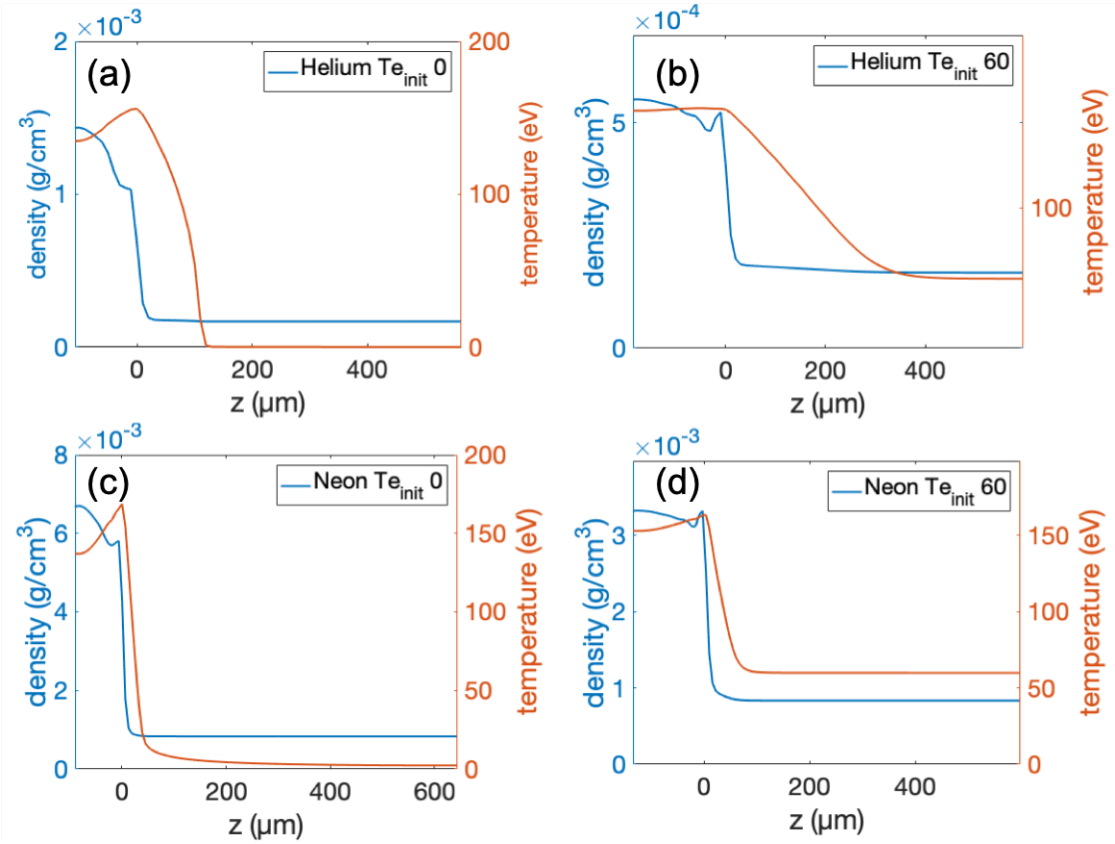

Figure 6.5: Simulated density and temperature profiles for helium and neon shocks with different initial electron temperature. Orange curves represent density, and blue curves represent temperature.

flow on the local temperature, as well as the temperature gradient. Therefore, to study properly the impact of electron thermal conduction on the precursor formation, the simulated electron temperature of the shock has to be matched with the experimental observation.

Shocks in the hydro simulation were initialized in one dimension by a hot moving plasma penetrating into a cold static one. The streaming velocity was adjusted between 300km/s and 400km/s, to make the simulated electron temperature of the shock comparable with the experimental measurement of $\sim$ 150eV. Here, pure helium gas was used to simulate the helium gas mixture (90% helium and 10% neon) since the code is limited on performing only a single fluid calculation. As the average atomic mass and

charge state for the 90% helium and 10% neon gas mixture are 5.6 and 2.8 assuming neon ions are fully stripped, pure helium is considered as a reasonable representation for the mixture. The pure neon gas shot was also simulated.

Because temperature below 60eV merge with the noise in the VSG, various initial temperatures ranging between room temperature ($\sim$ 0eV) and $\sim$ 60eV were tested in the simulation for helium and neon shocks. A systematic increase in the length of the precursor was observed when increasing the initial temperature. Fig. 6.5 columns (right) and (left) show the two cases for 60eV and 0eV, respectively. The timing of the profiles is the same as the timing of the experimental data. The blue curves in each plot represent the density profiles and the orange curves represent the temperature profiles. For easy comparison, the shock front positions were designated as the origin ($z = 0$) on all plots.

As shown by Fig. 6.5, the simulation results from the higher 60eV initial background electron temperatures give a better comparison to the experimental observations in terms of precursor length. Regardless of the initial electron temperature set, the simulation prediction for the length of the neon precursor is always less than 50μm, which well agrees with experimental data. The prediction for the helium shock shows a strong dependence on the initial electron temperature. From 0eV to 60eV, the simulation indicates a significant extension of the helium precursor length, from $\sim$ 100μm to $\sim$ 400μm.

The precursor length extension correlates with the heating of background electrons prior to the arrival of the compression shock. In a classical view of a plasma shock, the precursor length reaches to $\left(\frac{m_i}{m_e}\right)^{1/2} \lambda_{ii}$, which in the studied case, became comparable to the scale of the tube. Therefore, before the compression shock arrives, the background electrons in the un-shocked region are possibly heated up to temperatures much greater than the room temperature.

In addition to hydrodynamic simulations, 1D simulations using the particle-in-cell code OSIRIS [98] were also performed as the calculation of mean free paths presented in

the last section suggested kinetic ions at the shock front.

6.3.2 Kinetic aspects on the precursor preheating

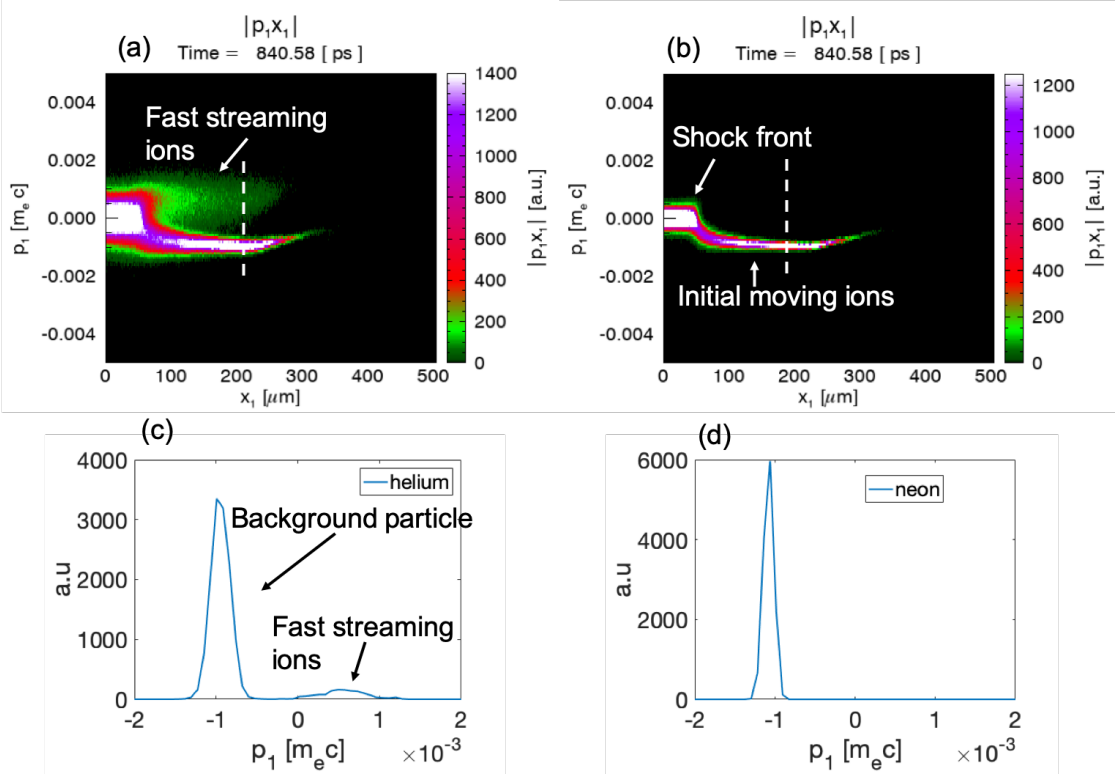

Figure 6.6: Phase plots from the particle-in-cell simulation for helium (a) and neon (b) shocks. For those two images, the horizontal axis represents the space along the shock propagation from left to the right and the vertical axis represents the particle momentum normalized by $m_e c$. (c) and (d) show ion particle distribution ahead of the shock at the position around $x_1 = 200\mu$m, which is indicated by the white dashed line.

To study the kinetic effect, the shock velocity rather than electron temperature is designated to match with that from the experimental measurement. PIC simulations with the OSIRIS code were run in 1D, and the shock geometry was created by initializing a thermal plasma with a drift velocity of 0.001c (300km/s) towards a perfectly reflecting wall, corresponding to a shock velocity 400km/s. The cell size is $0.143\,c/\omega_{pe}$, where ω_{pe} is the plasma frequency of the down-stream density, which roughly results in 0.09µm

for He/Ne and 0.05μm for Ne. The total length of the simulation box was dictated by the requirement that the edge of the drifting plasma does not reach the shock front before the end of the simulation, which for He/Ne was $800\,c/\omega_{pe}$, for Ne $1600\,c/\omega_{pe}$, and which in both cases correspond to about 600μm. Coulomb collisions were included using the Pérez collision model [99], with all possible species interactions included. The collision time step was set to 5 times the PIC time step, which was sufficient to resolve all the collisional timescales. In the cases shown here, the initial (upstream) electron and ion temperatures were about 15 eV, although multiple simulations were run and this parameter did not appear to have much of an effect.

Downstream, the electron temperature in the OSIRIS simulations was found to be ~ 400eV, higher than the experimental results. We believe this to be due to cooling via radiation effects (*e.g.* bremsstrahlung, bound-bound) which is not present in PIC, as well as overestimation due to the one-dimensional geometry. Therefore, we will not emphasize the quantitative comparison between experimental observation and simulation results, but rather focus on studying the underlying physics of the particle kinetic effects.

Phase plots of velocity versus space are shown for helium and neon shocks in Fig. 6.6 (a) and (b), respectively, taken after approximately 900ps. The horizontal axes of the plots display space along the shock propagation in μm. The fast particles were initially injected from the right and then were reflected by the wall set at location zero. Consequently, the formed shock is propagating to the right. The vertical axes represent the ion momentum normalized to $m_e c$. The fronts of the shocks are recognized by the sharp changes in ion velocity.

A group of fast streaming ions with a velocity nearly twice that of the shock is found ahead of the helium shock in the preheat region, which conversely is not observed in the neon shock. There are two hypotheses for the formation of the fast-moving ions. They could either be leaking from the compression shock region or reflected by the

shock front. Further investigations are ongoing to address in more details the origin of those fast-moving ions ahead of the shock front Being energetic, those fast-moving ions possibly transfer energy into background electrons by thermal equilibration processes, hence probably contributing to lengthening and heating up of the precursor in the helium gas.

Fig. 6.6(c) and (d) provide the ion particle distributions ahead of the shocks in the preheat regions for the helium and neon gases, respectively. (c) indicates that the number of the fast streaming ions is around 5% compared to that of the background ions in the unshocked helium gas. And the relative velocity is $\sim 500\mathrm{km/s}$, corresponding to a kinetic energy of $\sim 5\mathrm{keV}$. Being stopped by the background ion and electron particles, the fast streaming ions deposit their energy into the preheat region via collisions between ion-ion and ion-electron. Given the information above, that energy could be able to raise the background temperature by $\sim 250\mathrm{eV}$ in the precursor region.

6.4 Conclusion

In summary, we have successfully measured the electron temperature and density profiles of plasma shocks including the entire precursor region both in a pure neon gas and a helium gas mixture by a 1-D resolved soft x-ray spectrometer. The upper limits of the shock widths are measured to be on the order 300μm in the helium gas mixture and 180μm in the pure neon gas. A preheat region extending to more than $\sim 500\mu\mathrm{m}$ ahead of the shock front is observed in the helium gas mixture, while the precursor length of the shock in the pure neon gas is not observed. Investigation for the formation of precursor both by hydrodynamic simulation and particle-in-cell simulations were performed. These simulations provided two major observations. Hydrodynamically, the heat flow inversely depends on the charge state Z of the plasma, which was ~ 2 for the helium gas mixture

and ~ 9 for neon. Therefore, stronger heat flow was present in the shock propagating in the helium gas mixture. Good agreements have been achieved between the experimental measurements and the results from hydro simulations. The precursor length for the helium mixture gas has been seen to be strongly dependent on the preheating of the background electrons ahead of the shock. From the kinetic point of view, preliminary PIC simulations show a group of fast streaming ions that only appears in the helium gas mixture and might play a role in the formation of the long precursor in the helium shock via pre-heating.

Chapter 6, in full, is currently being prepared for publication as R. Hua J. May, M. Sherlock, M. Bailly-Grandvaux, M. Dozieres, F.N. Beg, C. McGuffey, W. Mori, and Y. Ping "Precursor structures of strong plasma shocks in helium and neon gases". The dissertation author was the primary investigator and author of the paper.

Chapter 7

Summary and Future Work

7.1 Summary

In summary, a novel platform is developed on the OMEGA-EP facility to study the shock front structure as well as the associated electric and magnetic field. Strong plasma shocks were generated by the laser ablation of a piece of plastic or glass foil. It then propagated into a cylindrical tube along the central axis. The tube was typically filled with neon or helium gases. The shock traveling along the central axis of a cylindrical tube can be approximated by a one dimension problem. In comparison to the convergent shocks in implosion experiments, this configuration provides more highly resolved observation of the shock front. A Variable line spacing soft-Xray spectrometer was employed to record the self-emitted x-ray light from the compressed shock front. The side-on proton radiography was used to detect the field structure at the shock front. Differentiating the electric field and the magnetic field associated with a strong shock is achieved using the method of multi-angle proton probing.

In chapter. 3, a detailed description of the configuration of the platform as well

as the structures of both the gas target and proton target are presented. The working principles of the two primary diagnostics, proton Radiography and soft X-ray spectrometer, as well as the analysis process of their data, are discussed in detail. Variable shock strength can be achieved by either varying the driver lasers' energy or changing the ablator material and thickness. The utilization of proton radiography enables the study of the electric and magnetic fields at the shock front. The generation of TNSA protons allows the radiography for the shock-fronts at different proton energies, thus providing energy-dependent information. Also, the timing of sending probing protons can be controlled by adjusting the delay between the long pulse and short pulse lasers, which enables the radiography for the shock front at different times during its propagation. Varying the shock strength and gas-fill allows us to study the underlying physics of plasma shock condition at different Z and T_e.

In chapter. 4, a strong self-generated electric field at a 0.5 Mbar shock front created in a low-density system has been studied both experimentally and theoretically. Experiments were conducted using three long-pulse laser beams with a total energy of 6.4 kJ in 2 ns for shock generation and an 850 J, 10 ps short-pulse laser to produce broadband protons for radiography. The shock front position was measured from the spatial fiducial attached to the gas target. By comparing the location of the shock front and proton source location, it was found that the incident angle of the protons from their source to the shock front was approximately normal. Evidence of the existence of an electric field at the shock front was observed. Observations of the deflection pattern of probing protons show the self-generated electric fields with the electric potential on the order of 300 V. Additionally, 2-Radiation hydro simulations using FLASH have been conducted, a strong shock comparable to the experimental observation was successfully generated using the identical laser drivers and the same target setup. The electric field inferred from the electron pressure profile from the simulation results is also favorably

comparable with the experimental results. Analytical and particle tracking methods support the observation of the electric field of 300 V potential.

In chapter 5, the design of the gas target has been improved from the one presented in chapter 4 by replacing the ablator from a piece of 50 μm plastic with a 2 μm glass. Stronger shock, whose speed reach to twice compared to the one presented in chapter 4, was achieved with even less laser energy. Initially, the proton source was placed behind the shock front by a distance of $\sim$ 800 μm. A significant strong proton signal was observed from the radiography, which corresponds to an electric field of $\sim$ 6 KeV. With the increase of two times in velocity, this vast increase in electric potential $\sim 20\times$ is unexplainable regardlessly.

The aberration in the experimental observation makes us realize the existence of a magnetic field in addition to the electric field. Motivated by the desire to recognize the type of field at the shock front, a new design of placing the proton source ahead of the shock front was developed. The basic idea comes from the fact that the deflection of a charged particle by the magnetic field has a dependence on the incident angle while the deflection by the electric field has no such dependence. Therefore, if the electric field dominates at the shock front, the proton radiography data should show consistency whether the probing protons were sent along or against the shock front. Otherwise, if the magnetic field dominates at the shock front, the proton radiography data should vary and show dependence on the proton incident angles.

The deflection pattern recorded by the radiography turned to be contrary when placing the proton source at different locations. From the information, we confirmed the domination of the magnetic field at the shock front. The simultaneous existence of the electric field is also realized and can be probed by the normal incident protons as described in chapter 4.

Quantitative analysis on the spatial profile of the magnetic field, including its

thickness, peak intensity as well as spatial variation, has been performed using a 3-D particle tracking program. Consistent results have been drawn from the analyses for data from both proton source locations. Further investigation for the magnetic field generation by particle-in-cell simulation was performed using LSP with an implicit, hybrid method. The self-generation of the strong magnetic field at the shock front is attributed to the Biermann Battery effect. As the ablator is 1.9 mm diameter, the central part 750 μm of which pushed into the gas with extremely high velocity by laser ablation. The density evolution, determined by advection and the temperature evolution, determined by thermal diffusion, obey different physical processes and therefore eventually evolve into different spatial distributions during the shock propagation. The unparallel components in the gradients of density and temperature give rise to the growth of a magnetic field.

In chapter 6, the one dimension resolved soft-X-ray data is present and analyzed both in a gas mixture composed of 90% helium and 10%*neon* and pure neon gas. The electron temperature and density profiles of plasma shocks have been successfully measured using the collisional-atomic program PRISMSPECT by the forward-fitting method. The shock width in both gases was measured to be on the order of 180 μm. Besides, the entire precursor region, where the electron temperature is far over ion temperature, is observed both in a helium dominated gas mixture and pure neon gas. It is found this preheat region extends to more than $\sim$ 500μm in the helium shock and less than $\sim$ 30μm in the neon shock. At the shock front, the electrons are found to be strongly collisional with their mean-free-path two orders less than the characteristic length of the shock. The radiation-hydrodynamic simulation is performed to investigate the impact of thermal conduction on the formation of the precursors. PIC simulation is also performed since the ion movement falls in the kinetic region. The results indicate that hydrodynamically, the dependence of heat flow on the charge state Z plays a role in the formations of precursors in the two gases. Kinetically, there is a group of fast streaming ions ahead of the

shock existing only in the helium gas mixture, which also potentially contributes to the formation of a more extended precursor layer in the helium shock. Further investigation of the formation of the fast streaming ions is still in progress.

7.2 Future work

7.2.1 Double ring data

Another interesting Radiography data acquired from this platform displays a double ring structure at the shock front as shown by Fig. 7.1(a). The gas-filled in this shot was 90% helium and 10% neon. The shock was initiated by the laser ablation of 2μm SiO_2 foil on the left side of the tube. The laser was delivered with 1 kJ energy in 0.5 ns. This snapshot was taken 3 ns after the shock initiation.

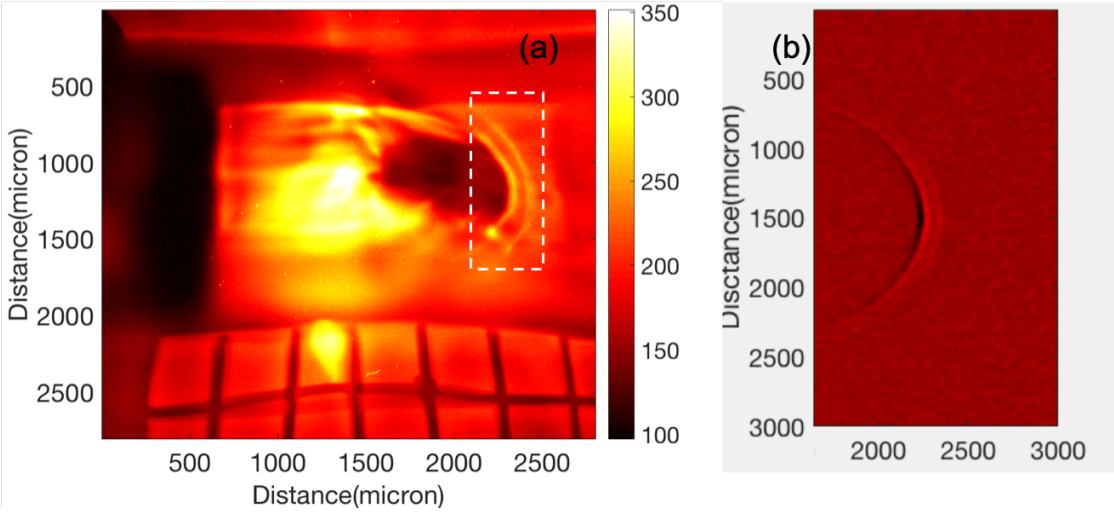

Figure 7.1: (a) Radiography image for a shot of 10% neon and 90 %helium. A double ring structure is observed at the shock front. (b) the simulated double ring radiography image.

Different from the radiography of pure helium shock, the double ring structure at the shock front indicates a more complex magnetic and electric field structure at the

shock front. As predicted by the FLASH simulation, the electron temperature at the shock front is similar to that of the pure helium shock. The electric field which is generated due to the gradient along the pressure profile is not significant from that of the pure helium shock, $\sim$ 300V in terms of potential. Therefore, the magnetic field structure must vary to produce such a double-ring proton signal at the shock front.

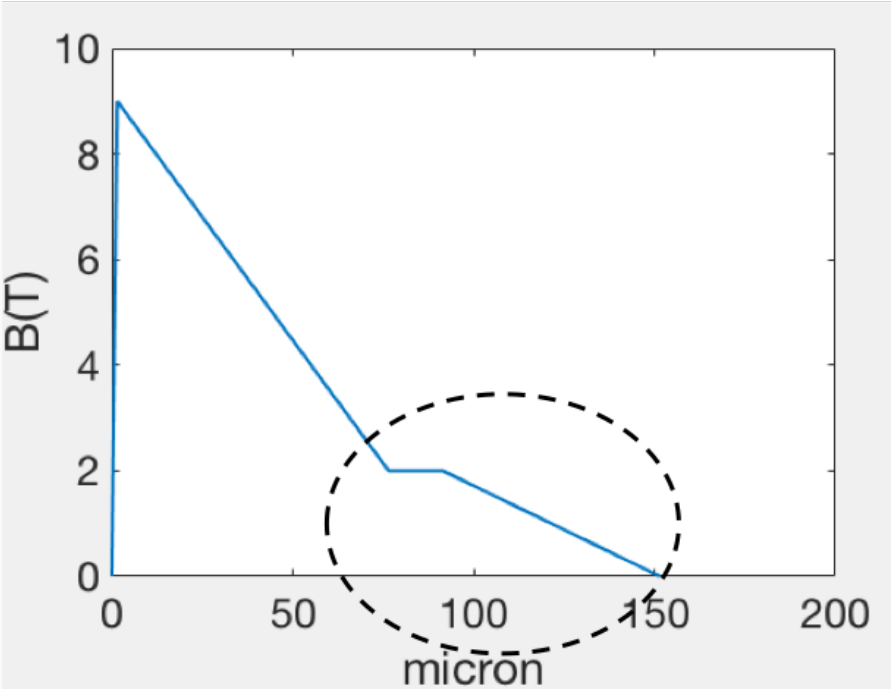

Figure 7.2: Magnetic field spatial profile at the shock front that could produce the double ring proton signal.

A potential field profile is displayed by Fig. 7.2. Rather than a simple triangular shape, an additional structure as labeled by the circle is attached. The preliminary hypothesis for the generation of such a magnetic field structure involves species separation between the neon and helium at the shock front. Further investigation both on the deeper insight of the radiography data as well as simulation from a particle in cell code is in progress.

7.2.2 Proposal to NIF

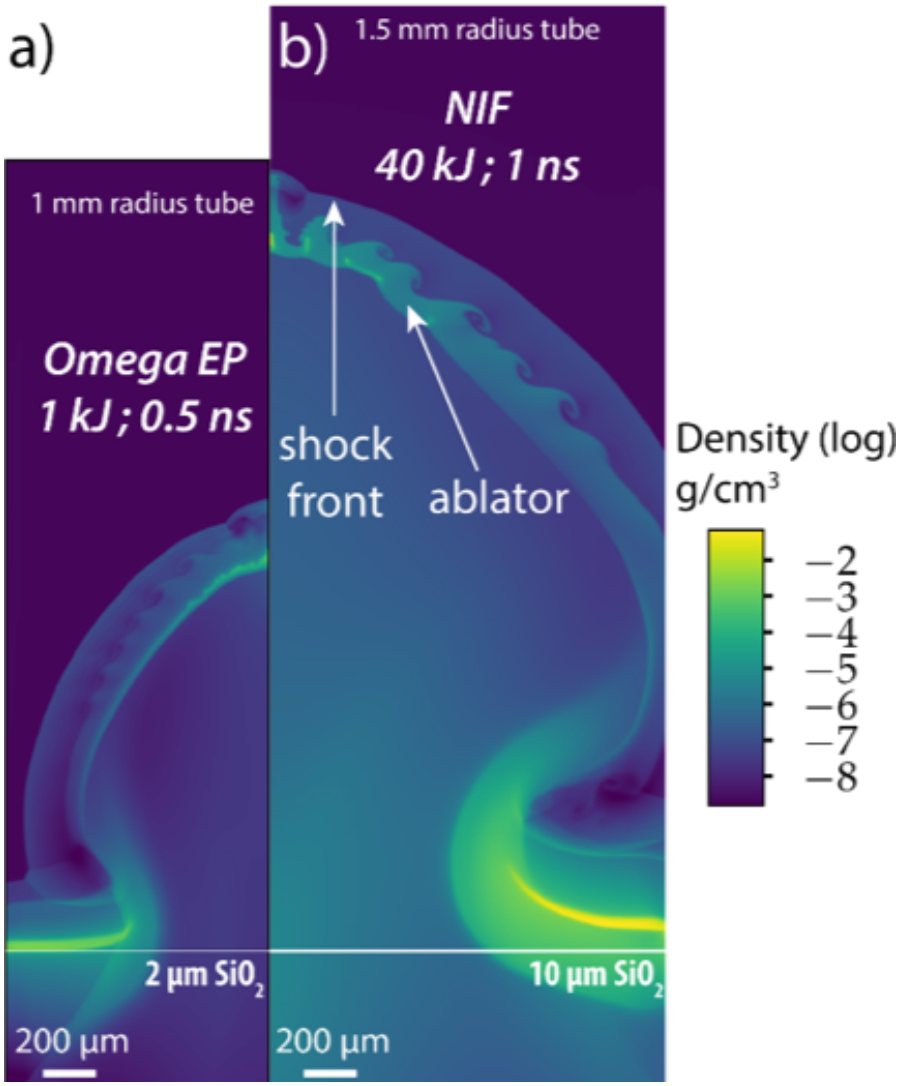

Figure 7.3: (a) is the results using the identical condition that was used on OMEGA EP, 1 kJ, 0.5ns, and 750µm focal spot. (b) shows the simulation result from FLASH using 80 kJ in 2ns and 2000 m focal spot, which is only possible on NIF.

We have proposed to the national ignition facility (NIF) with our platform to study the electric and magnetic fields associated with much stronger shocks. simulations using FLASH code with NIF laser parameters are carried out and the results have been compared with that from OMEGA EP laser as shown by Fig 7.3. On NIF, the shock is expected to be initiated from 6 quads driver beams using 80 kJ, 2ns, and the standard

phase plate. The significant separation between the shock front and the gas-ablator interface is predicted. In contrast, the EP long pulse laser can only drive the shock slightly in front of the gas-ablator interface (on the order of 100 um), while NIF scale laser increases that separation significantly to mm scale. Six quads of the NIF laser will generate a stronger shock, with Mach number more than 10, pressure on the order of 3 Mbar, speed up to 1000 km/s and temperature 1 keV which about four times larger compared to OMEGA EP for the same ablator. These simulations demonstrate that NIF is capable of providing stronger shocks far beyond what can be reached on OMEGA EP.

Bibliography

[1] Wikipedia contributors. *Binding energy — Wikipedia, The Free Encyclopedia*. [Online; accessed 9-May-2019]. 2019. URL: https://en.wikipedia.org/w/index.php?title=Binding_energy&oldid=888867198.

[2] S. Atzeni, J. Meyer-Ter-Vehn, and J. Meyer-ter Vehn. *The Physics of Inertial Fusion*. Vol. 125. Clarendon Press, Oxford, 2004, 2004.

[3] S. Haan, J. Lindl, D. Callahan, D. Clark, J. Salmonson, B. Hammel, L. Atherton, R. Cook, M. Edwards, and S Glenzer. "Point design targets, specifications, and requirements for the 2010 ignition campaign on the National Ignition Facility". In: *Physics of Plasmas* 18.5 (2011), p. 051001.

[4] Wikipedia contributors. *Inertial confinement fusion — Wikipedia, The Free Encyclopedia*. [Online; accessed 27-March-2019]. 2019. URL: https://en.wikipedia.org/w/index.php?title=Inertial_confinement_fusion&oldid=887662318.

[5] M. Y. Jaffrin and R. F. Probstein. "Structure of a plasma shock wave". In: *The Physics of Fluids* 7.10 (1964), pp. 1658–1674.

[6] G Gregori, B Reville, and F. Miniati. "The generation and amplification of intergalactic magnetic fields in analogue laboratory experiments with high power lasers". In: *Physics Reports* 601 (2015), pp. 1–34.

[7] J. Meinecke, H. Doyle, F. Miniati, A. Bell, R Bingham, R Crowston, R. Drake, M. Fatenejad, M. Koenig, and Y. Kuramitsu. "Turbulent amplification of magnetic fields in laboratory laser-produced shock waves". In: *Nature Physics* 10.7 (2014), p. 520.

[8] R Betti, C. Zhou, K. Anderson, L. Perkins, W Theobald, and A. Solodov. "Shock ignition of thermonuclear fuel with high areal density". In: *Physical Review Letters* 98.15 (2007), p. 155001.

[9] H. Herrmann, J. Langenbrunner, J. Mack, J. Cooley, D. Wilson, S. Evans, T. Sedillo, G. Kyrala, S. Caldwell, and C. Young. "Anomalous yield reduction in direct-drive deuterium/tritium implosions due to H 3 e addition". In: *Physics of Plasmas* 16.5 (2009), p. 056312.

[10] H. G. Rinderknecht, M. Rosenberg, C. Li, N. Hoffman, G Kagan, A. Zylstra, H Sio, J. Frenje, M. G. Johnson, and F. Séguin. "Ion thermal decoupling and species separation in shock-driven implosions". In: *Physical Review Letters* 114.2 (2015), p. 025001.

[11] M. Rosenberg, H. Rinderknecht, N. Hoffman, P. Amendt, S Atzeni, A. Zylstra, C. Li, F. Séguin, H Sio, and M. G. Johnson. "Exploration of the transition from the hydrodynamiclike to the strongly kinetic regime in shock-driven implosions". In: *Physical Review Letters* 112.18 (2014), p. 185001.

[12] B. D. Keenan, A. N. Simakov, L. Chacón, and W. T. Taitano. "Deciphering the kinetic structure of multi-ion plasma shocks". In: *Physical Review E* 96.5 (2017), p. 053203.

[13] M. Casanova, O. Larroche, and J.-P. Matte. "Kinetic simulation of a collisional shock wave in a plasma". In: *Physical Review Letters* 67.16 (1991), p. 2143.

[14] F Vidal, J. Matte, M Casanova, and O Larroche. "Ion kinetic simulations of the formation and propagation of a planar collisional shock wave in a plasma". In: *Physics of Fluids B: Plasma Physics* 5.9 (1993), pp. 3182–3190.

[15] C Bellei, H Rinderknecht, A Zylstra, M Rosenberg, H Sio, C. Li, R Petrasso, S. Wilks, and P. Amendt. "Species separation and kinetic effects in collisional plasma shocks". In: *Physics of Plasmas* 21.5 (2014), p. 056310.

[16] H. Yemin and H. Xiwei. "The properties and structure of a plasma non-neutral shock". In: *Physics of Plasmas* 10.7 (2003), pp. 2704–2711.

[17] P. Amendt, O. Landen, H. Robey, C. Li, and R. Petrasso. "Plasma barodiffusion in inertial-confinement-fusion implosions: Application to observed yield anomalies in thermonuclear fuel mixtures". In: *Physical Review Letters* 105.11 (2010), p. 115005.

[18] G. Kagan and X.-Z. Tang. "Electro-diffusion in a plasma with two ion species". In: *Physics of Plasmas* 19.8 (2012), p. 082709.

[19] K. Molvig, N. M. Hoffman, B. Albright, E. M. Nelson, and R. B. Webster. "Knudsen layer reduction of fusion reactivity". In: *Physical review letters* 109.9 (2012), p. 095001.

[20] J. R. Rygg, J. Frenje, C. Li, F. Séguin, R. Petrasso, J. Delettrez, V. Y. Glebov, V. Goncharov, D. Meyerhofer, and S. Regan. "Tests of the hydrodynamic equivalence of direct-drive implosions with different D 2 and He 3 mixtures". In: *Physics of plasmas* 13.5 (2006), p. 052702.

[21] H. Rinderknecht, H Sio, C. Li, A. Zylstra, M. Rosenberg, P Amendt, J Delettrez, C Bellei, J. Frenje, and M. G. Johnson. "First observations of nonhydrodynamic mix at the fuel-shell interface in shock-driven inertial confinement implosions". In: *Physical review letters* 112.13 (2014), p. 135001.

[22] D. Casey, J. Frenje, M. G. Johnson, M.-E. Manuel, H. Rinderknecht, N Sinenian, F. Séguin, C. Li, R. Petrasso, and P. Radha. "Evidence for stratification of deuterium-tritium fuel in inertial confinement fusion implosions". In: *Physical review letters* 108.7 (2012), p. 075002.

[23] C. Li, F. Séguin, J. Rygg, J. Frenje, M Manuel, R. Petrasso, R Betti, J Delettrez, J. Knauer, and F Marshall. "Monoenergetic-proton-radiography measurements of implosion dynamics in direct-drive inertial-confinement fusion". In: *Physical Review Letters* 100.22 (2008), p. 225001.

[24] T. Morita, N. Kugland, W Wan, R. Crowston, R. Drake, F. Fiúza, G. Gregori, C Huntington, T. Ishikawa, and M. Koenig. "Proton imaging of an electrostatic field structure formed in laser-produced counter-streaming plasmas". In: *Journal of Physics: Conference Series*. Vol. 688. 1. IOP Publishing. 2016, p. 012071.

[25] H.-S. Park, C. Huntington, F Fiuza, R. Drake, D. Froula, G Gregori, M Koenig, N. Kugland, C. Kuranz, and D. Lamb. "Collisionless shock experiments with lasers and observation of Weibel instabilities". In: *Physics of Plasmas* 22.5 (2015), p. 056311.

[26] J. Rygg, F. Séguin, C. Li, J. Frenje, M.-E. Manuel, R. Petrasso, R Betti, J. Delettrez, O. Gotchev, and J. Knauer. "Proton radiography of inertial fusion implosions". In: *Science* 319.5867 (2008), pp. 1223–1225.

[27] R Hua, H Sio, S. Wilks, F. Beg, C McGuffey, M Bailly-Grandvaux, G. Collins, and Y Ping. "Study of self-generated fields in strongly-shocked, low-density systems using broadband proton radiography". In: *Applied Physics Letters* 111.3 (2017), p. 034102.

[28] N. M. Hoffman, G. B. Zimmerman, K. Molvig, H. G. Rinderknecht, M. J. Rosenberg, B. Albright, A. N. Simakov, H. Sio, A. B. Zylstra, and M. Gatu Johnson. "Approximate models for the ion-kinetic regime in inertial-confinement-fusion capsule implosions". In: *Physics of Plasmas* 22.5 (2015), p. 052707.

[29] D. R. Welch, D. V. Rose, R. E. Clark, T. C. Genoni, and T. Hughes. "Implementation of an non-iterative implicit electromagnetic field solver for dense plasma simulation". In: *Computer physics communications* 164.1-3 (2004), pp. 183–188.

[30] O Larroche. "Kinetic simulations of fuel ion transport in ICF target implosions". In: *The European Physical Journal D-Atomic, Molecular, Optical and Plasma Physics* 27.2 (2003), pp. 131–146.

[31] C Bellei, P. Amendt, S. Wilks, M. Haines, D. Casey, C. Li, R Petrasso, and D. Welch. “Species separation in inertial confinement fusion fuels”. In: *Physics of Plasmas* 20.1 (2013), p. 012701.

[32] A. Inglebert, B. Canaud, and O. Larroche. “Species separation and modification of neutron diagnostics in inertial-confinement fusion”. In: *EPL (Europhysics Letters)* 107.6 (2014), p. 65003.

[33] I. Smirnovskii. “Influence of kinetic effects on the structure of an ion shock wave in a plasma”. In: *Plasma Physics Reports* 26.3 (2000), pp. 225–230.

[34] A. Velikovich, K. Whitney, and J. Thornhill. “A role for electron viscosity in plasma shock heating”. In: *Physics of Plasmas* 8.10 (2001), pp. 4524–4533.

[35] C. Graziani, P. Tzeferacos, D. Lee, D. Q. Lamb, K. Weide, M. Fatenejad, and J. Miller. “The biermann catastrophe in numerical magnetohydrodynamics”. In: *The Astrophysical Journal* 802.1 (2015), p. 43.

[36] A Ravasio, L Romagnani, S Le Pape, A Benuzzi-Mounaix, C Cecchetti, D Batani, T Boehly, M Borghesi, R Dezulian, and L Gremillet. “Proton radiography of a shock-compressed target”. In: *Physical Review E* 82.1 (2010), p. 016407.

[37] L Romagnani, S. Bulanov, M Borghesi, P Audebert, J. Gauthier, K Löwenbrück, A. Mackinnon, P Patel, G Pretzler, and T Toncian. “Observation of collisionless shocks in laser-plasma experiments”. In: *Physical review letters* 101.2 (2008), p. 025004.

[38] A. Mackinnon, P. Patel, M Borghesi, R. Clarke, R. Freeman, H Habara, S. Hatchett, D Hey, D. Hicks, and S Kar. “Proton radiography of a laser-driven implosion”. In: *Physical review letters* 97.4 (2006), p. 045001.

[39] B. Fryxell, K. Olson, P. Ricker, F. Timmes, M. Zingale, D. Lamb, P. MacNeice, R. Rosner, J. Truran, and H Tufo. “FLASH: An adaptive mesh hydrodynamics code for modeling astrophysical thermonuclear flashes”. In: *The Astrophysical Journal Supplement Series* 131.1 (2000), p. 273.

[40] J. Macfarlane, I. Golovkin, P. Woodruff, and P. Wang. “PrismSPECT and SPECT3D Tools for Simulating X-ray, UV, and Visible Spectra for Laboratory and Astrophysical Plasmas”. In: *APS Division of Atomic, Molecular and Optical Physics Meeting Abstracts*. 2003.

[41] I. Langmuir. “Oscillations in ionized gases”. In: *Proceedings of the National Academy of Sciences of the United States of America* 14.8 (1928), p. 627.

[42] S. I. Anisimov, A. Prokhorov, and V. E. Fortov. “Application of high-power lasers to study matter at ultrahigh pressures”. In: *Soviet Physics Uspekhi* 27.3 (1984), p. 181.

[43] E. M. Campbell and W. J. Hogan. “The National Ignition Facility-applications for inertial fusion energy and high-energy-density science”. In: *Plasma Physics and Controlled Fusion* 41.12B (1999), B39.

[44] J. Lindl. “Development of the indirect-drive approach to inertial confinement fusion and the target physics basis for ignition and gain”. In: *Physics of plasmas* 2.11 (1995), pp. 3933–4024.

[45] W. Hogan, E. I. Moses, B. Warner, M. Sorem, and J. Soures. “The national ignition facility”. In: *Nuclear Fusion* 41.5 (2001), p. 567.

[46] B. A. Remington, D. Arnett, R Paul, and H. Takabe. “Modeling astrophysical phenomena in the laboratory with intense lasers”. In: *Science* 284.5419 (1999), pp. 1488–1493.

[47] B. A. Remington, R. P. Drake, H. Takabe, and D. Arnett. “A review of astrophysics experiments on intense lasers”. In: *Physics of Plasmas* 7.5 (2000), pp. 1641–1652.

[48] I. E. Turcu and J. B. Dance. “X-rays from laser plasmas: generation and applications”. In: *X-Rays From Laser Plasmas: Generation and Applications, by ICE Turcu, JB Dance, pp. 330. ISBN 0-471-98397-7. Wiley-VCH, November 1998.* (1998), p. 330.

[49] G. A. Mourou, C. Barty, and M. D. Perry. *Ultrahigh-intensity laser: physics of the extreme on a tabletop*. Tech. rep. Lawrence Livermore National Lab., CA (United States), 1997.

[50] T. Ditmire, J Zweiback, V. Yanovsky, T. Cowan, G Hays, and K. Wharton. “Nuclear fusion from explosions of femtosecond laser-heated deuterium clusters”. In: *Nature* 398.6727 (1999), p. 489.

[51] N. Bloembergen. “From nanosecond to femtosecond science”. In: *More Things in Heaven and Earth*. Springer, 1999, pp. 474–481.

[52] M. G. Baring and E. J. Summerlin. “Electrostatic Potentials in Supernova Remnant Shocks”. In: *High Energy Density Laboratory Astrophysics*. Springer, 2006, pp. 165–168.

[53] M. S. Grewal. “Limiting Mach number of an embedded ion shock”. In: *The Physics of Fluids* 16.4 (1973), pp. 561–562.

[54] B. D. Keenan, A. N. Simakov, W. T. Taitano, and L. Chacón. "Ion species stratification within strong shocks in two-ion plasmas". In: *Physics of Plasmas* 25.3 (2018), p. 032103.

[55] A Schlüter. "Über den Ursprung der Magnetfelder auf Sternen und im interstellaren Raum". In: *Zeitschrift für Naturforschung A* 5.2 (1950), pp. 65–71.

[56] R. M. Kulsrud and E. G. Zweibel. "On the origin of cosmic magnetic fields". In: *Reports on Progress in Physics* 71.4 (2008), p. 046901.

[57] P. Tzeferacos, M. Fatenejad, N. Flocke, C. Graziani, G Gregori, D. Lamb, D Lee, J Meinecke, A Scopatz, and K Weide. "FLASH MHD simulations of experiments that study shock-generated magnetic fields". In: *High Energy Density Physics* 17 (2015), pp. 24–31.

[58] H Sio, R Hua, Y Ping, C McGuffey, F Beg, R Heeter, C. Li, R. Petrasso, and G. Collins. "A broadband proton backlighting platform to probe shock propagation in low-density systems". In: *Review of Scientific Instruments* 88.1 (2017), p. 013503.

[59] Wikipedia contributors. *CR-39 — Wikipedia, The Free Encyclopedia*. [Online; accessed 28-May-2019]. 2019. URL: https://en.wikipedia.org/w/index.php?title=CR-39&oldid=892280135.

[60] R. Snavely, M. Key, S. Hatchett, T. Cowan, M. Roth, T. Phillips, M. Stoyer, E. Henry, T. Sangster, and M. Singh. "Intense high-energy proton beams from petawatt-laser irradiation of solids". In: *Physical review letters* 85.14 (2000), p. 2945.

[61] P. Patel, A. Mackinnon, M. Key, T. Cowan, M. Foord, M Allen, D. Price, H Ruhl, P. Springer, and R Stephens. "Isochoric heating of solid-density matter with an ultrafast proton beam". In: *Physical review letters* 91.12 (2003), p. 125004.

[62] S. Wilks, A. Langdon, T. Cowan, M Roth, M Singh, S Hatchett, M. Key, D Pennington, A MacKinnon, and R. Snavely. "Energetic proton generation in ultra-intense laser–solid interactions". In: *Physics of plasmas* 8.2 (2001), pp. 542–549.

[63] P. Mora. "Plasma expansion into a vacuum". In: *Physical Review Letters* 90.18 (2003), p. 185002.

[64] S. P. Hatchett, C. G. Brown, T. E. Cowan, E. A. Henry, J. S. Johnson, M. H. Key, J. A. Koch, A. B. Langdon, B. F. Lasinski, and R. W. Lee. "Electron, photon, and ion beams from the relativistic interaction of Petawatt laser pulses with solid targets". In: *Physics of Plasmas* 7.5 (2000), pp. 2076–2082.

[65] D. J. Kirby. "Radiation dosimetry of conventional and laser-driven particle beams". PhD thesis. University of Birmingham, 2011.

[66] P. Bolton, M Borghesi, C Brenner, D. Carroll, C De Martinis, F Fiorini, A Flacco, V Floquet, J Fuchs, and P. Gallegos. “Instrumentation for diagnostics and control of laser-accelerated proton (ion) beams”. In: *Physica Medica* 30.3 (2014), pp. 255–270.

[67] M. Bailly-Grandvaux. “Laser-driven strong magnetic fields and high discharge currents: measurements and applications to charged particle transport”. PhD thesis. Université de Bordeaux, 2017.

[68] S. Chen, M Gauthier, M Bazalova-Carter, S Bolanos, S Glenzer, R Riquier, G Revet, P Antici, A Morabito, and A Propp. “Absolute dosimetric characterization of Gafchromic EBT3 and HDv2 films using commercial flat-bed scanners and evaluation of the scanner response function variability”. In: *Review of Scientific Instruments* 87.7 (2016), p. 073301.

[69] K. Cone, J Dunn, M. Schneider, H. Baldis, G. Brown, J Emig, D. James, M. May, J Park, and R Shepherd. “Development of a time-resolved soft x-ray spectrometer for laser produced plasma experiments”. In: *Review of Scientific Instruments* 81.10 (2010), 10E318.

[70] J Park, G. Brown, M. Schneider, H. Baldis, P Beiersdorfer, K. Cone, R. Kelley, C. Kilbourne, E. Magee, and M. May. “Calibration of a flat field soft x-ray grating spectrometer for laser produced plasmas”. In: *Review of Scientific Instruments* 81.10 (2010), 10E319.

[71] T. Boehly, D. Brown, R. Craxton, R. Keck, J. Knauer, J. Kelly, T. Kessler, S. Kumpan, S. Loucks, and S. Letzring. “Initial performance results of the OMEGA laser system”. In: *Optics communications* 133.1-6 (1997), pp. 495–506.

[72] T. Kita, T. Harada, N Nakano, and H. Kuroda. “Mechanically ruled aberration-corrected concave gratings for a flat-field grazing-incidence spectrograph”. In: *Applied optics* 22.4 (1983), pp. 512–513.

[73] P. Amendt, J. Milovich, S. Wilks, C. Li, R. Petrasso, and F. Séguin. “Electric field and ionization-gradient effects on inertial-confinement-fusion implosions”. In: *Plasma Physics and Controlled Fusion* 51.12 (2009), p. 124048.

[74] L. Waxer, D. Maywar, J. Kelly, T. Kessler, B. Kruschwitz, S. Loucks, R. McCrory, D. Meyerhofer, S. Morse, and C Stoeckl. “High-energy petawatt capability for the OMEGA laser”. In: *Optics and photonics news* 16.7 (2005), pp. 30–36.

[75] C Stoeckl, J. Delettrez, J. Kelly, T. Kessler, B. Kruschwitz, S. Loucks, R. McCrory, D. Meyerhofer, D. Maywar, and S. Morse. “High-energy petawatt project at the University of Rochester’s Laboratory for Laser Energetics”. In: *Fusion science and technology* 49.3 (2006), pp. 367–373.

[76] M Borghesi, A Schiavi, D. Campbell, M. Haines, O Willi, A. MacKinnon, L. Gizzi, M Galimberti, R. Clarke, and H Ruhl. "Proton imaging: a diagnostic for inertial confinement fusion/fast ignitor studies". In: *Plasma physics and controlled fusion* 43.12A (2001), A267.

[77] A. Mack, G. Mack, D. Weltz, S. G. Scheib, H. D. Böttcher, and V. Seifert. "High precision film dosimetry with GAFCHROMIC® films for quality assurance especially when using small fields". In: *Medical physics* 30.9 (2003), pp. 2399–2409.

[78] A. Zylstra, C. Li, H. Rinderknecht, F. Séguin, R. Petrasso, C Stoeckl, D. Meyerhofer, P Nilson, T. Sangster, and S Le Pape. "Using high-intensity laser-generated energetic protons to radiograph directly driven implosions". In: *Review of scientific instruments* 83.1 (2012), p. 013511.

[79] V. L. Highland. "Some practical remarks on multiple scattering". In: *Nuclear Instruments and Methods* 129.2 (1975), pp. 497–499.

[80] N. Kugland, D. Ryutov, C Plechaty, J. Ross, and H.-S. Park. "Invited Article: Relation between electric and magnetic field structures and their proton-beam images". In: *Review of scientific instruments* 83.10 (2012), p. 101301.

[81] A. Macchi, M. Borghesi, and M. Passoni. "Ion acceleration by superintense laser-plasma interaction". In: *Reviews of Modern Physics* 85.2 (2013), p. 751.

[82] Y. B. ZelDovich and Y. P. Raizer. *Physics of shock waves and high-temperature hydrodynamic phenomena*. Courier Corporation, 2012.

[83] L. Gao, P. Nilson, I. Igumenshchev, M. Haines, D. Froula, R Betti, and D. Meyerhofer. "Precision mapping of laser-driven magnetic fields and their evolution in high-energy-density plasmas". In: *Physical review letters* 114.21 (2015), p. 215003.

[84] L Willingale, P. Nilson, M. Kaluza, A. Dangor, R. Evans, P Fernandes, M. Haines, C Kamperidis, R. Kingham, and C. Ridgers. "Proton deflectometry of a magnetic reconnection geometry". In: *Physics of Plasmas* 17.4 (2010), p. 043104.

[85] H. G. Rinderknecht, H.-S. Park, J. Ross, P. Amendt, D. Higginson, S. Wilks, D Haberberger, J Katz, D. Froula, and N. Hoffman. "Highly Resolved Measurements of a Developing Strong Collisional Plasma Shock". In: *Physical Review Letters* 120.9 (2018), p. 095001.

[86] C. Walsh, J. Chittenden, K McGlinchey, N. Niasse, and B. Appelbe. "Self-generated magnetic fields in the stagnation phase of indirect-drive implosions on the National Ignition Facility". In: *Physical Review Letters* 118.15 (2017), p. 155001.

[87] P. Chang, G Fiksel, M Hohenberger, J. Knauer, R Betti, F. Marshall, D. Meyerhofer, F. Séguin, and R. Petrasso. "Fusion yield enhancement in magnetized laser-driven implosions". In: *Physical Review Letters* 107.3 (2011), p. 035006.

[88] S. A. Slutz and R. A. Vesey. "High-gain magnetized inertial fusion". In: *Physical Review Letters* 108.2 (2012), p. 025003.

[89] P. Schmit, P. Knapp, S. Hansen, M. Gomez, K. Hahn, D. Sinars, K. Peterson, S. Slutz, A. Sefkow, and T. Awe. "Understanding fuel magnetization and mix using secondary nuclear reactions in magneto-inertial fusion". In: *Physical Review Letters* 113.15 (2014), p. 155004.

[90] A. Dubey, K. Antypas, M. K. Ganapathy, L. B. Reid, K. Riley, D. Sheeler, A. Siegel, and K. Weide. "Extensible component-based architecture for FLASH, a massively parallel, multiphysics simulation code". In: *Parallel Computing* 35.10-11 (2009), pp. 512–522.

[91] C. K. Birdsall and A. B. Langdon. *Plasma physics via computer simulation*. CRC press, 2004.

[92] D. R. Welch, D. Rose, B. Oliver, and R. Clark. "Simulation techniques for heavy ion fusion chamber transport". In: *Nuclear Instruments and Methods in Physics Research Section A: Accelerators, Spectrometers, Detectors and Associated Equipment* 464.1-3 (2001), pp. 134–139.

[93] D. Tidman. "Structure of a shock wave in fully ionized hydrogen". In: *Physical Review* 111.6 (1958), p. 1439.

[94] K. Abe and G. Sakaguchi. "Linear and nonlinear evolution of double-humped ion distributions in strong unmagnetized shock structures". In: *The Physics of fluids* 28.12 (1985), pp. 3581–3589.

[95] H. G. Rinderknecht, H.-S. Park, J. Ross, P. Amendt, S. Wilks, J Katz, N. Hoffman, G Kagan, E. Vold, and B. Keenan. "Measurements of ion velocity separation and ionization in multi-species plasma shocks". In: *Physics of Plasmas* 25.5 (2018), p. 056312.

[96] L. Spitzer Jr and R. Härm. "Transport phenomena in a completely ionized gas". In: *Physical Review* 89.5 (1953), p. 977.

[97] F Vidal, J. Matte, M Casanova, and O Larroche. "Modeling and effects of nonlocal electron heat flow in planar shock waves". In: *Physics of Plasmas* 2.5 (1995), pp. 1412–1420.

[98] R. A. Fonseca, L. O. Silva, F. S. Tsung, V. K. Decyk, W. Lu, C. Ren, W. B. Mori, S Deng, S Lee, and T Katsouleas. "OSIRIS: A three-dimensional, fully relativistic

particle in cell code for modeling plasma based accelerators". In: *International Conference on Computational Science*. Springer. 2002, pp. 342–351.

[99] F Pérez, L Gremillet, A Decoster, M Drouin, and E Lefebvre. "Improved modeling of relativistic collisions and collisional ionization in particle-in-cell codes". In: *Physics of Plasmas* 19.8 (2012), p. 083104.